Astronomy Reports, Vol. 49, No. 4, 2005, pp. 259–268. Translated from Astronomicheskiĭ Zhurnal, Vol. 82, No. 4, 2005, pp. 291–301.

Absorption in the H(93–95)α and H(78–79)α Recombination Lines in the HII Region of the Quasar 3C 345

L. I. Matveyenko[1], D. A. Graham[2], and J. A. Zensus[2]

[1]*Space Research Institute, Russian Academy of Sciences, Profsoyuznaya ul. 84/32, Moscow, 117997 Russia*

[2]*Max Planck Institut für Radioastronomie, Auf dem Hügel 69, D-53121 Bonn, Germany*

Received April 27, 2004; in final form, September 20, 2004

Abstract—Absorption of the synchrotron emission of the quasar 3C 345 in the continuum and H(93–95)α and H(78–79)α radio recombination lines is studied. The upper limit for absorption in the H(93–95)α lines is $T_{\rm al}/T_{\rm ac} < 0.7\%$; absorption in the H(78–79)α lines with antenna temperature $T_{\rm al} = 25$ mK, linewidth $\Delta f = 5.3 \pm 0.08$ MHz, and $T_{\rm al}/T_{\rm ac} \geq 0.3\%$ has been detected. A correction to the redshift $\Delta z = 0.00135 \pm 0.00008$ ($z = 0.59365$) has been determined. © *2005 Pleiades Publishing, Inc.*

1. INTRODUCTION

Active galactic nuclei (AGN) are galaxies with enhanced nuclear activity. They can be either galaxies of various types or galaxies at different stages of the formation of their nuclei, at different stages of their activity. Radio observations with high angular resolution indicate that the activity of the nuclei is manifest in the ejection of a relativistic jet of plasma with a speed near the speed of light. Dense clouds of relativistic particles that produce flares of synchrotron radio emission are ejected episodically. The radio emission of these flares is delayed and decreases in amplitude with increasing wavelength. The brightness temperatures of the dense clouds reach the Compton limit, $T_{\rm b} = 10^{12}$ K [1]. However, variability reappears at low frequencies, connected with the effect of the interstellar medium on the propagation of the radiation and the changing opacity of the circumnuclear ionized gas that gives rise to the optical emission lines. The effect of this material on the synchrotron radio emission can also appear as absorption in radio recombination lines. Below, we report the results of our study of the quasar 3C 345.

2. THE STRUCTURE OF 3C 345

The quasar 3C 345 is a typical AGN, with a redshift $z = 0.595$. For the Hubble constant $H_0 = 100$ km/s/Mpc and an acceleration parameter of $q_0 = 0.05$, an angular scale of 1 mas corresponds to 3.76 pc. The quasar center has an active "core," which ejects a stream of relativistic plasma and occasional compact clumps with speeds near the speed of light. The core is surrounded by an ionized medium—an HII region. The flow forces its way through this material and is wrapped up in it like a cocoon. As a result, the synchrotron emission of the relativistic plasma is observed through this compressed layer of ionized gas.

The structure of the quasar has been studied over a broad spectrum in the radio, from millimeter to meter wavelengths. Figure 1 shows the fine structure of the quasar 3C 345 at 1.35, 3.6, 6.0, 18, and 49 cm. The brightness temperatures are determined by synchrotron emission. The temperatures of the compact components reach the Compton limit, $T_{\rm b} \approx 10^{12}$ K. The transparency of the cocoon wall grows with frequency and distance from the ejector. Accordingly, the optical depth of the relativistic plasma flow itself decreases with increasing frequency and distance from the ejector. Therefore, at high radio frequencies, only the core–ejector and dense compact clouds (Fig. 1a, $\lambda = 1.35$ cm) are visible. With increasing wavelength, the distant parts of the jet lying outside the dense part of the cocoon wall become visible. The flow has a helical structure produced by the precession of the rotational axis of the ejector.

At 6 cm, the brightness temperature of the ejector region $T_{\rm ej}$ does not exceed $\approx 0.2 T_{\rm peak}$ (epoch 1992.5), i.e., it is lower than the temperature of the nearest jet components, whose temperature is $T_{\rm peak} \approx 10^{12}$ K (Fig. 1c) [2]. Studies of the quasar at 6 cm in 1998.22–1999.69 with an angular resolution of $\sim$0.35 mas revealed fine structure of the core region and separated the ejector from neighboring compact components (Fig. 2, left-side lower map) [3]. During this interval, the flux density increased from 0.8 Jy (1998.57) to 1.8 Jy (1999.50). The core region had an elongated shape oriented in the direction $X \approx -100°$ (Fig. 2, right-hand maps).

1063-7729/05/4904-0259$26.00

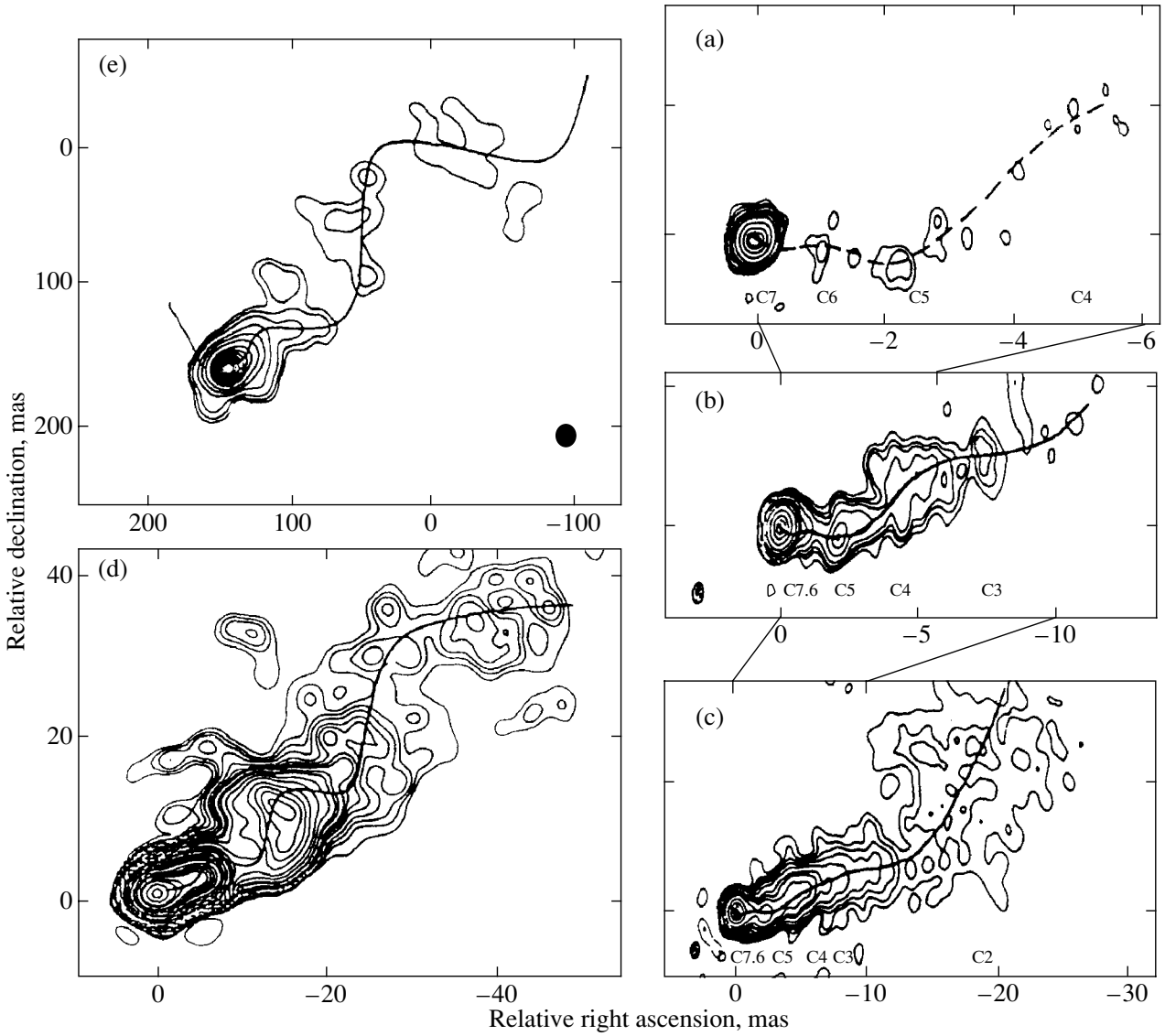

Fig. 1. Maps of the quasar 3C 345 at (a) 22 GHz (epoch 1992.53), (b) 8.4 GHz (1992.79), (c) 5.0 GHz (1992.5) [2], (d) 1.6 GHz (1985.35) [8], (e) 0.6 GHz (1986.8) [11].

Higher-frequency observations suggest orientation for the ejector axis of $-135°$ [4]. At 6 cm, the orientation of the bright component ("core") corresponds to a distance of $\sim$0.5 mas from the ejector. The brightness of the ejector region is about a factor of five and a factor of three lower than the brightness of the neighboring component at the first and second epoch, respectively. The brightness temperatures of these structures are close to the Compton limit: $T_b \approx 2 \times 10^{12}$ K [3, 5]. The observed increase of the brightness temperature with distance from the ejector is due to the increasing transparency of the screen wall. This is also testified to by the steep low-frequency cutoffs in the spectra of flares and of the core, which has a spectral index $\alpha \approx 3$ [6] (Fig. 3, curves *a* and *c*). A cutoff at centimeter wavelengths is observed in the spectrum of the central region [7].

At decimeter wavelengths, the main emission of 3C 345 is radiated by a bright region that is shifted from the ejector by $\sim$2 mas ($\lambda = 18$ cm) [4, 8]. Its effective brightness temperature is higher than the core temperature and essentially does not vary with time, $T_{peak} \approx 0.2 \times 10^{12}$ K. At $\lambda = 49$ cm, the bright compact region has an effective size of 5×4 mas, and is located at a projected distance of $\sim$16 mas from the ejector. Figure 4 shows the core region and its strip distribution of its brightness along the jet axis. The peak brightness temperature is $T_b \approx 0.5 \times 10^{12}$ K, and corresponds to the above component. The brightness temperature of the core region is $\sim$25 dB lower

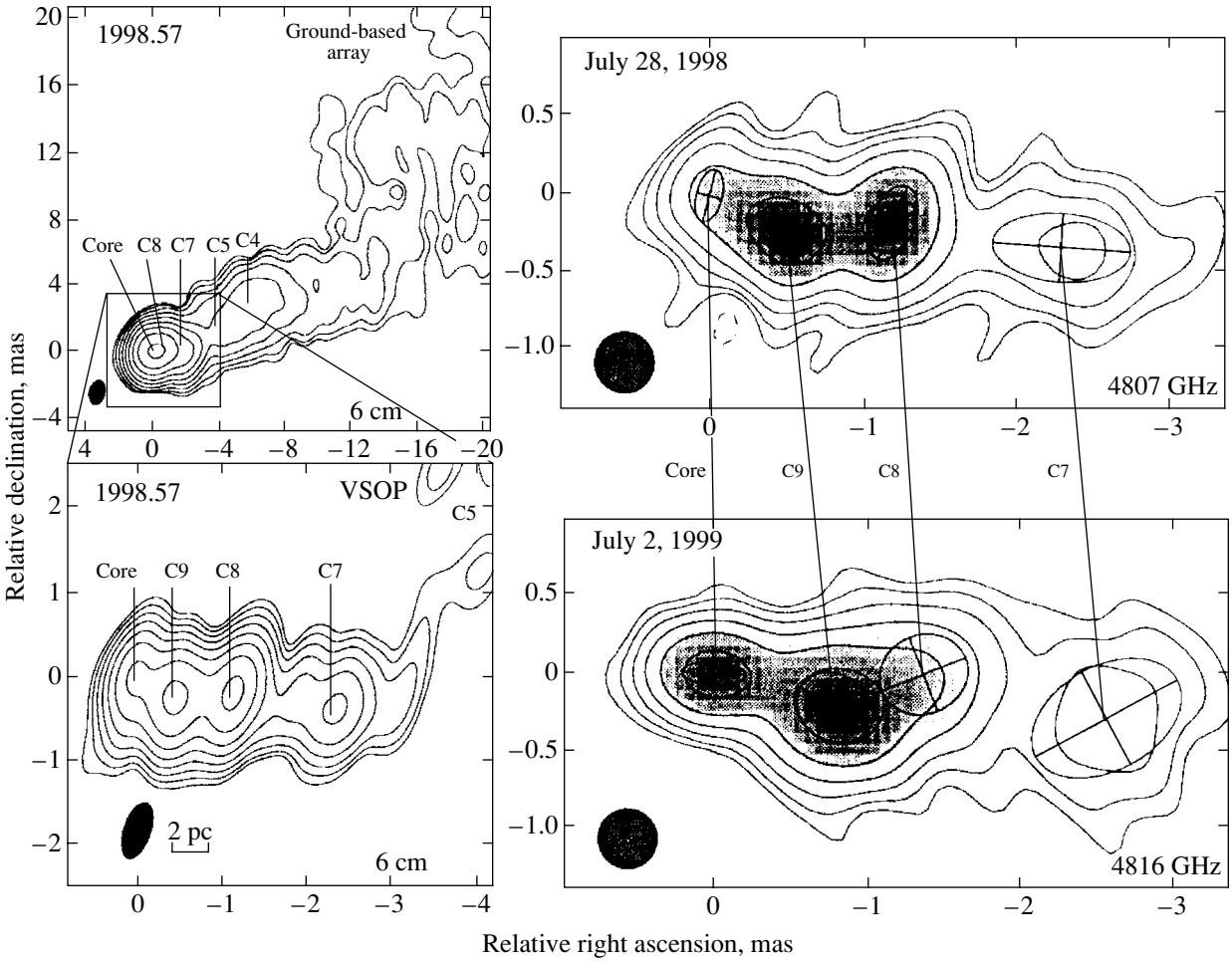

Fig. 2. Maps of the quasar 3C 345 at 6 cm [3].

[6]. At $\lambda = 92$ cm, the bright region is ~30 mas from the ejector, its effective size reaches 22.6×9.4 mas, and its brightness temperature is $T_b \approx 10^{11}$ K [9].

Figure 5 shows the brightness distributions along the jet axis at centimeter and decimeter wavelengths on a logarithmic scale. The distributions have been reduced to a 1-mas antenna beam. At millimeter and shorter centimeter wavelengths, the emission of the ejector region and of the compact components dominates. With increasing wavelength, the apparent brightness of the ejector region decreases considerably, and the region of maximum brightness recedes from it. This is due to the growing transparency of the screen with increasing distance and optical depth of the jet. At $\lambda = 49$ cm, the absorption in the core region reaches 25 dB; recalculated to $\lambda = 6$ cm, this corresponds to 6 dB, which is consistent with the above data. At $\lambda = 3.6$ cm, the absorption does not exceed a factor of 1.3.

3. RADIO FLARES

Synchrotron-emission flares in AGN are produced by dense compact clumps of relativistic plasma moving at speeds near the speed of light. The flare durations do not exceed several months. The flare emission is observed immediately upon its escape from the ejector at high frequencies. With growing distance from the ejector, the clump's optical depth decreases, its emission fades, and its maximum drifts toward lower frequencies. Though the screen's transparency is increasing, the intensity of the flare emission nevertheless decreases with time.

The enhanced activity of 3C 345 in 1981.5–1982.5 was accompanied by powerful radio flares at 8–89.6 GHz [10]. The spectrum of one of the most intense flares (epoch 1981.6) had a turnover at $f \approx 7$ GHz ($f \approx 11$ GHz in the quasar frame; Fig. 3, curve *a*) [11]. The spectral index of the low-frequency part is $\alpha \approx 3$, i.e., it is higher than the limiting theoretical value corresponding to synchrotron self-absorption, $\alpha = 2.5$. The spectral indices of optically thick sources of synchrotron emission are

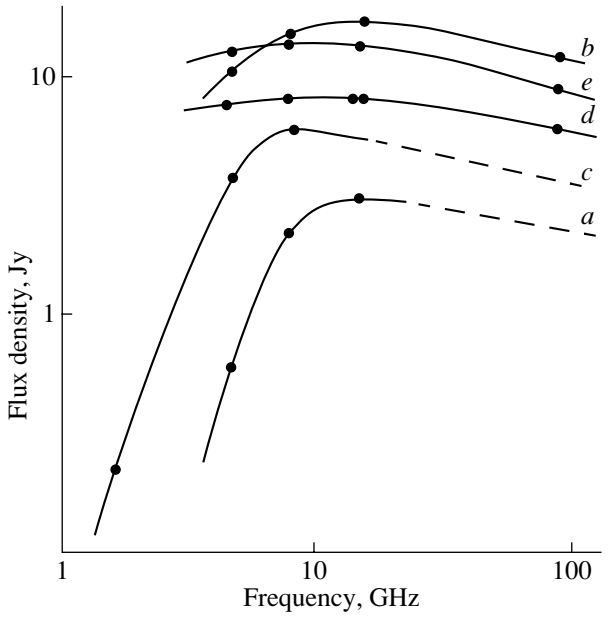

Fig. 3. Spectra of 3C 345 at various epochs: a flare at epoch 1981.6 (*a*); the total emission at epoch 1981.6 (*b*); the core at epoch 1981.6 (*c*); the total emission at epoch 1979.4 (*d*); and the total emission at epoch 1984.5 (*e*).

smaller than this limit. The observed steep low-frequency cutoff is due to the absorption of synchrotron emission in the screen—the surrounding ionized medium [11]. In a number of quasars, increases in the absorption result in "negative" flares, observed at decimeter wavelengths.

4. POLARIZATION OF THE RADIO EMISSION

The emission of 3C 345 is linearly polarized. The intensity and polarization of the radio emission of the jet and of individual components at $\lambda = 6$ cm vary depending on the relative position with respect to the core. The degree of polarization of the core and of nearby components (epoch 1985.12) does not exceed 2%; it increases to 18% at a distance of $R \approx 3$ mas (component C3) and to 20% at $R = 8$ mas (component C2) [12]. This is determined by a decrease in the optical depth of the radiating regions. The components initially have large optical depths. In this case, the limiting degree of polarization does not exceed 10%, and the polarization plane is aligned with the magnetic field. For an optically thin source, the level of polarization can reach 70%, and the polarization plane is perpendicular to the magnetic field (see, e.g., [13]).

The enhanced activity in 1981–1986 was accompanied by an increase in the intensity. At that time, the polarization and degree of polarization varied in antiphase with the intensity variations. This anticorrelation can be explained by an increase of the rotation measure (RM) of the cocoon wall.

The Faraday rotation of the polarization plane is $\psi = 18 \times 10^4 \mathrm{RM} f^{-2} \Delta f/f$ rad, where f is in MHz. The degree of polarization P depends on the rotation measure and the relative bandwidth of the received signal $\Delta f/f$. In the case of a rectangular frequency-response curve, the degree of polarization decreases:

$$P/P_0 = \sin\psi/\psi.$$

In practice, the frequency-response curve is not perfectly rectangular, and P/P_0 decreases monotonically.

The rotation measure of the quasar measured at 18–21 cm is $\mathrm{RM} \approx 29 \pm 8$ rad m^{-2}, and the degree of polarization is ~4% [14]. These data correspond to the region of maximum brightness. The region has a size of ~15 mas and is located at $R \approx 8$ mas from the core (Fig. 1). The rotation measure RM varies in proportion to R^{-3}, and is $\sim 10^4$ rad m^{-2} at $R \sim 1$ mas. The polarization measurements of 3C 345 at $f = 5$ GHz were carried out in a band with width $\Delta f = 28$ MHz. The increase in the total emission at 6 cm in 1984–1986 was accompanied by a decrease in the polarization from 3–4% to 1%, i.e., by about a factor of three. This corresponds to a change in the RM of the central region from $\sim 10^4$ to $\sim 10^5$ rad/m^2. In this region, the electron density in the screen wall is $N_\mathrm{e} = 10^5$–10^6 cm^{-3}, the wall thickness is ~0.1 pc, and the magnetic field is $B_{||} \approx (0.1$–$1)$ G.

5. THE HII REGION

The active regions of AGNs are surrounded by an ionized medium whose emission is observed in the optical in the form of narrow and broad Hα emission lines. The electron temperature of the HII region is $T_\mathrm{e} \approx 2 \times 10^4$ K [15]. The electron density in the narrow-line region reaches $N_\mathrm{e} \approx (10^5$–$10^6)$ cm^{-3}. The effective size of the region is $\sim 10^{21} L_{46}$ cm, where L_{46} is the UV luminosity of the quasar in units of 10^{46} erg/s. In the case of 3C 345, the effective size of the region is $\sim 10^{20}$ cm (~30 pc) or ~10 mas. The integrated electron density in the broad-line region is $N_\mathrm{e} \approx 10^8$ cm^{-3}; the effective size of this region does not exceed $\sim 10^{18.5} L_{46}$ and comprises a few percent of the size of the narrow-line region.

The surrounding medium is accreting onto the disk–black hole system and is basically concentrated in the azimuthal plane. A collimated flow of relativistic plasma is ejected along the disk rotation axis. It forces its way through the surrounding ionized medium and is wrapped up in it like a cocoon. The thickness of the

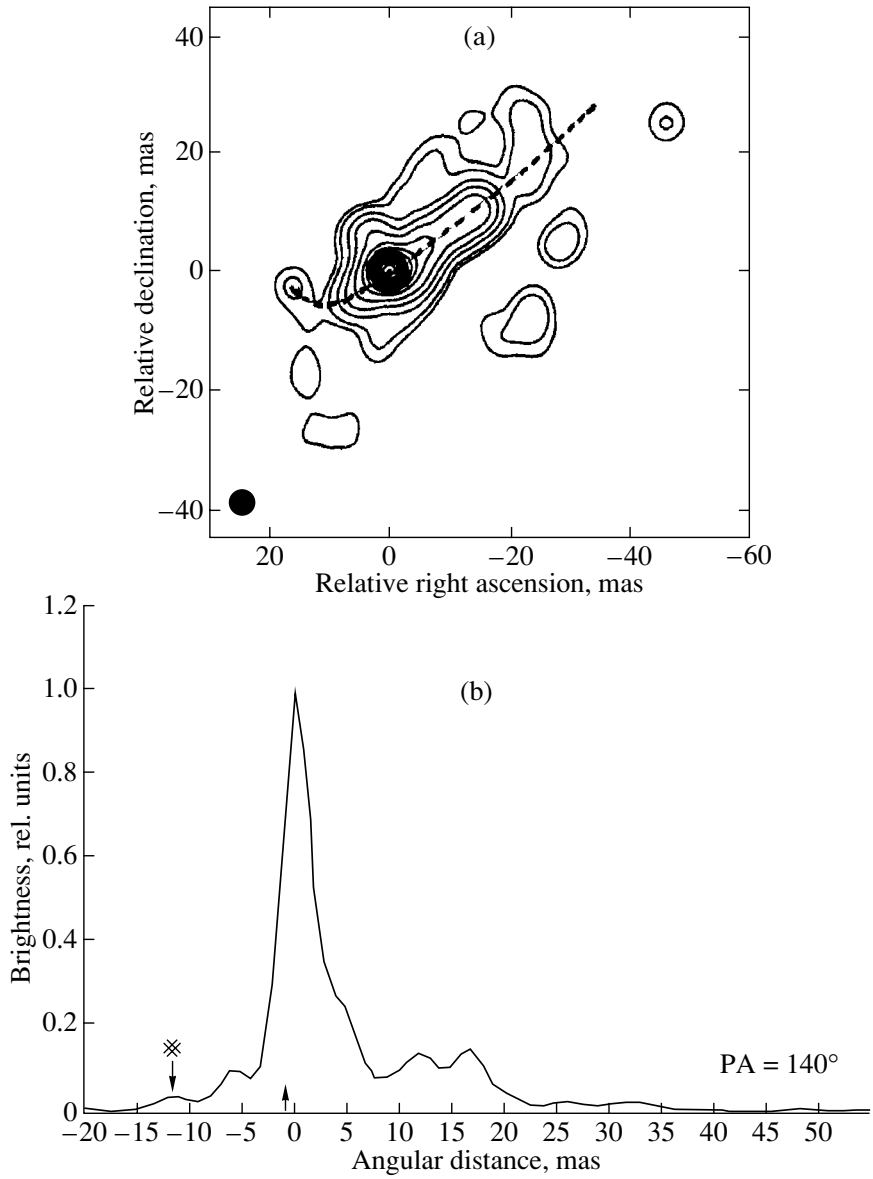

Fig. 4. (a) Core region of 3C 345 at 49 cm and (b) strip brightness distribution along the axis of the quasar jet at the same wavelength.

cocoon wall is determined by the condition of equilibrium between the pressure of the thermal and relativistic plasma. The pressure in the jet is proportional to the square of the density of the medium ($P_{\rm jet} \sim \rho^2$), and decreases with distance from the injector as R^{-2}. Accordingly, the electron density decreases as $N_{\rm e} \sim R^{-2}$, and the wall thickness increases as $l \sim R$ [16]; thus, the emission measure EM $\sim N_{\rm e}^2 l$ will decrease with distance as R^{-3}. Similarly, the rotation measure RM $\sim N_{\rm e} B_{||} l$, where $B_{||} \sim R^{-2}$ is the axial component of the magnetic field, varies as R^{-3}.

The absorption in the cocoon wall e^{τ} is determined by its optical depth

$$\tau = 0.08 T_{\rm e}^{-1.35} [(1+z)f]^{-2.1} \int N_{\rm e}^2(l) dl,$$

where f is the frequency of the received emission in MHz, $T_{\rm e} = 2 \times 10^4$ K is the electron temperature of the ionized gas, l is the screen thickness in parsecs, and $N_{\rm e}(l)$ is the line-of-sight distribution of the electron density in cm^{-3}.

The optical depth varies with the distance as $\tau \sim R^{-3}$. Thus, the synchrotron emission of the flow of relativistic plasma is observed through the cocoon wall, whose transparency increases with distance from the ejector. The electron density in the ejector

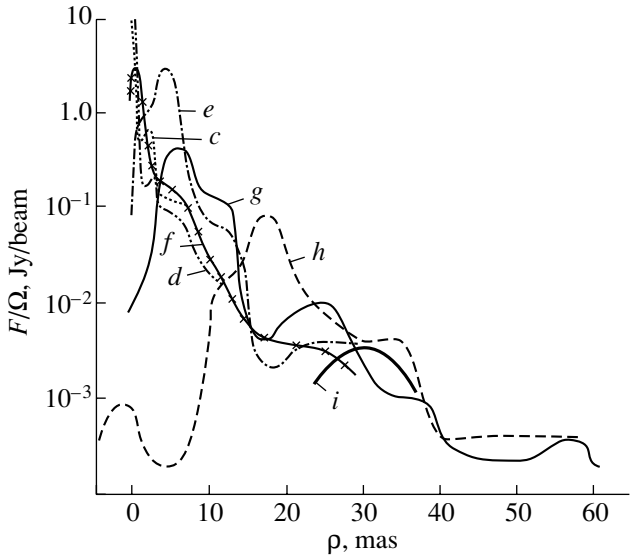

Fig. 5. Brightness distributions along the jet axis of the quasar 3C 345, reduced to a 1-mas beam for: $\lambda = 1.35$ cm (curve *c*), $\lambda = 3.6$ cm (curve *d*), $\lambda = 6$ cm (1990, curve *e*), $\lambda = 6$ cm (1992, curve *f*), $\lambda = 18$ cm (curve *g*), $\lambda = 49$ cm (curve *h*), $\lambda = 92$ cm (curve *i*).

region probably reaches $N_e \approx 10^8$ cm^{-3} and drops to $N_e \approx 10^5$ cm^{-3} at a distance of $\sim$10 mas. Thus, absorption limits the possibility of observing the core region even at the shortest radio wavelengths.

The core activity is accompanied by an increase in the UV radiation, which results in an increase in the emission measure EM. Accordingly, the screen transparency changes, resulting in variability and, in some cases, "negative" radio flares at decimeter wavelengths. The timescale t for the low-frequency variability is $\approx$1 year. The recombination timescale t_r in the ionized medium is $N_e/10^5$ years. It follows that the electron density in the region of the low-frequency emission is $N_e \approx 10^5$ cm^{-3}, and the screen wall thickness l for an optical depth $\tau \approx 1$ will be $\approx 10^{-3}$ pc. A change of the emission measure inevitably results in a change of the rotation measure RM.

6. ABSORPTION IN RADIO RECOMBINATION LINES

The synchrotron radio emission of active regions in AGN is observed through an ionized absorbing medium. In this case, the increment of the antenna temperature is

$$T_a(f) \approx T_0 e^{-\tau(f)} + T_e\{1 - e^{-\tau(f)}\},$$

where $T_0 \leq 10^{12}$ K is the brightness temperature of the region of synchrotron emission, $T_e \approx 2 \times 10^4$ K is the electron temperature of the absorbing medium (screen), and $\tau(f)$ is its optical depth.

The background brightness temperature considerably exceeds the electron temperature of the screen ($T_0 \gg T_e$), and the recombination line will be observed in absorption, determined by the optical depth of the screen $\tau(f)$. The transparency of the screen (cocoon wall) grows with distance from the ejector and with the signal frequency. At high frequencies, the optical depth of the screen is small ($\tau < 1$), and the increment of the antenna temperature is

$$T_a(f) \approx T_0 + T_e\tau(f) \approx T_0.$$

At low frequencies, when $\tau \geq 1$, the increment of the antenna temperature is

$$T_a(f) \approx T_0 e^{-\tau(f)}.$$

The absorption coefficient in the continuum for free–free transitions at radio wavelengths is [17]

$$K_c \approx 0.08235 N_e N_i f^{-2.1} T_e^{-1.35} \text{ pc}^{-1},$$

where N_e and N_i are, respectively, the electron and ion densities in cm^{-3} and f is the frequency in GHz.

The absorption coefficient in a line at local thermodynamic equilibrium for $h\nu \ll kT_e$ is

$$K_l = 1.07 \times 10^7 \Delta n (f_{nn'}/n) N_e N_i T_e^{-2.5} \times \exp\{E/kT_e\} f(\nu)$$

for two energy levels with principal quantum numbers n and n', where n is the lower value of the principal quantum number, Δn is the change of n, and E is the energy of the upper quantum level. For hydrogen, $E/kT_e \approx 1.579 \times 10^5/n^2 T_e$.

The ratio of the emission coefficients in the line and continuum is determined by the ratio of their optical depths, or absorption coefficients, and is

$$\int (I_l/I_c) d\nu = 1.299 \times 10^5 \Delta n (f_{nn'}/n) \nu^{2.1} T_e^{-1.15} \times F \exp\{1.579 \times 10^5 n^{-2}/T_e\},$$

where F is a factor describing the interaction of helium ions and electrons and ν is in kHz.

The ratio I_l/I_c grows with frequency, or decreasing principal quantum number. The population of the energy levels of the hydrogen atom is described by the Boltzmann distribution with the electron temperature. In the case of a small optical depth in the line ($\tau_l \ll 1$) and continuum ($\tau_c \ll 1$), the ratio T_l/T_c is

$$(T_{l+c} - T_c)/T_c = T_l/T_c.$$

At the same time, for $\tau_c \geq 1$, this ratio is reduced by a factor of $\tau_c/(e^{\tau_c} - 1)$. In the Orion Nebula, in the Hα line for the principle quantum number $n = 109$ ($f_0 = 5008.93$ MHz), the ratio $T_l/T_c = 5.2\%$ [18].

In this case, the linewidth is $\Delta f \approx 485$ kHz, which corresponds to a temperature of $T \approx 6000$ K. This relationship should also hold in the case of absorption. However, in the HII regions of AGN, deviations from thermodynamic equilibrium are possible, which will lower this ratio.

In AGN, the optical depths of the screen and jet decrease with distance from the ejector. The maximum effect is expected in regions where the screen is fairly transparent ($\tau_c < 1$) and the jet has a fairly high brightness temperature. When $\tau_c \approx 1$, the ratio T_l/T_c will be a factor of 0.6 lower than in the optically thin case. A single-dish radio telescope would observe the ratio T_l/T_c averaged over the source. The region of synchrotron emission in AGN extends far beyond the HII region; in turn, this will lower the ratio T_l/T_c. Therefore, it is expedient to observe at high frequencies, where the emission of the extended part of the jet is low and the screen transparency is fairly high. Spectral measurements of the structure of the quasar with high angular resolution, including observations at different frequencies, will allow us to obtain the distribution of absorption in the object and determine its correlation with the object's structure [19].

7. OBSERVATIONS OF THE QUASAR 3C 345

The choice of frequency band is determined by the expected ratio T_l/T_c and the sensitivity of the radio telescope. Special attention should be paid to spurious effects caused by standing waves in the antenna. The maximum sensitivity of large instruments is at centimeter wavelengths. One of the most sensitive instruments is the 100-m radio telescope of the Max-Planck-Institut für Radioastronomie in Effelsberg. The 6-cm waveband corresponds in the quasar 3C 345 ($z = 0.595$) to frequencies of $f = 8$–9 GHz; there are lines with principal quantum numbers $n = 93$–95. Near 3 cm, there are lines with $n = 78$–79. The table lists the frequencies of Hα radio recombination lines in MHz with different principal quantum numbers n for the quasar 3C 345.

Observations of a number of AGN were carried out on May 21–22 and June 10–11, 2001 on the 100-m radio telescope in Effelsberg in left- and right-circular polarizations on and off source. To improve the sensitivity and reduce spurious effects, we observed three neighboring lines with different principal quantum numbers at 6 cm. To eliminate spurious effects due to standing waves, the feed with the receiver was displaced along the electric axis by $\pm\lambda/8$ relative to the calculated position. This changed the phase of the standing waves by 180°. At the same time, the level of the received signal remained virtually unchanged. The amplitude and velocity (frequency)

Frequencies of the recombination lines

H$n\alpha$	f_l, MHz	f_{obs}, MHz ($z = 0.595$)
78	13595.51	8523.83
79	13088.87	8206.19
91	8584.84	
92	8309.40	
93	8045.62	5044.27
94	7792.88	4885.82
95	7550.63	4733.94
108	5148.71	
109	5008.93	
110	4874.17	

were calibrated using observations of the H(108–110)α emission lines of the gas–dust complex W3.

Observations of the calibration source W3. As a result of the 6-cm observations, we obtained the total spectrum of three lines of the source W3 in left- and right-circular polarizations for principal quantum numbers $n = 108$–110 (Fig. 6a). Since the emission in the lines was fairly strong, we made no observations with the feed shifted by $\pm\lambda/8$. The bandwidth for the analysis is 40 MHz, with 512 individual channels separated by 78.1 kHz, or $\Delta v = 4.68$ km/s. A small ripple in the data is due to standing waves. The amplitude of the standing waves does not exceed 0.2 K, and the period of the standing wave is 5.1 MHz, which corresponds to a distance between the feed and secondary mirror of 19.7 m. The averaged H(108–110)α recombination line is prominent in the spectrum. Its average antenna temperature is T_{al} is 1.23 K. The continuum temperature is $T_{ac} = 29.95$ K, and the ratio $T_{al}/T_{ac} = 4.1\%$. The linewidth at a level of 3-dB is $\Delta f = 5.5 \pm 0.2$ channels, or $\Delta f = 430 \pm 16$ kHz. The line center is at channel 265.2 ± 0.5. The velocity of the observed line (source) is $V_{LSR} = -42.3$ km/s, i.e., shifted toward higher frequencies by 9.0 channels. The zero velocity is at channel 256.2. In addition to the hydrogen recombination line, lines of helium He109α and carbon C109α (channel 270) are also visible in the profile, as well as the H137β hydrogen line (channel 210).

Observations of 3C 345 at 6 cm. The observations of the AGN were performed using a similar technique. In AGN, the ionized medium is observed against the bright background of the source of synchrotron radio emission. The brightness temperature

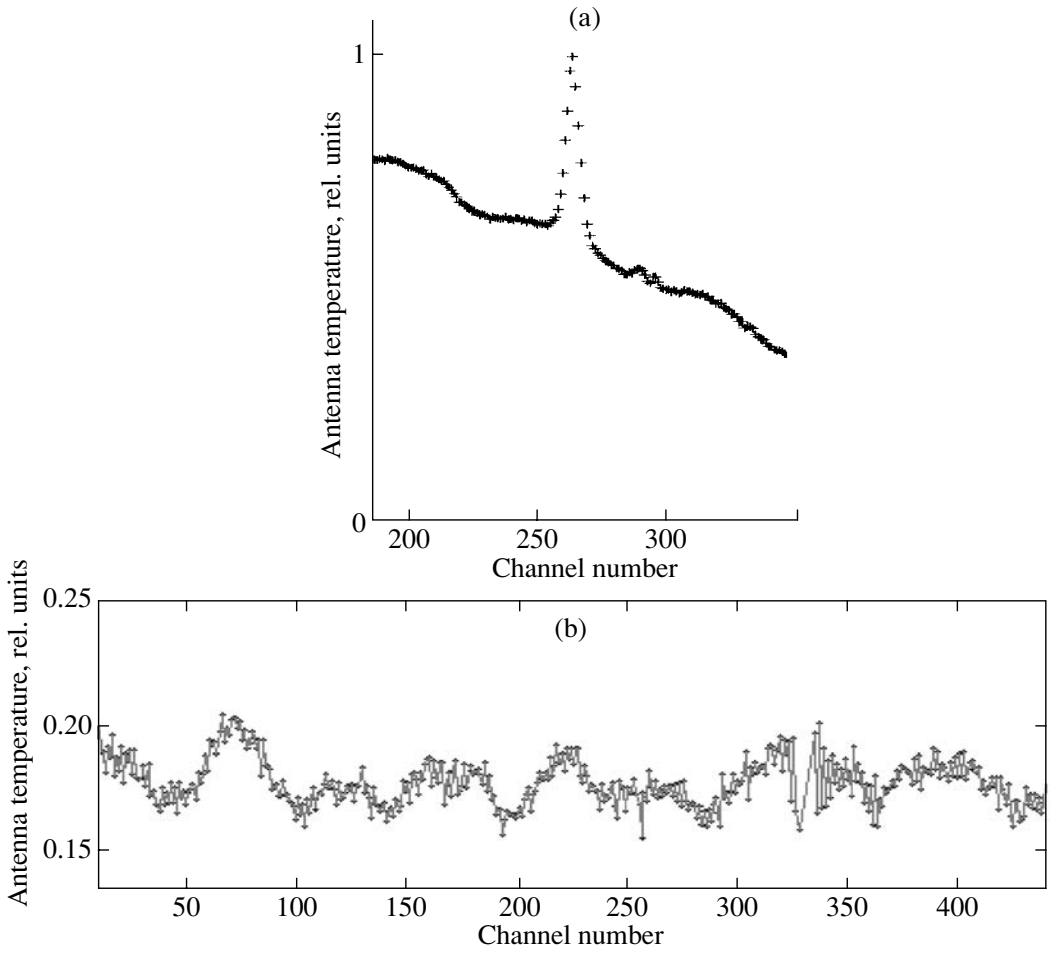

Fig. 6. (a) Line profile in the spectrum of the calibration source W3 with principal quantum numbers $n = 108$–110 and (b) an averaged recording of the emission of 3C 345 in the lines with principal quantum numbers $n = 93$, 94; wavelength $\lambda = 6$ cm.

T_0 of the emission of the relativistic plasma reaches $\approx 10^{12}$ K, far greater than the electron temperature T_e of the screen ($T_e \ll T_0$). In this case, the on-source antenna temperature is $T_a(f) \approx T_0 e^{-\tau(f)}$, and the absorption recombination line is observed against the bright background of the synchrotron emission region. The results for 3C 345 are presented below. The frequencies of recombination lines of the ionized region visible at frequencies of about 5 GHz for $z = 0.595$ correspond to principal quantum numbers $n = 91$–94 (table).

The observations were carried out in three lines with different principal quantum numbers in both circular polarizations, with the feed shifted by $\pm\lambda/8$, with the antenna pointing on and off source. The frequency resolution Δf is 78.1 kHz, or $\Delta v = 4.68$ km/s. The technical sensitivity was poorer than the calculated value due to instrumental effects having to do with the frequency conversion in the correlator. Figure 6b shows the averaged record. The integration time was ~40 min, and the on-source antenna noise temperature was $T_a \approx 10.5$ K. The peak-to-peak fluctuations reach 45 mK, which is twice the calculated value of $6\sigma = 20$ mK. The upper limit of the signal at a level of $T_a = 10\sigma$ is 75 mK, and the ratio $T_{al}/T_{ac} = 0.007$, or 0.7%. The antenna temperature T_{ac} is determined by the total emission of the studied object; the absorption in the lines is due only to the part where the screen optical depth is relatively small and the background brightness is significant. The main emission of 3C 345 at 6 cm is determined by its central region, where the screen optical depth $\tau \geq 1$ and the ratio T_{al}/T_{ac} should be lowered. In the equilibrium case, when $\tau \approx 1$, the ratio T_{al}/T_{ac} is reduced compared to the optically thin case by a factor of $\tau_c/(e^{\tau_c} - 1) = 0.6$. The main effect takes place at a distance of several mas from the ejector. The contribution of the emission of this region does not exceed 20–30% of the total flux of the radio

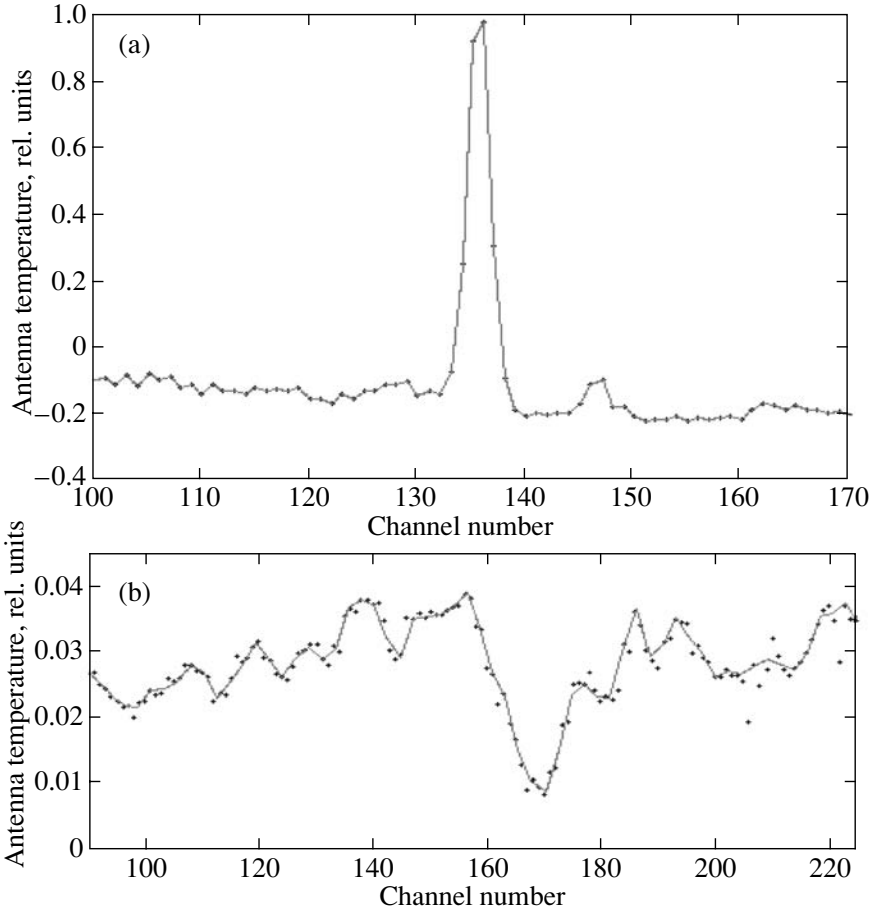

Fig. 7. (a) Average profile for the lines with principal quantum numbers $n = 91–92$ in the spectrum of the calibration source W3 and (b) average profile for the absorption lines with principal quantum numbers $n = 78–79$ in the spectrum of 3C 345; wavelength $\lambda = 3$ cm.

emission, and, accordingly, the upper limit of the ratio T_{al}/T_{ac} is $\geq 3.5\%$.

Observations of 3C 345 at 3 cm. Observations of the calibration source W3 were carried out on June 10–11, 2001, using a similar technique simultaneously in two lines, $n = 91–92$, in both circular polarizations with the feed shifted by $\pm\lambda/8$ and on–off antenna pointing. The line frequencies are listed in the table. During the observations, the observed frequency of the H91α line corresponded to $f = 8585.170$ MHz and, with regard to the source velocity ($v = -42.3$ km/s), to 8586.383 MHz. The bandwidth was 80 MHz with 256 individual channels, corresponding to a frequency resolution (channel spacing) of 312.5 kHz, or 11 km/s.

Figure 7a presents the total profile in the spectrum of W3. The line position is at channel 135.7 ± 1 ($v = -42.3$ km/s, $f = 8586.383$ MHz), at channel 122.2 if recalculated to the zero velocity ($f = 8585.170$ MHz, $\Delta f = 1.213$ MHz, which corresponds to 13.5 channels). The linewidth $\Delta f = 820$ kHz matches the expected value. The antenna temperature in the line T_{al} is 1.1 K; in the continuum $T_{ac} = 17.1$ K.

3C 345 was observed in the lines with principal quantum numbers $n = 78–79$. Figure 7b shows the total profile for the source spectrum. The frequency of the absorption line is at channel 168.6 ± 2, and is shifted from zero by 36.8 ± 2 channels, or 11.5 MHz. The zero position corresponds to the calculated frequency of the H78α line ($f = 8523.83$ MHz; see table). During the observations, the line frequency was $f = 8524.226$ MHz, and differed by $\Delta f = 0.396$ MHz, or 2.35 channels. Thus, the absorption line is shifted from the expected position ($z = 0.595$) by 34.4 ± 2 channels. This difference is $\Delta f = (10.75 \pm 0.60)$ MHz, which corresponds to $\Delta z = 0.00126 \pm 0.00007$, and, accordingly, $z = 0.59374 \pm 0.00007$.

The antenna temperature in the absorption line is $T_{al} = 25$ mK and in the continuum is $T_c = 8$ K. The mean ratio T_{al}/T_{ac} is 0.3%. The main emission of the quasar at 3 cm is determined by the core. The optical depth of the absorbing screen is insignificant. The

ratio T_{al}/T_{ac} can be partly underestimated, but not by more than several factor.

The linewidth Δf is 5.3 ± 0.3 MHz, and is determined by Doppler broadening—the kinetic temperature of the medium and its microturbulence. For a Maxwellian velocity distribution of the particles, the line profile is Gaussian, and the total linewidth at the half-maximum level is

$$\Delta f_D = (2f_{mn}/c)\sqrt{\ln 2(2kT_k/M + \langle V\rangle^2)},$$

where $\langle V\rangle$ is the probable turbulent velocity.

The obtained profile width of the absorption line $\Delta f = 5.3 \pm 0.3$ MHz considerably exceeds the Doppler value, ~820 kHz. This broadening is probably determined by microturbulence of the medium or by a velocity gradient within the absorption region. The corresponding effective velocity $\langle V\rangle$ is ≈100 km/s.

8. CONCLUSIONS

We have carried out spectral observations of the quasar 3C 345 at 5- and 8-GHz on the 100-m radio telescope in Effelsberg in left- and right-circular polarizations with two positions of the feed spaced by $\pm\lambda/8$.

We have studied the absorption of the synchrotron emission of the quasar in the surrounding HII region in the H(92–94)α and H(78–79)α radio recombination lines.

An upper limit for the ratio of the antenna temperatures in the H(92–94)α absorption lines and in the continuum is $T_{al}/T_{ac} < 0.7\%$.

We have detected absorption in the H(78–79)α lines; the ratio of the antenna temperatures is $T_{al}/T_{ac} = 0.3\%$, and the linewidth is $\Delta f = 5.3 \pm 0.08$ MHz.

The measured line frequency differs from the expected value by $\Delta f = 10.75 \pm 0.60$ MHz, which corresponds to $\Delta z = 0.00126 \pm 0.00007$ and $z = 0.59374 \pm 0.00007$.

ACKNOWLEDGMENTS

This work was supported by the Russian Foundation for Basic Research (project no. 02-02-1677) and the Program of the Presidium of the Russian Academy of Sciences "Nonstationary Phenomena in Astronomy." One of the authors (L.I.M.) thanks Max-Planck-Institut für Radioastronomie for assistance in this work and to R.D. Dagkesamanskiĭ for helpful comments.

REFERENCES

1. K. I. Kellermann and I. I. K. Pauliny-Toth, Astrophys. J. **155**, L71 (1969).
2. J. A. Zensus, *Extragalactic Radio Sources—From Beams to Jets*, Ed. by J. Roland, H. Sol, and G. Pelletier (Cambridge Univ. Press, Cambridge, 1993), p. 154.
3. J. Klare, J. A. Zensus, E. Ros, and A. P. Lobanov, in *Astrophysical Phenomena Revealed by Space VLBI*, Ed. by H. Hirabayashi, P. G. Edwards, and D. W. Murphy (ISAS, Tokyo, 2000), p. 21.
4. L. I. Matveenko, D. A. Graham, I. I. K. Pauliny-Toth, *et al.*, Pis'ma Astron. Zh. **18**, 931 (1992) [Sov. Astron. Lett. **18**, 379 (1992)].
5. E. Ros, J. A. Zensus, and A. P. Lobanov, Astron. Astrophys. **354**, 55 (2000).
6. L. I. Matveenko, D. A. Graham, I. I. K. Pauliny-Toth, *et al.*, Astron. Astrophys. **312**, 16 (1996).
7. A. P. Lobanov and J. A. Zensus, Astron. Lett. **22**, 16 (1996).
8. F. T. Rantakyro, L. B. Baath, I. I. K. Pauliny-Toth, *et al.*, Astron. Astrophys. **259**, 8 (1992).
9. Hong Xiao-yu, Wan Tong-shan, Shen Zhi-qiang, *et al.*, Chinese Astron. Astrophys. **19**, 60 (1995).
10. J. N. Bregman, A. E. Glassgold, P. J. Huggins, *et al.*, Astrophys. J. **301**, 708 (1986).
11. L. I. Matveenko, I. I. K. Pauliny-Toth, W. A. Sherwood, *et al.*, Pis'ma Astron. Zh. **12**, 156 (1986) [Sov. Astron. Lett. **12**, 63 (1986)].
12. L. F. Brown, D. H. Roberts, and J. F. C. Wardle, Astrophys. J. **437**, 108 (1994).
13. K. I. Kellermann, *Galactic and Extra-Galactic Radio Astronomy*, Ed. by G. L. Verschuur and K. I. Kellermann (Springer-Verlag, New York, 1976), p. 346.
14. L. Rudnick and T. W. Jones, Astron. J. **88**, 518 (1983).
15. H. Netzer, *Astrophysical Jets and Their Engines*, Ed. by W. Kundt (D. Reidel Publ. Comp., Dordrecht, 1987), p. 103.
16. M. C. Begelmann, R. D. Blanford, and M. J. Rees, Rev. Mod. Phys. **56**, 255 (1984).
17. M. A. Gordon, in *Galactic and Extra-Galactic Radio Astronomy*, Ed. by G. L. Verschuur and K. I. Kellermann (Springer-Verlag, New York, 1976), p. 110.
18. P. G. Mezger and A. P. Henderson, Astrophys. J. **147**, 471 (1967).
19. L. I. Matveenko, Pis'ma Astron. Zh. **27**, 807 (2001) [Astron. Lett. **27**, 686 (2001)].
20. E. Churchwell and C. M. Walmsley, Astron. Astrophys. **38**, 451 (1973).
21. L. I. Matveyenko, A. I. Witzel, and J. A. Zensus, *Proc. IAU Colloq. No. 182* (China, 2000).

Translated by G. Rudnitskii

Astronomy Reports, Vol. 49, No. 4, 2005, pp. 269–273. Translated from Astronomicheskiĭ Zhurnal, Vol. 82, No. 4, 2005, pp. 302–307.

The Generation of Low-Energy Cosmic Rays in Molecular Clouds

Yu. A. Shchekinov

Rostov State University, Rostov-on-Don, Russia;
Astronomisches Institut, Ruhr-Universität, Bochum, Germany

Received September 10, 2003; in final form, September 20, 2004

Abstract—Arguments are presented in support of the idea that the total energy losses of cosmic rays passing through molecular clouds can exceed the energy production due to the action of shocks in supernovae. Galactic cosmic rays interacting with the surface layers of molecular clouds can be efficiently reflected, so that they do not penetrate into the depths of the clouds. Low-energy cosmic rays ($E < 1$ GeV) that can produce the primary ionization of the molecular-cloud gas can be generated inside such clouds by numerous shocks arising due to supersonic turbulence. © *2005 Pleiades Publishing, Inc.*

1. INTRODUCTION

Gas-phase chemical reactions in molecular clouds are predominantly ion–molecular reactions, and are catalyzed by H^+, H_2^+, and H_3^+ ions, which are produced, in turn, by low-energy cosmic rays ($E \lesssim 1$ GeV; see the review [1]). The primary ionization rate by cosmic rays required to sustain the degrees of ionization and concentrations of these ions is estimated to be $\zeta \sim 10^{-17}$ s^{-1}. A similar value is obtained for the upper limit to the primary ionization rate derived from the abundances of HD in molecular clouds, $\zeta \lesssim 10^{-16}$–10^{-17} s^{-1} [2, 3]. It was first proposed in [4] that the degrees of ionization in the cores of molecular clouds might exceed the value corresponding to $\zeta \sim 10^{-17}$ s^{-1} by a factor of five, which would require that ζ be increased by a factor of 25. Based on the assumption that the predominant magnetic-field structure in molecular clouds is dipolar, it was shown in [5] that cosmic rays with energies $E > 1$ MeV/nucleon essentially freely penetrate into the cores, with ionization losses constituting about 10% of their energy (see also [6]). For this reason, the above estimates of the primary ionization rate are considered to be valid for the interstellar medium as well.

However, new data on the properties of molecular clouds and new theoretical analyses of their nature have recently cast doubts on the unconditionality of the conclusions of [5] and the general view that the primary ionization rates by cosmic rays in molecular clouds and in the ISM are in agreement. We present here arguments supporting the idea that cosmic rays with energies $E \lesssim 1$ GeV are not able to penetrate into the cores of molecular clouds, so that the presence of such particles there suggests that high-energy, nonrelativistic, nonthermal particles are generated within the molecular clouds themselves. This could occur, in particular, due to MHD shock waves arising from more rarefied gas during the formation of the molecular cloud.

Section 2 presents estimates of the total energy lost by Galactic cosmic rays in molecular clouds, and shows that these energy losses exceed the total power injected into cosmic rays by supernovae. Section 3 presents arguments based on the results of recent numerical modeling that suggest that the magnetic-field structure in a molecular cloud should differ from a simple dipolar field, and probably has a toroidal (helical) component in the plane perpendicular to the rotational axis of the cloud. In this case, most of the cosmic rays incident on the cloud should be reflected. Section 4 presents estimates of the efficiency of the acceleration of cosmic rays by MHD shock waves in molecular clouds. Finally, Section 5 summarizes our conclusions.

2. ENERGY LOSSES OF COSMIC RAYS IN MOLECULAR CLOUDS

It can easily be shown that the dominant contribution to the primary ionization rate by Galactic cosmic rays with an energy spectrum [7]

$$J(E) \simeq \frac{3 \times 10^4}{(800 + E)^{2.5}}\ (\mathrm{cm^2\ sr\ s\ MeV})^{-1} \quad (1)$$
$$(E < 10\ \mathrm{GeV})$$

is provided by cosmic rays with energies $E < 1$ GeV (the energy E in (1) is in MeV); the spectrum has a break at energies $E > 10$ GeV, where its slope becomes steeper. The fraction of the total energy $E = \gamma m_p c^2$ lost by a cosmic-ray particle (proton) as it passes through material with a hydrogen density

1063-7729/05/4904-0269$26.00

along the path N_L is determined to an order of magnitude as in [6]

$$\delta_E = \frac{4\pi e^4 \Lambda}{m_e c^2 m_p c^2} \frac{\gamma}{\gamma^2 - 1} N_L \simeq (0.5 - 1) \times 10^{-4} \frac{\gamma}{\gamma^2 - 1} N_{L,22}, \quad (2)$$

where $\Lambda = \ln[2m_e c^2 \beta^2 / I(1 - \beta^2)] - \beta^2 \simeq 5 - 12$ for energies from 1 MeV to 1 GeV, $N_{L,22} = 10^{-22} N_L$, $\beta = v/c$, and c is the speed of light. As it penetrates into a cloud, a high-energy particle undergoes numerous scatterings, so that the total path length traversed by the particle in the cloud is $L \sim 4cR^2/D$, where R is the radius of the cloud and D is the diffusion coefficient for cosmic rays in the cloud. The total density of particles along the trajectory is $N_L \sim 2NR/\lambda \gg N$ [6], where λ is the characteristic correlation scale for turbulence in the magnetic field, $\lambda \ll R$, and N is the surface density of the molecular cloud. Observed molecular clouds display a roughly constant (independent of radius) surface density of $N = 1.5 \times 10^{22}$ cm^{-2} (see the review [8]). Thus,

$$\delta_E \sim (1.5 - 3) \times 10^{-4} \frac{\gamma}{\lambda_R (\gamma^2 - 1)}, \quad (3)$$

$\lambda_R = \lambda/R$; for $E_k = 100$ MeV and $\lambda_R = 0.1$, we find $\delta_E \sim 0.01$.

The energy absorbed by all the molecular clouds in the Galaxy is

$$\dot{E}^{cr}_{MC} = S \int\limits_{100\,\mathrm{MeV}}^{\infty} \delta_E E J(E) dE \sim 5 S \lambda_R^{-1} \text{ erg/s}, \quad (4)$$

where S is the total surface area of the molecular clouds. Adopting for the entire Galaxy the molecular-cloud spectrum obtained in [9],

$$\frac{d\mathcal{N}}{dM} = A M^{-1.73}, \quad (5)$$

over the interval $M = [M_1 = 10^2, M_2 = 10^6] M_\odot$ with the normalization factor $A = 3.5 \times 10^7$, we can find the total surface area of clouds:

$$S = 4\pi \int\limits_{M_1}^{M_2} R^2 \frac{d\mathcal{N}}{dM} dM = 7 \times 10^{46} \sigma n^{-2/3}, \quad (6)$$

where $n \simeq 10^2$ cm^{-3} is the mean gas density in the clouds and $\sigma > 1$ is a factor taking into account the fact that the surface area of a cloud is greater than that of a sphere due to irregularities in the cloud boundary [10]. When computing the normalization coefficient A, we assumed that the mass spectrum of molecular clouds determined in [9] for the Perseus arm is valid for the Galaxy as a whole, with the mass of molecular gas in the Galaxy being $5 \times 10^9 M_\odot$. This yields $S \simeq 3 \times 10^{45} \sigma$ cm^2, and $\dot{E}^{cr}_{MC} \simeq 2 \times 10^{42} \sigma / \lambda_R$ erg/s for the energy losses of cosmic rays in clouds. The production of energy in Galactic cosmic rays in supernovae is $\dot{E}^{cr}_{SN} \sim 10^{42} \eta \nu_{1/30}$ erg/s, where $\eta < 1$ is the fraction of the supernova energy that goes into cosmic rays (for which modern estimates yield $\eta \sim 0.1$ [11]), and $\nu_{1/30}$ is the supernova rate in the Galaxy in units of explosions per 30 years. It can readily be verified that, for $\eta \sim 0.1$ and $\lambda_R \sim 0.1$, the amount of energy in cosmic rays that is absorbed by molecular clouds is higher than the amount of cosmic-ray energy produced in supernovae. In fact, this conclusion can be stated more firmly: with the adopted assumptions, $\dot{E}^{cr}_{SN} \ll \dot{E}^{cr}_{MC}$, which implies that probably $\lambda_R \ll 0.1$. If, in reality, the correlation length is determined by viscosity, then $\lambda_R \sim (\ell/R)^{3/4}$, where ℓ is the mean-free path of the particles ($\ell \ll R$) [6]. Recent numerical modeling of MHD turbulence in molecular clouds [12, 13] suggests that the correlation length is 0.01–0.03 of the scale on which energy is injected into the system, which in our case is the radius of the cloud. To remove this inconsistency between the cosmic-ray energy that could be absorbed in molecular clouds and the cosmic-ray energy produced by supernovae, we must suppose that Galactic cosmic rays interacting with molecular clouds are predominantly reflected, so that only a small fraction of the cosmic-ray energy is lost.

3. REFLECTION OF COSMIC RAYS FROM THE SURFACE LAYERS OF A MOLECULAR CLOUD

According to recent numerical modeling, molecular clouds represent temporary regions of enhanced density arising due to the action of converging flows of interstellar gas [14–17], whose lifetimes, $t_{MC} \sim 2 \times 10^7$–$10^8$ yr, are probably determined by the activity of the stars born in them. In this picture, one of the main sources of turbulent energy in molecular clouds is the kinetic energy of the converging flows, although it is not ruled out that an appreciable amount of energy can be contributed by young stars born in the molecular-cloud cores. During the formation of a molecular cloud, i.e., the transformation of atomic into molecular hydrogen in the presence of an enhanced gas density, some fraction of its rotational angular momentum is lost, but the remaining specific rotational angular momentum of the cloud is still substantial: on average, the specific angular momentum in molecular clouds is a factor of four lower than the specific angular momentum of the interstellar gas. This means that a cloud rotates about 30 times as it is compressed in the converging flows (we have adopted

here a characteristic rotational velocity for the cloud $\Omega \sim 10^{-14}$ s^{-1} [18]). Thus, we expect the magnetic field in the outer parts of the molecular cloud to have a helical structure with an appreciable toroidal component (i.e., the component perpendicular to the rotational axis of the cloud). This type of field structure is indeed observed in a number of cases (such as the cloud Lynds 1641) [19]. In this case, no matter what the angle at which a cosmic ray is incident on the molecular-cloud surface, the pitch angle will reach its critical value as the cosmic ray begins to penetrate into the cloud, causing the cosmic ray to be reflected by the magnetic field. The characteristic time for the reflection of cosmic rays by this process is [5]

$$t_m \sim \frac{\gamma m_p}{p}\left(\frac{\partial \ln B}{\partial s}\right)^{-1} \sim \frac{\gamma m_p L_B}{p}, \qquad (7)$$

where L_B is the length along the trajectory of the cosmic-ray particle over which the regular component of the magnetic field varies, for which it is natural to adopt $L_B \sim R$. The characteristic diffusion time for the cosmic rays is

$$t_D \sim \frac{R^2}{D}. \qquad (8)$$

If we suppose that this diffusion is determined by kinetic processes with cross section $\sigma_i \sim 3 \times 10^{-18}$ cm^2 (the cross section for ionization losses), the diffusion time will be $t_D = (N\sigma_i)^{3/4}R/c$, so that

$$\frac{t_m}{t_D} \sim \frac{1}{(N\sigma_i)^{3/4}} \ll 1. \qquad (9)$$

If the diffusion is determined by resonance scattering on small scales of the order of the gyroradius of a cosmic-ray proton, $l \sim 2\pi r_p$ [5, 6], the diffusion coefficient will be $D \lesssim cR^{1/4}l^{3/4}$, and the ratio of the time scales becomes

$$\frac{t_m}{t_D} \sim \left(\frac{l}{R}\right)^{3/4} \ll 1. \qquad (10)$$

Thus, cosmic rays should be reflected by the enhanced magnetic field of a molecular cloud appreciably more rapidly than they can penetrate into the cloud core. The fraction of cosmic rays that are able to penetrate into the cloud can be crudely estimated using the ratio t_m/t_D, which is to an order of magnitude 10^{-3} in both cases.

This analysis forces us to conclude that the primary ionization rate of the molecular gas is substantially lower than the value that is required in order for the gas–chemical reactions in the cloud to be sustained: $\zeta \sim 10^{-17}$ s^{-1}. Galactic cosmic rays with the spectrum presented above provide to an order of magnitude just this primary ionization rate. Even if about 10% of the high-energy particles can penetrate into the cloud, which could with some margin lead to agreement between $\dot{E}^{cr}_{MC}$ and $\dot{E}^{cr}_{SN}$, ζ would be at least an order of magnitude lower than the required value. This contradiction can be resolved if turbulent motions in the molecular cloud are able to accelerate nonthermal particles to sufficiently high energies to sustain the required level of primary ionization.

4. ACCELERATION OF NONTHERMAL PARTICLES IN A MOLECULAR CLOUD

Molecular clouds display well-developed turbulence, as a rule, supersonic, and probably super-Alfvènic (see the discussions in [4, 12, 20]). It is, accordingly, natural to expect the presence of numerous MHD shock waves in the cloud, as is observed in both numerical simulations (see the discussion in [21]) and in real molecular clouds [22, 23]. The characteristic velocities of MHD shocks in molecular clouds can reach ~10 km/s, in which case it is reasonable to expect that some fraction of their kinetic energy could be transformed into nonthermal particles accelerated in the shock fronts. The efficiency of particle acceleration under these conditions can be estimated using the theory developed in the studies [24–27], which are concerned with the acceleration of particles in the fronts of chaotic shocks in turbulent interplanetary and interstellar fields. In this theory, the maximum energy that can be gained by particles is determined by the ratio of the time over which the acceleration region exists (the time for the shocks to travel through the distance separating them), $t_a \sim L_s/u$, and the time for the diffusion of the particles from the acceleration region, $t_D \sim L_s^2/D$, where L_s is the characteristic distance between the shock fronts and u is the shock velocity [26] (the accelerated particles leave the acceleration zone when $t_D/t_a < 1$). The diffusion coefficient $D = v\Lambda/3$ is determined by the scattering of particles on small-scale inhomogeneities in the magnetic field with a characteristic transport free path $\Lambda \simeq C_\nu L_s(r_b/L_s)^{2-\nu}$, where $C_\nu \simeq 0.3$, $r_p = cp/eB$ is the gyroradius of the particle, p is the momentum of the particle, and ν is the index of the spectrum of the small-scale fluctuations of the magnetic field ($d\langle B^2\rangle/dk \sim k^{-\nu}$, $kL_s \gg 1$ [26, 27]). We will estimate the maximum energy of the accelerated particles E_M from the condition $t_D/t_a = 1$. This yields for the spectral index $\nu = 1.5$

$$E_M \simeq 5 \times 10^{-3} L_{s,R}^2 B_1^2 R_1^2 \text{ GeV} \qquad (11)$$

when $E_M < m_p c^2$ and

$$E_M \simeq 0.1 L_{s,R} B_1 R_1 \text{ GeV} \qquad (12)$$

when $E_M > m_p c^2$; here, $L_{s,R} = L_s/R$, $R_1 = R/(1\text{ pc})$, $B_1 = B/(1\ \mu\text{G})$. Thus, in clouds with

characteristic parameters $B \sim 10\ \mu$G and $R \sim 10$ pc and with $L_s/R \sim 0.01-0.03$, we expect protons to be accelerated to energies $E_M \sim 5-15$ MeV. However, E_M is very sensitive to the index of the magnetic-field fluctuation spectrum: $E_M \propto (u/c)^{1/(2-\nu)}$ in the relativistic limit and $E_M \propto (u/c)^{2/(2-\nu)}$ in the nonrelativistic case. Therefore, with a Kolmogorov turbulence spectrum, $\nu \simeq 1.7$, and shock velocities $u \sim 10$ km/s, the estimates of E_M fall to values of the order of atomic energies. Only detailed observations of the magnetic-field fluctuation spectrum will enable confident determination of whether or not it is possible to accelerate nonthermal particles to high energies in molecular clouds. The most recent numerical simulations of MHD turbulence in molecular clouds suggest that, in most cases, a Kolmogorov spectrum is established near wave numbers $kL/2\pi \gtrsim 10$, but the spectrum becomes appreciably non-Kolmogorov at longer wavelengths (exceeding 0.1 of the cloud radius), where is has an index near zero [12, 13]. Thus, the transition from large scales, corresponding to the energy-injection scales, to the scales on which an inertial regime is established encompasses a broad wavenumber interval. If we associate the possibility of generating cosmic rays with long-wavelength components of the turbulent motions in the molecular cloud, the energy E_M could reach values of 1 GeV or higher.

However, both the steady-state characteristic energy of the nonthermal particles E_* and the spectrum of the generated cosmic rays are determined to a considerable extent by the injected-particle distribution function, i.e., by those particles that, having ended up in an active acceleration region, are able to undergo fairly frequent interactions with the shocks there, and by the fraction of the injected particles in the flow as a whole that intersect the shock front, η. One source of particles that is usually considered is particles that become distinguished from the thermal background during the scattering of fairly energetic protons on forming collisionless shocks. This process is probably not efficient in molecular clouds, because the thermal energy of the particles is too low. Winds from young stars and/or low-energy cosmic rays entrained in the converging flows forming the molecular cloud may serve as a source of particles. In any case, the question remains open and requires a separate analysis; more detailed discussions in application to shocks from supernovae and to the diffuse interstellar and interplanetary media can be found in [24, 26, 28, 29]. The value of the fraction of interacting injected particles η is very uncertain. The injection rate at the bow shock in the magnetosphere of the Earth is $\eta \sim 10^{-3}$ [30]. Estimates carried out in [31] for supernova remnants leave open a very wide interval for η, $10^{-5} < \eta < 10^{-1}$. If we adopt the lower limit for molecular clouds, the characteristic energy of the nonthermal particles proves to be too low. Based on the fact that the characteristic energy of the nonthermal particles should be such that their total energy $W_p \sim \eta n p_*^2/2m_p$ does not exceed the kinetic energy of the generated turbulent motions $W_T \sim \rho u^2/2$, we arrive at the estimate $E_* \lesssim 0.5\eta^{-1} m_p c^2 (u/c)^2 \sim 50$ keV. The Larmor radius of protons with such energies is only $r_p \sim 3 \times 10^9$ cm in a magnetic field of $B \sim 10\ \mu$G, so that the protons should primarily occupy a limited volume near the surface of the accelerating shock.

To estimate the primary ionization rate provided by generated nonthermal particles throughout the molecular cloud, we suppose that only those particles that have diffusion lengths at times $t \sim t_a$ equal to half the distance between the shock fronts (i.e., $\sim L_{s,R} = 1/2$) are able to occupy the cloud volume fairly uniformly and contribute to the ionization of the medium in the cloud. Adopting a power-law spectrum for the nonthermal particles, $dN_p/dE \propto E^{-q}$, and assuming that the total energy contained in these particles is comparable to the energy of the turbulent motions, $\int E dN_p \sim W_T$, we obtain the primary ionization rate

$$\zeta = \int_{E_{M/2}}^{E_M} v(E) \frac{dN_p}{dE} \sigma(E) dE \simeq 3 \times 10^{-18} n\ \text{s}^{-1} \tag{13}$$

for $q = 2$ and

$$\zeta \simeq 3 \times 10^{-19} n\ \text{s}^{-1} \tag{14}$$

for $q = 2.5$; here, n is the gas density in the molecular cloud. Thus, for a mean gas density $n \sim 10^2$ cm^{-3} [32], we find $\zeta \sim 10^{-17}-10^{-16}$ s^{-1}, which is close to the value required to sustain the gas-phase chemistry in the molecular cloud. Note that larger values exceed the value expected from Galactic cosmic rays. We note in this connection that recent observations of some molecular clouds require primary ionization rates that cannot be provided by Galactic cosmic rays. In particular, the value $\zeta = 5.6 \times 10^{-17}$ s^{-1} with an uncertainty factor of about three is preferred in [33]; i.e., the upper end of the allowed interval corresponds to $\zeta \sim 10^{-16}$ s^{-1}. However, even the most probable value exceeds the value expected from Galactic cosmic rays by a factor of five. This serves as an additional argument for the need for additional sources of cosmic rays in molecular clouds and the possible generation of cosmic rays in such clouds.

5. CONCLUSION

(1) The energy lost by Galactic cosmic rays in molecular clouds may exceed the total energy converted into cosmic rays by supernovae.

(2) An appreciable fraction of cosmic rays with energies $E \sim 1$ GeV can be reflected from the surface layers of molecular clouds. Thus, an additional source of nonthermal particles is required to sustain the gas-phase chemical processes occurring in these clouds.

(3) One such source is particles accelerated in the fronts of MHD shocks that arise during the formation of the molecular cloud. The primary ionization rate that can be provided by such particles is $\zeta \sim 10^{-17}-10^{-16}$ s^{-1}.

ACKNOWLEDGMENTS

The author thanks the referee for comments. This work was supported by the Russian Foundation for Basic Research (project no. 02-02-17642), the INTAS foundation (project no. 99-1667), and the German Scientific Society (DFG; project no. SFB 591, TP A6). This work has made use of the NASA Astrophysics Data System Abstract Service.

REFERENCES

1. W. D. Watson, Rev. Mod. Phys. **48**, 513 (1976).
2. E. J. O'Donnell and W. D. Watson, Astrophys. J. **191**, 89 (1974).
3. J. Barsuhn and C. M. Walmsley, Astron. Astrophys. **54**, 345 (1977).
4. P. C. Myers and V. K. Khersonsky, Astrophys. J. **442**, 186 (1995).
5. C. J. Cesarsky and H. J. Völk, Astron. Astrophys. **70**, 367 (1978).
6. T. Nakano and E. Tademaru, Astrophys. J. **173**, 87 (1972).
7. J. A. Simpson, Annu. Rev. Nucl. Part. Sci. **33**, 330 (1983).
8. C. F. McKee, *The Origin of Stars and Planetary Systems*, Ed. by C. J. Lada and N. D. Kylafis (Kluwer Acad., 1999), p. 29.
9. M. H. Heyer and S. Terebey, Astrophys. J. **502**, 265 (1998).
10. E. Falgarone and J.-L. Puget, Astron. Astrophys. **162**, 235 (1986).
11. R. Schlickeiser, *Cosmic Ray Astrophysics* (Springer, Berlin, 2002).
12. J. Cho and A. Lazarian, Phys. Rev. Lett. **88**, 245001 (2002).
13. J. G. Vestuto, E. C. Ostriker, and J. M. Stone, Astrophys. J. **590**, 858 (2003).
14. J. Ballesteros-Paredes, E. Vazquez-Semadeni, and J. Scalo, Astrophys. J. **515**, 286 (1999).
15. E. Vazquez-Semadeni, in *New Perspectives in the Interstellar Medium*, Ed. by A. R. Taylor, T. L. Landecker, and G. Joncas (Astron. Soc. Pacif., San Francisco, 1999), ASP Conf. Ser., Vol. 168, p. 345.
16. W.-T. Kim, E. C. Ostriker, and J. M. Stone, Astrophys. J. **581**, 1080 (2002).
17. R. S. Klessen, Rev. Mod. Astron. **16** (2003).
18. J. P. Phillips, Astron. Astrophys., Suppl. Ser. **134**, 241 (1999).
19. F. J. Vrba, S. E. Strom, and K. M. Strom, Astron. J. **96**, 680 (1988).
20. S. Boldyrev, Astrophys. J. **569**, 841 (2002).
21. P. Padoan, A. A. Goodman, and M. Juvela, Astrophys. J. **588**, 881 (2003).
22. E. Falgarone, J.-L. Puget, and M. Perault, Astron. Astrophys. **257**, 715 (1992).
23. P. C. Myers and C. F. Gammie, Astrophys. J. **522**, L141 (1999).
24. I. N. Toptygin, *Cosmic Rays in Interplanetary Magnetic Fields* (Nauka, Moscow, 1983; Reidel, Dordrecht, 1985).
25. A. M. Bykov and I. N. Toptygin, Zh. Éksp. Teor. Fiz. **98**, 1255 (1990) [Sov. Phys. JETP **71**, 702 (1990)].
26. A. M. Bykov and G. D. Fleishman, Pis'ma Astron. Zh. **18**, 234 (1992) [Sov. Astron. Lett. **18**, 95 (1992)].
27. A. M. Bykov and G. D. Fleishman, Mon. Not. R. Astron. Soc. **255**, 269 (1992).
28. D. C. Ellison and D. Eichler, Astrophys. J. **286**, 691 (1984).
29. R. Blandford and D. Eichler, Phys. Rep. **154**, 2 (1987).
30. M. A. Lee, J. Geophys. Res. **87**, 5063 (1982).
31. L. O'C. Drury, W. J. Markiewicz, and H. J. Völk, Astron. Astrophys. **225**, 179 (1989).
32. J. Bally, *Galactic Structure, Stars and the Interstellar Medium. ASP Conf. Ser*, Ed. by C. E. Woodward, M. D. Bicay, and J. M. Shull (Astron. Soc. Pacif., San Francisco, 2001), ASP Conf. Ser., Vol. 231, p. 204.
33. S. D. Doty, E. F. van Dishoeck, F. F. S. van der Tak, and A. M. S. Boonman, Astron. Astrophys. **389**, 446 (2002).

Translated by D. Gabuzda

Astronomy Reports, Vol. 49, No. 4, 2005, pp. 274–283. Translated from Astronomicheskiĭ Zhurnal, Vol. 82, No. 4, 2005, pp. 308–318.

Analysis of the Dynamical Instability of Several Multiple Stars with Weak Hierarchy

R. Ya. Zhuchkov[1] and V. V. Orlov[2]

[1] *Chair of Astronomy, Kazan State University, Kremlevskaya ul. 18, Kazan, 420008 Russia*

[2] *Sobolev Astronomical Institute, St. Petersburg State University, Universitetskiĭ pr. 28, Staryĭ Peterhof, St. Petersburg, 198504 Russia*

Received April 22, 2004; in final form, September 20, 2004

Abstract—The dynamical stability of 16 multiple stars is analyzed using Monte Carlo simulations with allowance for the errors in the observational data. The analysis was carried out by varying the uncertainties in the initial observational data. Six different stability criteria were considered, and the dynamical evolution was studied using numerical simulations. Eleven of the systems are probably stable, whereas five systems (HD 40887, HD 136176, HD 150680, HD 217675, and HD 222326) are probably unstable (the probability that they are unstable is 0.94 or more according to the results of forward and backward simulations over intervals of 10^6 yr). The results of the simulations were most consistent with the criteria of Mardling–Aarseth (the correlation coefficient between the probabilities of disruption inferred from the stability criterion and numerical integration was $r = 0.998$), Valtonen–Karttunen ($r = 0.998$), and Eggleton–Kiseleva ($r = 0.997$). In about 92–93% of all cases, these criteria yield results that are consistent with the numerical simulations. These criteria also yield high disruption probabilities for the unstable systems. Scenarios for the formation of such systems are discussed: temporary capture of a field star by a close binary, perturbation of a stable multiple system by a massive field object, and disruption of small stellar groups or clusters. The probabilities that these scenarios are realized are analyzed. © *2005 Pleiades Publishing, Inc.*

1. INTRODUCTION

The stability of multiple systems with $N_c \geq 3$ components and weak hierarchy remains a problem for which no final solution has been found (see, e.g., [1–4]).

In our previous paper [5], we analyzed the stability of 16 multiple systems in the framework of the three-body problem using six analytical and empirical stability criteria and numerical simulations of the dynamical evolution of these systems. We showed 11 systems to be stable, whereas our results for five systems suggested possible instability, based on the observational initial conditions—the orbital elements of the subsystems and the component masses.

However, to draw more definitive conclusions about the stability or instability of these systems, we must take into account the fact that orbital parameters and masses are always determined with some uncertainty. Whereas these errors have little effect on the predicted dynamical evolution of systems far from the stability boundary, in the case of a small margin of stability, even a small change in the initial conditions could trigger a transition of the system in question from the domain of stable into the domain of unstable motions or vice versa.

In the current paper, we continue our analysis of the stability of the systems described in our previous paper [5], but now with allowance for the effect of observational errors (Section 2), and discuss various scenarios for the formation of the unstable systems (Section 3). In Section 3 we also compare the results of applying the stability criteria with the results of numerical simulations.

2. ANALYSIS OF THE STABILITY OF THE SAMPLE SYSTEMS

As in [5], we will use six stability criteria for triple systems: the criteria of Golubev [6, 7], Harrington [8, 9], Eggleton and Kiseleva [10], Mardling and Aarseth [11], Valtonen and Karttunen [12], and Tokovinin [13]. In addition, we have carried out numerical simulations of the dynamical evolution of the systems using the TRIPLE code developed by Sverre Aarseth (Cambridge University, United Kingdom), which includes the regularization of close binary encounters [14]. We modified this code somewhat; in particular, we used the criterion of Griffith and North [15] to identify a state of disruption when numerically simulating the evolution of the triple systems.

1063-7729/05/4904-0274$26.00

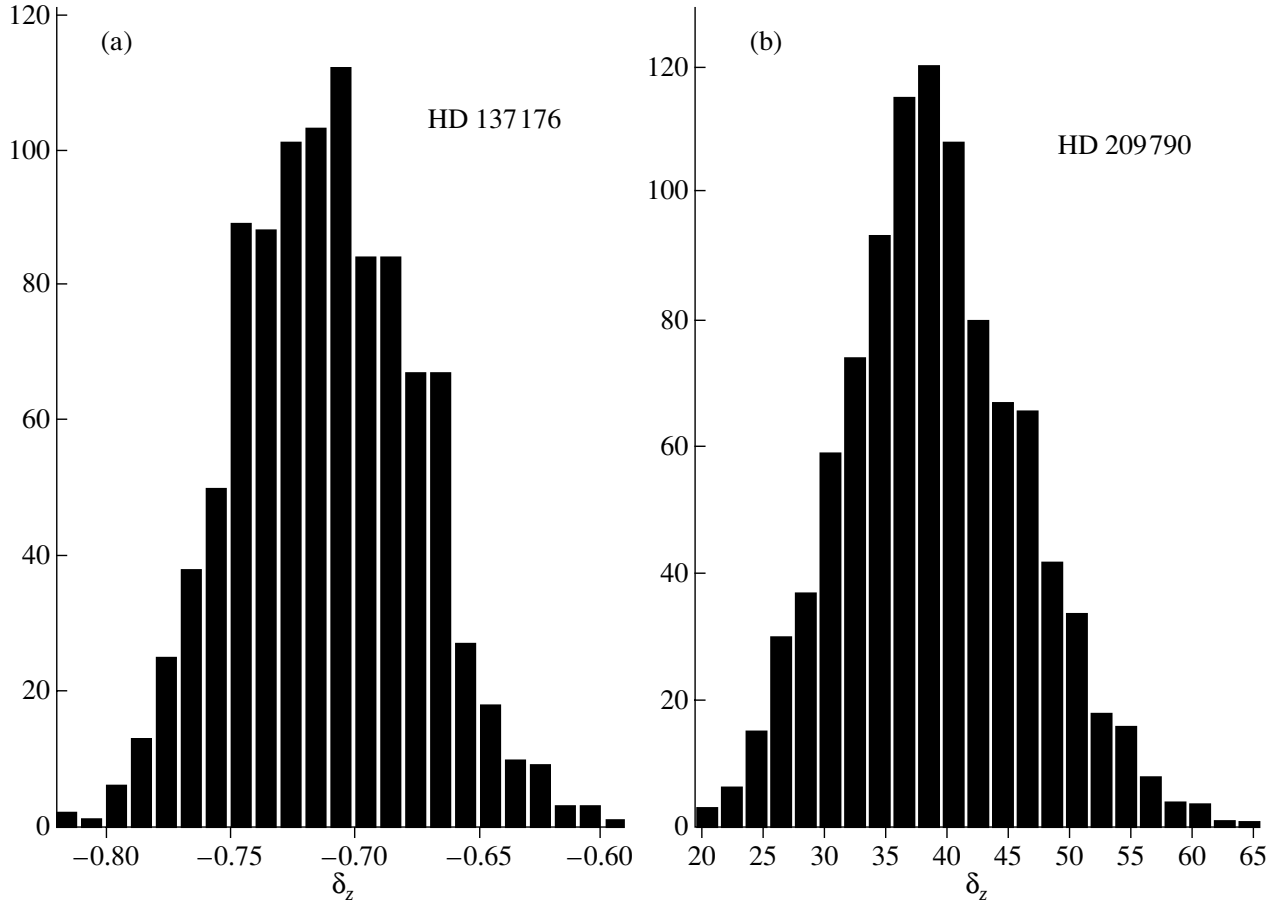

Fig. 1. Distribution of the margin of stability δ_Z according to criterion [11] for (a) the unstable triple system HD 136176 and (b) the stable system HD 209790.

We already described the construction of the sample of objects, its partitioning into subgroups, and our preliminary stability analysis in [5]. Let us briefly summarize the main stages of this analysis.

(1) Selecting systems with published orbital parameters for the inner and outer binaries and published component masses.

(2) Partitioning the sample into subgroups based on the degree of multiplicity and the closeness of the inner binary.

(3) Computing the parameters and margin of stability based on the criteria listed above, and identifying candidate unstable systems.

(4) Computing the dynamical evolution for the candidate unstable systems by numerically integrating the equations of motion using the TRIPLE code.

(5) Comparing the results of the analyses based on the stability criteria and the numerical simulations, and identifying the most adequate stability criterion.

(6) Analyzing various scenarios for the formation of the unstable systems.

2.1. Allowance for the Uncertainties in the Observational Data

We used Monte Carlo simulations to analyze the stability of the 16 systems with allowance for the observational errors in the input data. We adopted the uncertainties in the orbital elements and masses from the literature (see the references in [5]). When the authors of the original papers reported no uncertainties, we determined these uncertainties as follows.

(a) For systems with two orbits published within a short time interval displaying discrepancies comparable to the typical errors in the orbits of binary stars, we set the uncertainties equal to the absolute value of the difference of the corresponding elements.

(b) Otherwise, we set the uncertainties equal to 0.1 of the element in question for periods, semimajor axes, and stellar masses, and set the uncertainties in the zero epoch, eccentricity, and angular elements equal to the uncertainty in the period, 0.1, and 10°, respectively.

(c) We set the uncertainties in the masses equal to $0.1M_\odot$ for stars with masses less than $1M_\odot$, in

Table 1. Instability probabilities for the systems, computed with allowance for the distributions of the initial conditions

Parameter	P_d^+	P_d^-	P_d	P_s	P_F	P_X	P_Z	P_Q	P_T
HD 5408	0.000	0.000	0.000	0.000	0.005	0.000	0.000	0.000	0.000
HD 9770	0.003	0.002	0.002	0.000	0.032	0.000	0.000	0.003	0.024
HD 9770	0.001	0.001	0.003	0.000	0.035	0.000	0.000	0.003	0.020
HD 12376	0.005	0.004	0.005	0.253	0.158	0.000	0.000	0.014	0.186
HD 29316	0.019	0.021	0.033	0.002	0.886	0.000	0.000	0.000	0.420
HD 40887*	0.855	0.868	0.947	0.827	1.000	0.844	0.877	1.000	0.987
HD 56986	0.000	0.000	0.000	0.000	0.000	0.000	0.000	0.000	0.000
HD 98230/1	0.000	0.019	0.019	0.494	0.000	0.000	0.000	0.000	0.000
HD 108500	0.015	0.013	0.016	0.025	0.081	0.008	0.016	0.036	0.522
HD 136176*	0.940	0.937	0.952	1.000	1.000	1.000	1.000	1.000	1.000
HD 150680*	0.998	0.995	1.000	1.000	1.000	1.000	1.000	1.000	1.000
HD 198183	0.028	0.023	0.034	0.000	0.193	0.001	0.012	0.060	0.401
HD 209790	0.000	0.000	0.000	0.000	0.000	0.000	0.000	0.000	0.000
HD 213051/2	0.077	0.080	0.094	0.654	0.217	0.017	0.021	0.028	0.684
HD 217675/6*	0.995	0.996	0.999	1.000	1.000	1.000	0.998	0.999	1.000
HD 218658	0.000	0.000	0.000	0.000	0.000	0.000	0.000	0.000	0.031
HD 222326*	0.940	0.959	0.987	0.887	1.000	0.921	0.983	1.000	1.000

Note: P_d^+ and P_d^- are the probabilities of disruption based on the forward and backward simulations, P_d is the total probability of disruption based on the realizations that are unstable in the backward and/or forward direction, $P_{s,F,X,Z,Q,T}$ is the probability of disruption, which is equal to the fraction of systems that are unstable according to the corresponding criterion (the subscripts denote the criteria of Golubev (s), Harrington (F), Eggleton and Kiseleva (X), Mardling and Aarseth (Z), Valtonen and Karttunen (Q), and Tokovinin (T)). We considered two sets of initial conditions for the systems HD 9770 and HD 209790. We report both results for HD 9770, but the two alternative sets of initial conditions for HD 209790 yielded the same results, and we do not indicate the alternative set of initial conditions for this system. The five likely unstable systems are marked by asterisks.

accordance with the actual accuracy of astrophysical data for low-mass stars.

For the adopted values of each parameter, we generated a random, normal distribution with its mean and dispersion equal to the observed value and the square of the error in this parameter, respectively. We further imposed natural constraints on the parameter values (e.g., orbital eccentricities must be less than unity, stellar masses must be positive, etc.).

The orbital elements of the components of the system and their masses were represented by points in the corresponding multidimensional phase-space distributions. The set of all these points, in turn, represents a probabilistic model for the system and its dynamics. Each parameter set corresponds to a realization of the given system with a probability determined by the errors in the orbital parameters and masses. In our analysis, the errors in different parameters are assumed to be independent of each other.

In this way, we generated for each system a set of 1000 models with various parameters. A statistical analysis of the stability criteria and the results of numerically integrating the equations of motion for these versions of the initial conditions provide insight into probable scenarios for the dynamical evolution of the multiple system considered.

2.2. Analysis of Dynamical Stability

For each of the 16 systems in our sample [5, Table 1], we performed stability computations for each

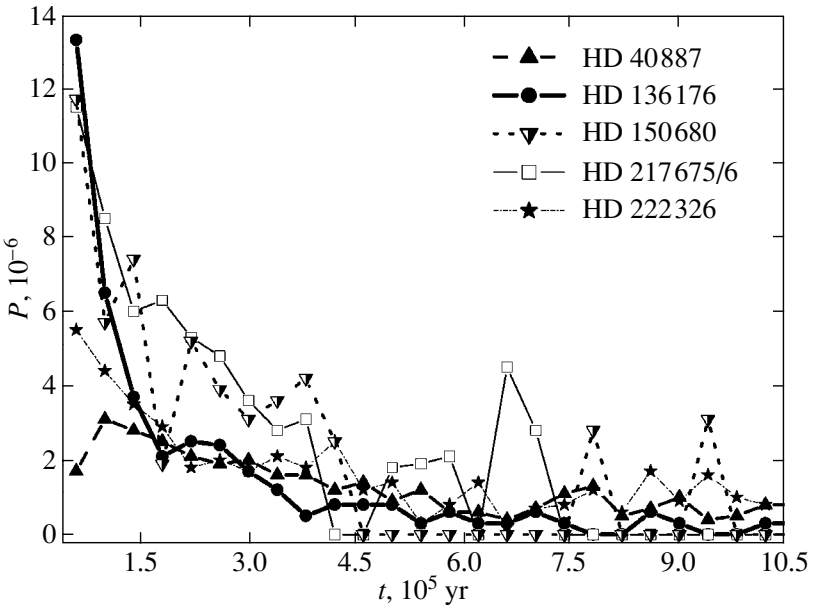

Fig. 2. Time dependence of the specific probability of disruption (per one-year time interval) for the unstable systems.

of the 1000 simulated configurations using the six stability criteria described in [4, 5].

Figures 1a and 1b show the distributions of the parameter δ_i for one probable unstable (HD 136176) and one stable (HD 209790) system. We computed the margin of stability δ_i as

$$\delta_i = \frac{k_i - k_{i_c}}{k_{i_c}}, \qquad (1)$$

where k_i is the value of the stability parameter for stability criterion i, and k_{i_c} is the critical value of this parameter ($\delta_i > 0$ for systems that are stable according to this criterion and, the higher δ_i, the larger the margin of stability). We present the distributions for the stability criterion of Mardling and Aarseth [11]; the distributions for the other criteria are similar.

As is evident from this figure, the distributions of δ_Z are close to normal in both cases. The chief difference between these distributions is that, in the case of HD 136176, the distribution lies completely in the instability domain (all $\delta_Z < 0$), whereas, in the case of HD 209790, it lies completely in the domain of stable motions (for all realizations, $\delta_Z > 0$).

Table 1 lists the probabilities of instability, P_i, for all the criteria, computed as the fraction of systems that are unstable ($\delta_i < 0$) according to a given criterion. To check these computations, we also simulated each system with a set of 10 000 configurations. The results obtained in these simulations agreed with those reported in Table 1 to within 2%.

Note that some of the systems may have their longitudes of the ascending node determined ambiguously (by 180°). The computations performed with the alternative values of the longitudes of the ascending node yielded the same qualitative results.

We also numerically simulated the dynamical evolution of all 16 systems using Monte Carlo simulations for 1001 sets of initial conditions (1000 simulated sets and the initial version). We integrated the equations of motion over a 10^6 yr time interval, which exceeds $1000P_{out}$ for all the systems studied except for HD 108500 (where P_{out} is the orbital period of the outer binary). We integrated the equations of motion for this last system over of 2.5×10^6 yr, which is $\sim 10^3 P_{out}$.

We integrated each system over 10^6 yr in the past and in the future, with the corresponding disruption fractions in Table 1 designated P_d^+ (forward simulation) and P_d^- (backward simulation). Table 1 lists the probabilities of disruption for the forward and backward evolution, together with the total instability probabilities P_d, equal to the fraction of systems that are unstable in at least one of the cases.

It is evident from Table 1 that these multiple systems separate clearly into two populations. The first population consists of 11 likely stable systems whose disruption probabilities P_d do not exceed 10%, according to our numerical simulations (see the detailed description of the simulations below). This is in qualitative agreement with the criteria-based estimates of the instability probabilities P_i. Although some criteria yield discrepant stability estimates in some cases, this may be due to the inaccuracy of the criteria themselves.

Table 2. Parameters of the dynamical evolution of the unstable systems (for an evolution time of 10^6 yr)

Parameter	HD 40887	HD 150680	HD 136176	HD 217675/6	HD 222326
$\bar{t}_d^+$, years	172050	10660	41550	17080	77360
σ_t, years	190120	47240	100090	51200	146260
$\bar{t}_d^-$, years	183440	8850	35240	17210	83020
σ_t, years	203640	29160	72050	47440	158390
$t_{1/2}$, years	39950	7550	30280	15350	56350
$\bar{t}_d^+/P_{out}$	440	309	208	249	511
$\bar{t}_d^-/P_{out}$	470	257	176	251	548
$t_{1/2}/P_{bin}$	1155	576	1030	1687	3782

Note: $\bar{t}_d$ is the mean disruption time (subscripts "+" and "−" correspond to forward and backward evolution, respectively), σ_t are the standard deviations of the disruption times, $t_{1/2}$ is the median disruption time (backward plus forward evolution), P_{out} is the observed period of the outer pair of the corresponding system, and P_{bin} is the initial period of the inner binary (after disruption of the triple system in the case of backward evolution).

Two systems (HD 56986 and HD 209790) had a high margin of stability according to all the criteria [5, Table 3], and these systems are certainly stable.

The second population consists of five systems whose disruption probabilities P_d exceed 94%. The stability criteria also indicate the likely instability of these systems. These data lead us to conclude that, in the case of unstable systems, we may be dealing with dynamically young objects.

Some of the systems that were stable over the time period covered by the computed evolution showed some tendency for disruption over longer times, albeit with lower probability. For example, increasing the integration time period for HD 136176 from 10^6 to 10^7 yr decreased the number of surviving configurations by a factor of 1.3 (from 60 to 46) and increased the probability of disruption from 0.940 to 0.954. The same increase in integration time for HD 222326 decreased the number of surviving configurations by a factor of five (from 61 to 12) and increased the probability of instability from 0.940 to 0.988. At the same time, increasing the integration time for the stable system HD 198183 by the same amount increased the probability of disruption from 0.028 to 0.065 (by a factor of 2.3)—37 more systems disrupted. However, most of the versions (more than 90%) remained stable.

Note that the triple systems considered by Agekyan *et al.* [16] and Anosova and Orlov [17], who analyzed random samples of initial conditions, were "nonaging;" i.e., the distribution of lifetimes was approximately consistent with a radioactive decay law. This is not true in our case—see Fig. 2, which shows the time dependence of the probability of disruption, $P(t)$, defined to be the number of systems that disrupt per unit time divided by the total number of unstable configurations at the given time. In the case of radioactive decays, this probability should be independent of time. It is evident from Fig. 2 that $P(t)$ rapidly decreases at small times, and then approaches a constant value with increasing t. At the same time, the distribution of disruption times is not Gaussian, although all the initial parameters are normally distributed.

Reversing the direction of the simulations (forward/backward) has no qualitative effect on the form of the disruption-time distribution. As is evident from Tables 1 and 2, the disruption probabilities and mean lifetimes are not very different for the different directions of the simulations.

3. DISCUSSION OF THE RESULTS

On the whole, comparison of the disruption probabilities computed according to the stability criteria with the results of the numerical simulations showed good agreement for all the criteria employed. Figure 3 shows the decay probabilities based on the stability criteria plotted against on the decay probabilities based on the numerical simulations. As expected, the escape probabilities for the triple systems with high margins of stability are close to zero. Some criteria yield overestimated disruption probabilities for stable systems near the instability boundary. Some of the criteria appear to have substantially overestimated their stability boundaries. The results for unstable

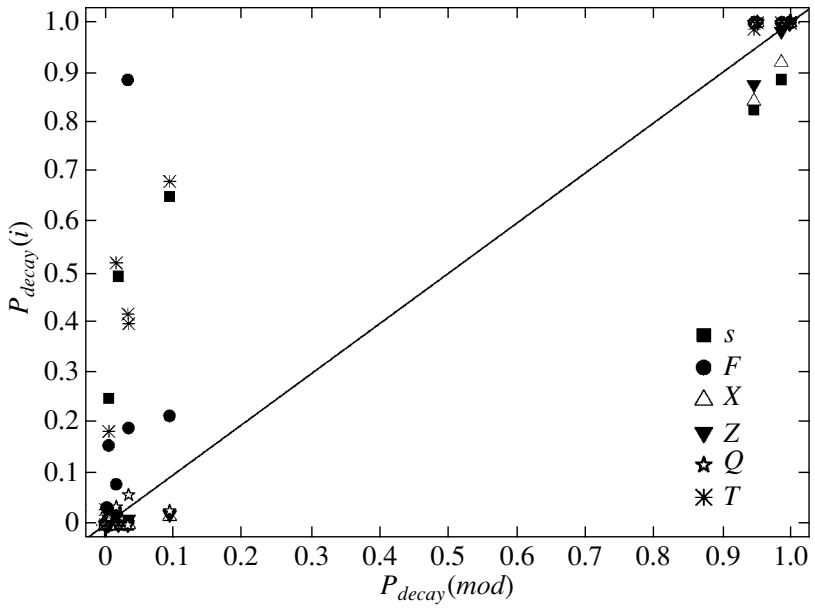

Fig. 3. Dependence of the probability of disruption of a system according to the various criteria, $P_{decay}(i)$, on the probability of disruption according to the numerical simulations, $P_{decay}(mod)$. The different symbols correspond to different criteria, and the letters correspond to those in Table 1. The solid line shows the diagonal of the plot. The fact that $P_{decay}(i) > P_{decay}(mod)$ for small disruption probabilities indicates a shift of the instability boundary for a number of criteria (see text for discussion).

systems are close to those based on the numerical simulations.

Table 3 gives the correlation coefficients for the correlations between the disruption probabilities based on the stability criteria and those based on the numerical simulations. The simulation results are most consistent with the results for the criteria of Mardling and Aarseth (correlation coefficient $r = 0.998$), Valtonen and Karttunen ($r = 0.998$), and Eggleton and Kiseleva ($r = 0.997$).

Table 3 also lists the fractions of coincidences, ν_i, between the results of the stability analyses based on the numerical simulations and on each criterion—$\nu_i = N_{coin}/N_{tot}$. Here, N_{coin} is the total number of coincidences (i.e., cases where both the criterion and simulations indicated stability or instability of the given configuration) and N_{tot} is the total number of versions. We also analyzed the agreement between the configurations of the systems found to be unstable according to the simulations and each of the criteria, and determined the fraction of coincidences for systems found to be unstable according to each criterion and according to the numerical simulations. We measured this agreement using the ratios $\nu_{mod} = N_{mod}/N_{com}$ and $\nu_{crit} = N_{crit}/N_{com}$. Here, N_{com} is the number of realizations found to be unstable in both cases, N_{mod} is the number of versions found to be unstable according to the numerical simulations, and N_{crit} is the number of systems found to be unstable according to the given criterion.

It is evident that, although there is a high degree of agreement between unstable configurations according to the criteria of Harrington and Tokovinin and objects found to be unstable according to the numerical simulations, the number of these agreements is fairly small compared to the total number of unstable objects according to these criteria. This indicates that most of the systems found to be unstable according to the numerical simulations were also predicted to be unstable by these instability criteria; however, at the same time, these criteria overestimated the total number of unstable configurations by a factor of two compared to the numerical simulations. The remaining four criteria yield similar values of ν_{mod} and ν_{crit}, close to 0.7–0.8.

The quantity ν_i, which indicates the fraction of agreements between the stability characteristics based on each criterion and on the numerical simulations, is maximum for three criteria—those of Eggleton and Kiseleva [10], Mardling and Aarseth [11], and Valtonen and Karttunen [12]. These criteria appear to have somewhat different sensitivities for different versions of the initial conditions, and the combined use of these three criteria may ensure more thorough analyses of various systems.

Thus, five systems in the sample (HD 40887, HD 136176, HD 150680, HD 217675, and HD 222326) are probably unstable on time scales of the order 10^6 yr or less. Allowance for the observational errors had no effect on our conclusions

Table 3. Correlation coefficients r between the disruption probabilities according to the stability criteria and numerical simulations

Criterion	r	ν_i	ν_{mod}	ν_{crit}
Golubev [6, 7]	0.910 ± 0.042	0.84	0.77	0.74
Harrington [8, 9]	0.900 ± 0.047	0.86	0.83	0.57
Eggleton and Kiseleva [10]	0.997 ± 0.002	0.92	0.65	0.82
Mardling and Aarseth [11]	0.998 ± 0.001	0.92	0.68	0.82
Valtonen and Karttunen [12]	0.998 ± 0.001	0.93	0.75	0.75
Tokovinin [13]	0.900 ± 0.047	0.87	0.79	0.50

Note: ν_i are the fractional agreements between the results obtained for the numerical simulations and for each of the criteria, ν_{mod} are the fractions of the disruptions among the configurations that are unstable according to the simulations, and ν_{crit} are the fractions of disruptions among the configurations that are unstable according to each of the criteria (see text for additional comments).

with regard to the stability of these systems, although the effect of taking these errors into account may be underestimated for some of the systems. Should this be the case, our conclusions about the stability or instability of a particular system may change.

The few unstable realizations of stable systems are probably due to errors in the initial data. It is obvious from Fig. 4 that the distributions of stable and unstable configurations for the stable system HD 198183 are shifted relative to each other. The lack of a well-defined boundary between these distributions may be due to the complex structure of the stability boundary in the parameter domain considered, as well as the possible effect on the stability of the system of other parameters that are not represented on the diagram.

Figure 5 shows the same distributions for the unstable system HD 136176. In this case, the distributions for the stable and unstable realizations overlap. This can be interpreted as predicting the future disruption of all (or of the overwhelming majority) of the systems that have remained stable by the end of the simulations. However, here, too, the stability may be affected by other parameters not represented on the diagram.

Since it is difficult to explain the instability of all the unstable multiple systems that we have identified as a result of young physical ages, other factors must be invoked to interpret these results—if, of course, they cannot be explained as an effect of the observational errors.

According to one hypothesis, such objects form as a result of encounters between binary (or multiple) systems and single stars or other multiple systems in the Galactic field or in a cluster. In this way, a temporary multiple system can form, which is unstable on long time intervals. Triple systems formed in this way have a median lifetime of $\sim 500 P_{bin}$, where P_{bin} is the orbital period of the binary before the encounter [18]. In this case, the distribution of the lifetimes of these systems has a long "tail" of long-lived systems, which, on the whole, is consistent with the data listed in Table 2 (the last row). It is important that the probability that this process is realized differs little from the probability of a binary encounter in the Galactic field (or in a cluster), since two-thirds to three-quarters of stars belong to binary or multiple systems (see, e.g., [19, 20]) and the probability of an encounter between two single stars is of the order of 0.1.

The probability of capture as a result of an encounter depends on the impact parameter and the relative velocity of the objects, as well as on the time during which the stars interact with each other and the space density of stars. In our case, the impact parameter does not exceed 100 AU, and we model the distribution of residual stellar velocities as a superposition of three independent normal distributions, setting the standard deviations of these distributions equal to 30 km/s. Our computations then show that the local solar neighborhood (a sphere of radius $\sim$200 pc) may contain several such systems.

Note that at least one of the five unstable systems (HD 217675/6) may belong to the moving group associated with the open cluster α Per, as follows from the similarity of the space velocities and positions of this star and the cluster. The stable triple system HD 5408 may also belong to the corona of this cluster. The estimates show that the probability of capture in a moving group may be somewhat higher than in the Galactic field. It is possible that other such systems may also belong to groups or clusters.

Another possible scenario involves an encounter between a stable multiple system and a massive object (molecular cloud, black hole, stellar cluster, etc.) that perturbs the motion of the system and leads to

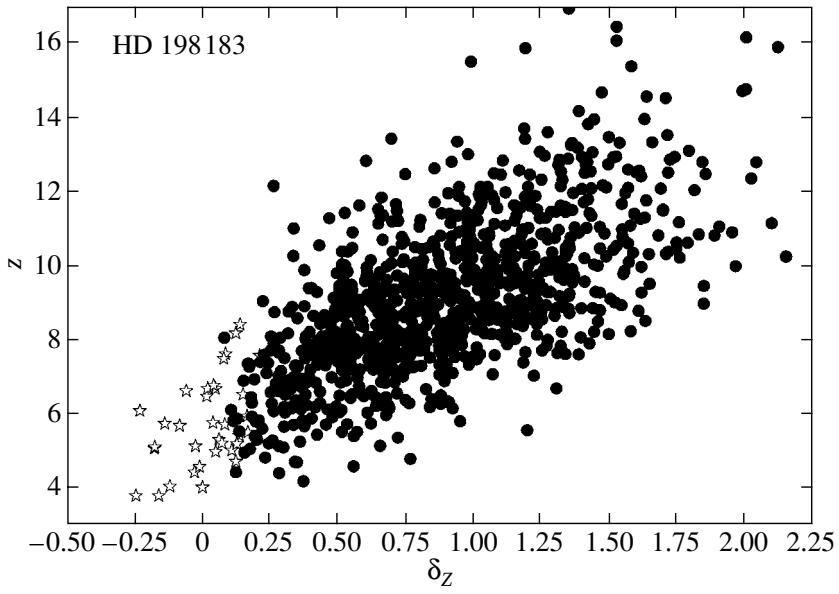

Fig. 4. Distribution of stable and unstable realizations of the system HD 198183. The horizontal axis plots the margin of stability δ_Z according to the criterion of Mardling and Aarseth and the vertical axis the combination $z = a_{out}(1 - e_{out})/(a_{in}(1 + e_{in}))$, which is sensitive to the dynamics of the system. The filled circles and hollow stars indicate stable and unstable realizations, respectively. We integrated the evolution of the system for one million years backward and forward.

its subsequent disruption. We estimated the expected number of such events; here, the impact parameter corresponds to the distance at which tidal acceleration begins to appreciably affect the dynamics of the components, i.e., it exceeds 0.1 of the characteristic acceleration in the system. The number of unstable systems formed in this way proved to be comparable to the number of captures to an order of magnitude (see above).

Both mechanisms may operate in the solar neighborhood, although the probability of observing systems formed via either of these mechanisms is low.

Another possible mechanism involves the disruption of small groups or open clusters during their dynamical evolution. In this case, the observed systems may be produced by the dissipation ("evaporation") of such clusters or their remnants in the final stage of their disruption. Such groups can initially consist of 10^1-10^3 objects. Although the lifetimes of triple systems are small, the dynamical youth of these objects may be a result of their relatively recent formation. At the same time, the population of unstable multiple systems is constantly replenished, since the formation and disruption of groups in the Galactic disk is a continuous process.

We will adopt several assumptions in order to obtain an upper limit for the number of such objects.

(1) We assume that the disruption of triple systems is a process that behaves similarly to radioactive decays (although the actual process might look nothing like this; see Fig. 2 and discussion in the text).

(2) We assume that the disruption of clusters follows a similar law; i.e., the mean time for the escape of one star (the inverse escape rate) is constant and independent of the number of stars in the cluster. Support for this assumption can be found in the papers by de la Fuente Marcos [21–24] (see, e.g., Table 2 and Figs. 7–10 in [24]), who used numerical simulations of the dynamics of open clusters to show that the inverse escape rate is approximately constant and equal to $\approx 1.5 \times 10^6$ yr during the evolution of clusters initially consisting of $N_0 = 100-750$ objects.

Note that the evaporation rate decreases as the number of stars in the cluster decreases, and this decrease is different for clusters with different mass distributions for their stars. However, unstable triple systems can form from groups of different ages and different initial populations, and even an appreciable increase in the time before the escape of each next star (as is the case with small stellar groups consisting of $N < 30$ objects) should not significantly affect the quantitative estimates.

At the same time, a detailed analysis of this issue, in particular, determination of the dependence of the dissipation rate on the cluster parameters, requires a special investigation.

(3) We also assume that, as clusters form, their mass distribution (and the distribution of the number of objects they contain, provided that the mean mass of a cluster star can be assumed to be independent of

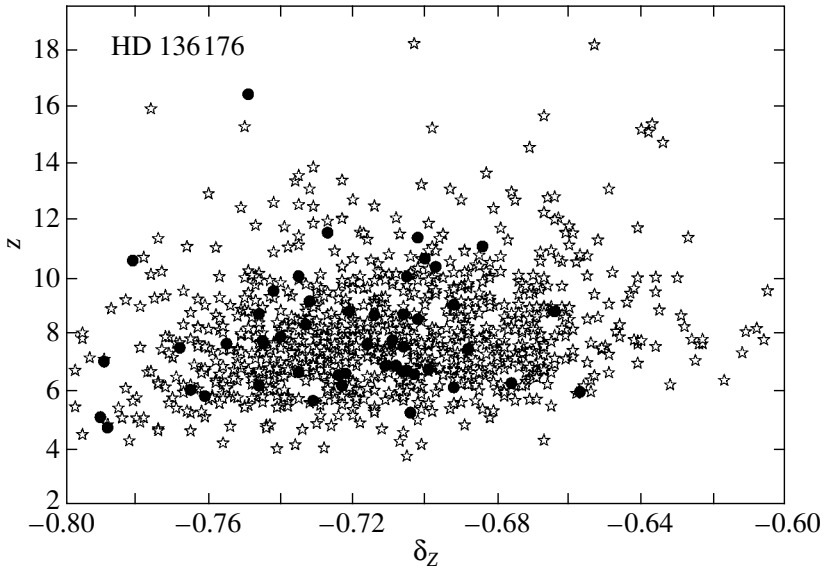

Fig. 5. Same as Fig. 4 for HD 136176.

the mass of the cluster) obeys the law:

$$f(N_0) = kN_0^{-2}. \quad (2)$$

Surdin [25] reported this result for stellar groups with 10^2–10^7 objects, and this relation can be extrapolated to smaller groups (down to $N_0 = 4$) based on the results of Larson [26].

(4) We assume that the total mass of stars formed as a result of the evaporation of clusters is equal to the total mass of stars that formed in the given region during the same time. We adopted this assumption based on the analysis of Larson [27], who argues that most stars form in small groups and clusters.

(5) We finally assume that all triple systems formed via dissipation that are now observable are unstable. This assumption can also be used to obtain upper limits for the number of such objects, but simulations of this process [28] have shown that a high fraction (about 50%) of triple systems that formed as a result of the disruption of small groups are unstable.

We found, based on these assumptions, that several unstable triple systems should have formed within 200 pc of the Sun during the past ten billion years, so that we should now observe several such unstable triple systems.

Thus, different scenarios for the formation of such systems yield comparable probabilities for the formation of these dynamically young objects in the relatively recent past, although the total number of such objects in the solar neighborhood is small: there are certainly no more than $\sim 10^2$ systems with outer-pair periods of less than 1000 yr.

More certain identification of the most likely scenario for the formation of particular observed probable unstable systems requires a more detailed analysis of these systems, as well as determination of the physical properties of their components. In particular, significant age and chemical composition differences between the components may be indicative of a capture.

At the same time, we must try to refine the orbital parameters of the systems studied, in order to reduce the effect of errors in these parameters and make possible more definitive conclusions about their instability. This especially concerns the systems HD 136176, HD 150680, and HD 217675/6; the systems HD 40887 and HD 222326 already have reliably determined orbits.

ACKNOWLEDGMENTS

This work was supported by the Program of Support for Leading Scientific Schools of Russia (grant no. 1078.2003.02), the Russian Foundation for Basic Research (project no. 02-02-17516), and the Universities of Russia Program of the Ministry of Education and Science of the Russian Federation (grant no. UR.02.01.027).

REFERENCES

1. V. Szebehely and K. Zare, Astron. Astrophys. **58**, 145 (1977).
2. F. C. Fekel, Astrophys. J. **246**, 879 (1981).
3. J. R. Donnison and D. F. Mikulskis, Mon. Not. R. Astron. Soc. **272**, 1 (1995).

4. V. V. Orlov and A. V. Petrova, Pis'ma Astron. Zh. **26**, 301 (2000) [Astron. Lett. **26**, 250 (2000)].
5. R. Ya. Zhuchkov and V. V. Orlov, Astron. Zh. **82**, 231 (2005) [Astron. Rep. **49**, 201 (2005)].
6. V. G. Golubev, Dokl. Akad. Nauk SSSR **174**, 767 (1967) [Sov. Phys. Dokl. **12**, 529 (1967)].
7. V. G. Golubev, Dokl. Akad. Nauk SSSR **180**, 308 (1968) [Sov. Phys. Dokl. **13**, 373 (1968)].
8. R. S. Harrington, Celest. Mech. **6**, 322 (1972).
9. R. S. Harrington, Astron. J. **82**, 753 (1977).
10. P. Eggleton and L. Kiseleva, Astrophys. J. **455**, 640 (1995).
11. R.-M. Mardling and S. J. Aarseth, *The Dynamics of Small Bodies in the Solar System, a Major Key to Solar System Studies*, Ed. by B. A. Steves and A. E. Roy (Kluwer, Dordrecht, 1999), p. 385.
12. M. Valtonen and H. Karttunen, *Three-Body Problem in Astrophysics* (Cambridge Univ. Press., Cambridge, 2005, in press).
13. A. A. Tokovinin, Rev. Mex. Astron. Astrofis. (Ser. Conf.) **21**, 7 (2004).
14. S. J. Aarseth and K. Zare, Celest. Mech. **10**, 185 (1974).
15. J. S. Griffith and R. D. North, Celest. Mech. **8**, 473 (1974).
16. T. A. Agekyan, Zh. P. Anosova, and V. V. Orlov, Astrofiz. **19**, 111 (1983) [Astrophys. **19**, 66 (1983)].
17. Zh. P. Anosova and V. V. Orlov, Tr. Astron. Obs. Leningrad. Univ. **40**, 66 (1985).
18. P. Hut, Astrophys. J. **403**, 256 (1993).
19. A. Duquennoy and M. Mayor, Astron. Astrophys. **248**, 485 (1991).
20. M. Mayor, S. Udry, J.-L. Halbwachs, and F. Arenou, in *IAU Symp. No. 200: The Formation of Binary Stars, Potsdam, Germany, 2001*, Ed. by H. Zinnecker and R. D. Mathieu, p. 45.
21. R. de la Fuente Marcos, Astron. Astrophys. **301**, 407 (1995).
22. R. de la Fuente Marcos, Astron. Astrophys. **308**, 141 (1996).
23. R. de la Fuente Marcos, Astron. Astrophys. **314**, 453 (1996).
24. R. de la Fuente Marcos, Astron. Astrophys. **322**, 764 (1997).
25. V. G. Surdin, Pis'ma Astron. Zh. **21**, 574 (1995) [Astron. Lett. **21**, 508 (1995)].
26. R. B. Larson, in *Clouds, Cores, and Low Mass Stars*, Ed. by D. P. Clemens and R. Barvainis (Astron. Soc. Pacif. Conf. Ser., San Franisco, 1994), ASP Conf. Ser., Vol. 65, p. 125.
27. R. B. Larson, in *IAU Symp. No. 200: The Formation of Binary Stars, Potsdam, Germany, 2001*, Ed. by H. Zinnecker and R. D. Mathieu, p. 93.
28. A. V. Rubinov, A. V. Petrova, and V. V. Orlov, Astron. Zh. **79**, 1044 (2002) [Astron. Rep. **46**, 942 (2002)].

Translated by A. Dambis

Astronomy Reports, Vol. 49, No. 4, 2005, pp. 284–294. Translated from Astronomicheskiĭ Zhurnal, Vol. 82, No. 4, 2005, pp. 319–330.

Two- and Three-Dimensional Hydrodynamical Simulations of Mass Transfer in Semidetached Binaries with Explicit Radiative Cooling and Self-Absorption in Their Gaseous Envelopes

V. V. Nazarenko, L. V. Glazunova, and L. S. Shakun

Astronomical Observatory, Mechnikov National University, Shevchenko Park, Odessa, 270014 Ukraine

Received February 4, 2004; in final form, September 20, 2004

Abstract—We have modeled the mass transfer in three Algol-type binaries using two- and three-dimensional numerical hydrodynamical techniques. Radiative cooling and absorption in the envelopes surrounding the components of the close binaries are explicitly taken into account. The resulting envelope temperatures are consistent with those observed. We derived these temperatures by considering the energy balance in the moving gas, including heating due to the numerical viscosity that is inherent to the simulations and radiative cooling. The radiative cooling was calculated assuming an optically thin plasma in a state of ionization balance. Taking into account both of these processes yielded temperatures of 4000–30 000 K in the disk around the accreting primary and in the common envelope surrounding the close binary. Our computations also indicate that the envelope morphology is not sensitive to the radiative-cooling model used. © *2005 Pleiades Publishing, Inc.*

1. INTRODUCTION

Simulations of mass transfer in close binary systems have been carried out in numerous studies. The mass outflow from the Lagrangian point L_1 and the formation of an accretion disk and circumstellar envelopes have been modeled using two- and three-dimensional hydrodynamical computations. The most important and interesting results have been obtained by Sawada *et al.* [1], Różyczka and Spruit [2], Spruit [3] (two-dimensional computations), Molteni *et al.* [4], Hirose *et al.* [5], Lanzafame *et al.* [6, 7], Sawada and Matsuda [8], Meglicki *et al.* [9], Whiteburst [10], Simpson [11], Armitage and Livio [12], Yukawa *et al.* [13], and Bisikalo *et al.* [14–16] (three-dimensional computations).

In these studies, one of the main problems was to reach consistency with the observed temperatures in the disks and circumstellar envelopes [14–16]. Unfortunately, due to the numerical viscosity inherent to the simulation techniques used, the temperatures in the disk and envelope turned out to be very high—hundreds of thousands of degrees or more. It is obvious that such temperatures cannot be real. Observations of spectral lines formed in disks or envelopes indicate temperatures of the order of tens of thousands or thousands of degrees [17]. The higher temperatures resulting from the numerical viscosity, particularly in three-dimensional computations, lead to the expansion of the gas outwards in the orbital plane, under the action of the artificially high gas pressure. Accordingly, the gaseous structures formed around the accretor only vaguely resemble disks (the gas in these structures essentially does not rotate around the central object, simply leaving the system instead). As a result of heating due to numerical viscosity, accretion disks are formed in three-dimensional computations only when γ is smaller than 1.2 [4]. The only way to obtain temperatures in hydrodynamical computations that are close to those observed in envelopes is to consider all aspects of the energy balance in the gas flows in the envelope, taking into account all factors affecting the temperature. These are primarily heating and cooling due to the action of radiation on the moving gas, as well as convective thermal conduction. Radiative cooling must be explicitly taken into account. When this is done implicitly, by decreasing the ratio of specific heat capacities, the temperatures in the computational domain remain far from the observed values. It is also clear that heating of the disk and envelope by X-ray radiation from central regions of the accretion disk is important only for systems with a compact object. Therefore, for systems in which both components are normal stars, we can restrict our consideration to radiative cooling. Also, for simplicity, our computations do not take into account convective heat conduction.

The first attempt to include radiative cooling in hydrodynamical computations of gas motions in close binaries was made by Blondin *et al.* [18], who used

1063-7729/05/4904-0284$26.00

the radiative-cooling function for an optically thin cosmic plasma in a state of ionization balance (the MOTCAPIE model) to model the formation of a transient accretion disk in β Per as a function of the density of matter in the disk. Cox and Daltabuilt [19] essentially obtained their cooling function by taking into account radiative losses in induced O and C lines. In [20], we used this radiative-cooling model in two-dimensional computations of the mass transfer in three semidetached close binaries (RZ Sct, U Cep, and V373 Cas) whose components rotate asynchronously (those computations were made to investigate the possibility that the asynchronous rotation of both components was associated with mass transfer through L_1, with subsequent accretion). However, due to the large rate of mass transfer through L_1 in these systems ($10^{-6} M_\odot$ yr^{-1}), and, accordingly, the high density of the matter in the envelope (10^{12}–10^{13} cm^{-3}), the energy radiated per unit volume becomes very large, so that virtually all the thermal energy in the envelope is radiated away, and the temperature approaches the lowest value in the MOTCAPIE model (around 1000 K). Like temperatures of hundreds of thousands of degrees, such low temperatures for the envelopes are also unrealistic. This indicates that the absorption of radiation must be taken into account when the density in the envelopes exceeds 10^{10} cm^{-3}. When this is done in the de-excitation function, the computed temperatures in the envelope and accretion disk can approach their real values. The effect of absorption on the computed temperatures in the moving gas in close binaries is obvious and very simple: for temperatures exceeding 15 000–20 000 K, the absorption in the envelope and disk is small, and energy is radiated very efficiently in these structures; when the temperature decreases to 10 000–15 000 K, the absorption increases, radiation almost ceases, and the temperature ceases to decrease. Thus, when absorption is taken into account in the de-excitation function, the temperature in the moving gas will be specified by the joint action of numerical viscosity and radiative cooling, and will be of the order of tens of thousands or thousands of degrees.

Here, we present the results of two- and three-dimensional hydrodynamical computations of mass transfer in the three Algol-type close binaries RZ Sct, V373 Cas, and U Cep using the MOTCAPIE model, including the effects of radiative cooling and absorption in the envelope and accretion disk.

2. MASS TRANSFER MODELS EXPLICITLY TAKING INTO ACCOUNT RADIATIVE COOLING

We explicitly included radiative cooling in our computations, using the MOTCAPIE model, which expresses the energy radiated per unit volume of gas at all wavelengths per unit time as a function of temperature. We take into account absorption in the envelope and disk by multiplying the de-excitation function by $e^{-\tau}$, where τ is the optical depth in the continuum near the Hα line. This quantity is calculated in the z direction, normal to the orbital plane (we assume that the disk and surrounding envelope are optically thick in the direction of the orbital plane). Note that multiplication of the de-excitation function by $e^{-\tau}$ does not follow from the solution of the transfer equation, and is merely a phenomenological practice that makes it possible to correctly take into account the absorption of radiation produced by de-excitation in the envelopes of the close binaries. The optical-depth calculations assumed LTE; i.e., the number of ionized atoms and hydrogen atoms in the upper level was calculated using the Saha and Boltzmann equations. Our two-dimensional computations of the mass transfer assumed that the heights of the envelope and accretion disk surrounding the accretor are equal to the accretor's radius.

This two-dimensional model of mass transfer in a close binary is similar to that used in our previous studies [20, 21], which assumed that the donor loses mass only from the vicinity of L_1 (i.e., mass loss via the donor stellar wind was neglected). We used Kurucz [22] model stellar atmospheres to construct the initial model atmosphere for the donor in the vicinity of L_1 and simulate the formation of a flow around this point. The nonstationary hydrodynamical equations in Euler form were solved using the method of "large particles" developed by Belotserkovskiĭ and Davydov [23]. Our version of this technique includes artificial viscosity in the first time sub-step, to ensure stability of the computations and obtain the second order accuracy in the time and space coordinates.

Since taking radiative cooling into account in this way results in instability of the computations in some cases, we introduced a special technique in the method of large particles—so-called regularization of the temperature field, which makes the computations stable even in the presence of radiative cooling. The essence of this modification is that, when the temperature in a cell exceeds $T_{\rm prev}$ at the end of a given time step, this temperature is assumed to be equal to the temperature in the first stage of the computations for the given time step, which corresponds to some version of gas cooling. Recall that, in the method of large particles, the parameters of the gas flow in a given cell are calculated in two stages at each time step. In the first stage, the effects of gas pressure and external fields in the computational domain are determined (in our case, the external field is the gravitational field). In the second stage, the mass, momentum, and internal energy transferred through

Parameters of the systems

System	Spectral type	P_{orb}, days	q	$\dot{M}$, $M_\odot$/yr	M_{accr}, $M_\odot$	$R_{accr}/A\,(A=1)$
V373 Cas	B1(II-Ib)+B0.5III	13.4	0.74	10^{-5}–10^{-6}	14	0.15
U Cep	B7V+G8IV	2.49	1.49	10^{-6}–10^{-7}	3.6	0.18
RZ Sct	B1Ib+A2IV	15.2	5.26	10^{-6}	16.3	0.17

the cell boundaries are calculated taking into account the velocities obtained in the first stage, and the final parameters for the given time step are determined. Thus, heating of the moving medium by numerical viscosity, which is inherent to the method, is limited.

We used a standard model for a binary system: the gravitational fields of the binary components were calculated in a Roche approximation, all effects of rotation in the binary (Coriolis and centrifugal forces) were taken into account, and it was assumed that the components' orbits were circular and that their orbital motion about their common center of mass was synchronous with their rotation about their own axes. To simulate the interaction between the flow from L_1 and the accretor's surface, we introduced a factor f_v specifying the accretion rate at the accretor's surface ($f_v = 0$ if there is no accretion and $f_v = 1$ if all the matter reaching the surface is accreted onto it). In our computations, we adopted $f_v = 0.5$.

As we noted in the Introduction, we considered the formation of gaseous structures in three Algol-type systems: RZ Sct, V373 Cas, and U Cep, whose mass-transfer rates are of the order of 10^{-6} $M_\odot$/yr. The table presents the parameters of these close binaries: the columns contain the (1) name of the system, (2) spectral types of the components, (3) orbital period of the system in days, (4) component-mass ratio $q = M_{accr}/M_{donor}$, (5) observed rate of mass transfer through L_1, and (6)–(7) mass and radius of the accretor in solar units.

3. RESULTS OF THE COMPUTATIONS

3.1. Results of the Two-dimensional Hydrodynamical Simulations

The computations were carried out as follows. For the first three orbital periods, radiative cooling was only implicitly taken into account, with the polytropic factor $\gamma = 0.65$. The radiative cooling was then switched on in the third orbital period (so that the accretion disk and surrounding envelope formed without being influenced by radiative cooling). The computations continued until a steady state was reached in the computational domain. We considered a steady state to have been reached when the accretion rate added to the mass-loss rate in the binary was equal to the rate of mass transfer through L_1. This state is reached after approximately one or two periods after the radiative cooling is switched on. In practice, we continued the computations for 10–12 orbital periods, to ensure we obtained a steady state over a long time.

Figures 1 (V373 Cas), 2 (U Cep), and 3 (RZ Sct) present the results of the computations. Figures 1a, 2a, 3a present density contours and flow lines, and Figs. 1b, 2b, 3b present temperature contours and the velocity field (the density is given in units of 10^{11} cm^{-3}, the temperature in units of 10 000 K, and the velocity field in arbitrary units). These figures indicate that the morphology of the gas flows and the structure of the envelopes basically reproduce the results of [20]. In other words, in these systems, the interaction between the flow and accretor depends on the component-mass ratio (cf. the almost direct collision between the flow and accretor in U Cep and V373 Cas and the tangential impact of the flow on the accretor in RZ Sct). We see that the relation between the density and the size of the envelope and disk in the new computations is also similar to that in [20]—a small accretion disk and large extended envelope in U Cep and V373 Cas, versus a fairly dense (of the order of 10^{14} cm^{-3}) and large disk (filling about 90% of the accretor's Roche lobe) in RZ Sct. As in our previous study, we use the term "disk" to mean that part of the flow that envelopes the accretor and displays a velocity field similar to that of a classical disk; however, unlike a classical disk, it falls down onto or moves away from the star over a single period. The figures also display gas motions from the disk toward the libration points and the reverse motion from them to L_1.

Although the gas motions in the Algol-type close binaries observed in the new simulations essentially coincide with the results obtained in [20], the details of the gas flows differ. The main difference is that the density at the boundary of the computational domain varies more sharply in the new results. In V373 Cas, the minimum density is reached at the libration points L_4 and L_5, where strong shocks are formed (Fig. 1b), providing evidence for outflows of matter from these points. In addition, we can see that the new com-

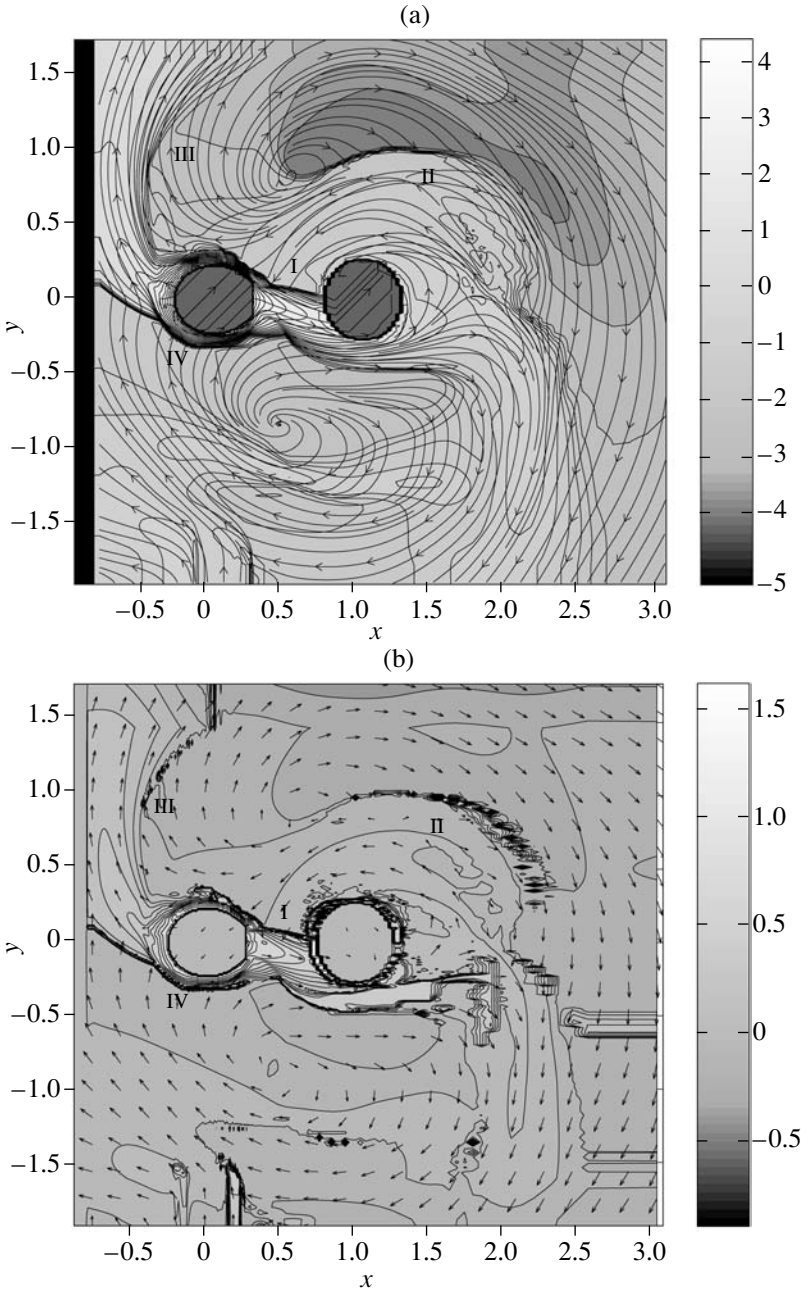

Fig. 1. (a) Density contours and flow lines and (b) temperature contours and the velocity field for V373 Cas.

putations indicate intense flows of gas from the disk toward the libration points.

The results presented in Figs. 1–3 indicate that, as in [20], a set of shocks forms: the shock I (in the notation of Bisikalo *et al.* [14]), due to the interaction between the accretion disk and flow, and the weak shocks III and IV around the donor surface. However, the main difference between the new results and those of [20] is the formation of a powerful shock II in the region of the disk where it interacts with the matter flowing from L_4.

Another result of simultaneously taking into account radiative cooling and the absorption of radiation in the envelope is that the temperature in the disk is 30 000–70 000 K and the temperature in the envelope surrounding the disk is 5000–15 000 K (Figs. 1b, 2b, 3b). Thus, the model for radiative cooling we have used has enabled us to obtain temperatures in gaseous structures in the close binaries that are close to those observed.

To illustrate the temperature and density distributions in the envelopes and disks of the three close bi-

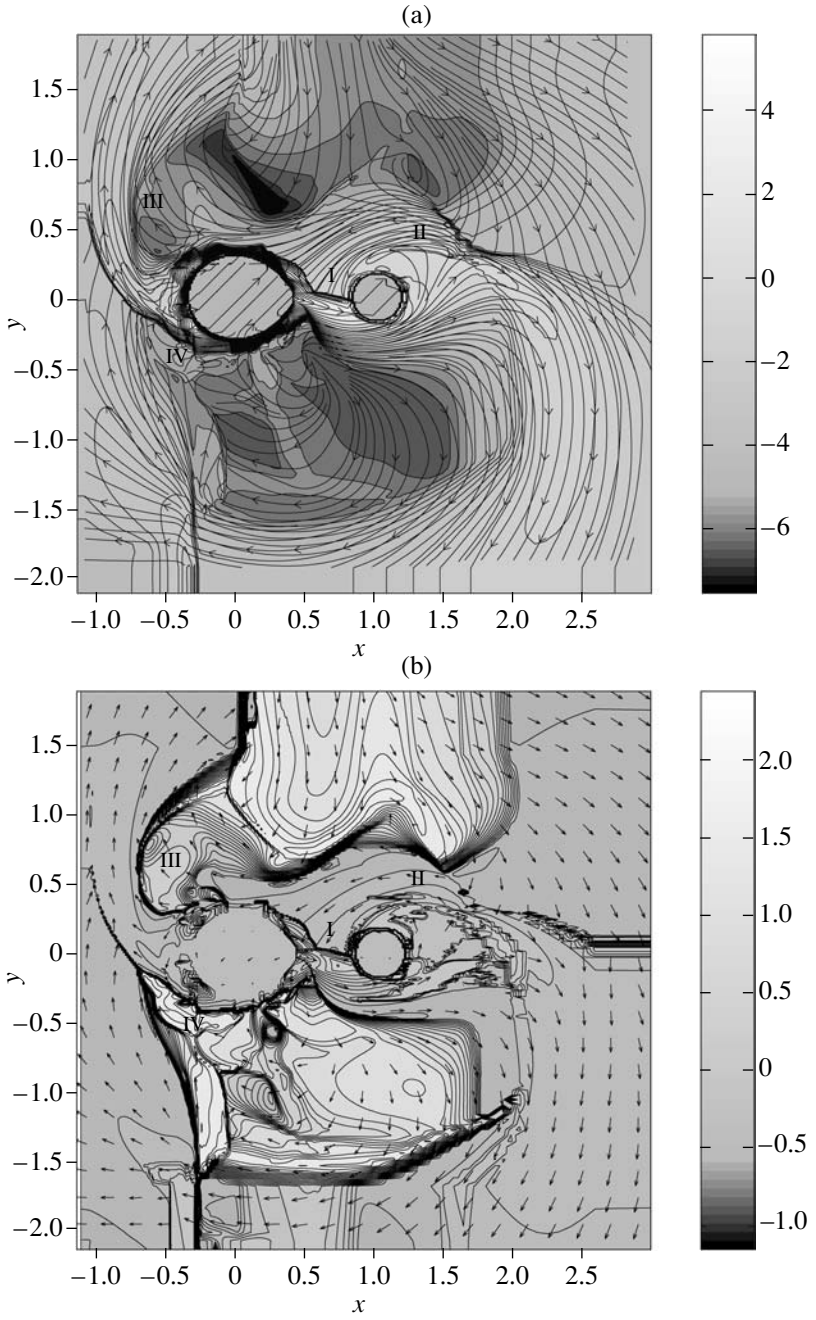

Fig. 2. Same as Fig. 1 for U Cep.

naries, we plotted these parameters as functions of the radial distance from the center of the accretor along a line perpendicular to the line connecting the centers (Fig. 4). We can see from Fig. 4 that the density in the disk is $10^{10}-10^{11}$ cm^{-3}, and decreases very rapidly near the outer boundary of the computational domain. The temperatures in the disks and inner parts of the circumstellar envelopes are 15 000–70 000 K, while the temperatures in the outer parts of the envelopes are 4000–7000 K. The spiral shock II is manifest by increases in the density and temperature. Thus, the obtained temperature distributions indicate that viscosity (in our case, numerical) plays the main role in heating the gas in the disk, while radiative cooling does the same for temperature variations in the outer envelope surrounding the disk.

3.2. Results of the Three-dimensional Hydrodynamical Simulations

Our three-dimensional computations of mass transfer in these three close binaries were carried

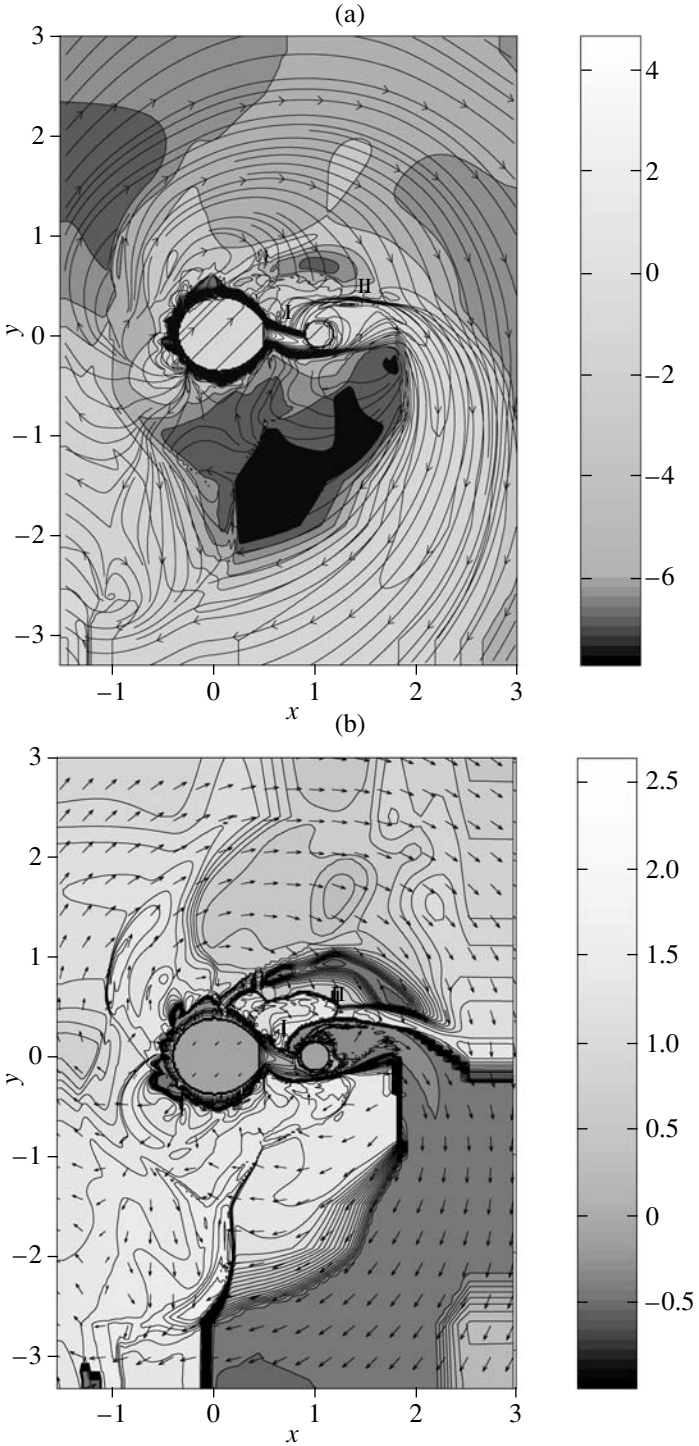

Fig. 3. Same as Fig. 1 for RZ Sct.

out for the same mass-transfer rates through L_1 as for the two-dimensional computations. Figures 5 (V373 Cas), 6 (RZ Sct), and 7 (U Cep) present the results. The notation in Figs. 5–7 is as follows: 1 is the flow from L_1, 2 is the accretion disk formed around the accretor, 3 is the accretor, 4 is the shock wave originating adjacent to the boundary of the flow facing orbital phases 0.7–0.8 (this shock is formed when the matter flowing from L_3 moves back toward the donor and interacts with the flow), 5 is the high-temperature region due to the interaction between the flow and the accretor surface, and 6 is the so-called "hot line."

Since the computational domain for the three-dimensional models is restricted to the accretor's

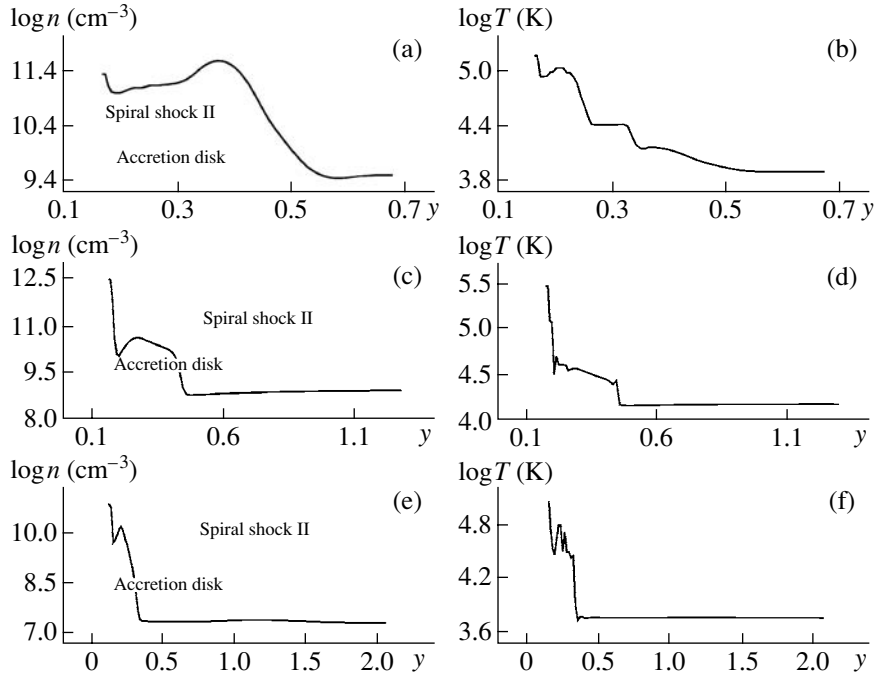

Fig. 4. The density (a, c, e) and temperature (b, d, f) as functions of radial distance in the disk and circumstellar envelope for RZ Sct (a, b), U Cep (c, d), and V373 Cas (e, f).

Roche lobe, we can only carry out limited comparisons between the two- and three-dimensional results. Nevertheless, it is clear that the basic properties of the accretion disks and surrounding envelopes differ. In the two-dimensional computations, relatively weak disks and prominent envelopes are formed in V373 Cas and U Cep. On the contrary, in the three-dimensional computations, the gas around the accretor is primarily concentrated in the accretion disks; this effect is more pronounced in V373 Cas, while the envelope of U Cep remains fairly dense. In RZ Sct, the patterns displayed by the two- and three-dimensional results are similar: the disk is prominent, while the envelope is less dense. The distribution of matter in the $z-x$ and $z-y$ planes in the three-dimensional computations indicates that the height of the disk and circumstellar envelope is equal to the radius of the accretor in all three systems. We can see from Figs. 5–7 that the disk symmetries in the $(z-x)$ and $(z-y)$ planes in the three close binaries are intermediate between those of a torus and cylinder. The three-dimensional model accretion disks are distinguished by the presence of the spiral shock II formed at the outer boundary of the disk in the direction of orbital phases 0.2–0.3 in all three close binaries. This is entirely consistent with the two-dimensional computations, which also show this spiral shock in the disk at the same place in all three close binaries when this model for radiative cooling is used. Note also the shock at the boundary of the flow facing orbital phases 0.6–0.8 in V373 Cas and U Cep (labeled 4 in Fig. 5f). This shock separates matter of the flow and circumstellar envelope in the direction of orbital phases 0.6–0.8. Since the temperature in this shock reaches 100 000 K and the density is lower than 10^{11} cm^{-3}, this structure may well be responsible for the line emission in these close binaries.

Figures 5–7 indicate that the interactions between the flow and accretor are similar in the two- and three-dimensional computations: a nearly head-on collision in U Cep and V373 Cas and a tangential impact in RZ Sct. As a result of the interaction between the flow and accretor, a high-temperature region is formed adjacent to the accretor in RZ Sct and U Cep. No such region is formed in V373 Cas, apparently because the flow velocity in this system is insufficient. This result may be related to the component-mass ratio in V373 Cas, whose donor is more massive than the accretor. The density in the disks of the three close binaries is of the order of 10^{11} cm^{-3}, while the temperatures are 5000–12 000 K. Note also that a high-temperature region is formed at the poles of the accretor (30 000–100 000 K), which may also lead to the radiation of emission lines in the spectra of these close binaries.

4. RESULTS AND CONCLUSIONS

We have carried out new two- and three-dimensional hydrodynamical computations of mass

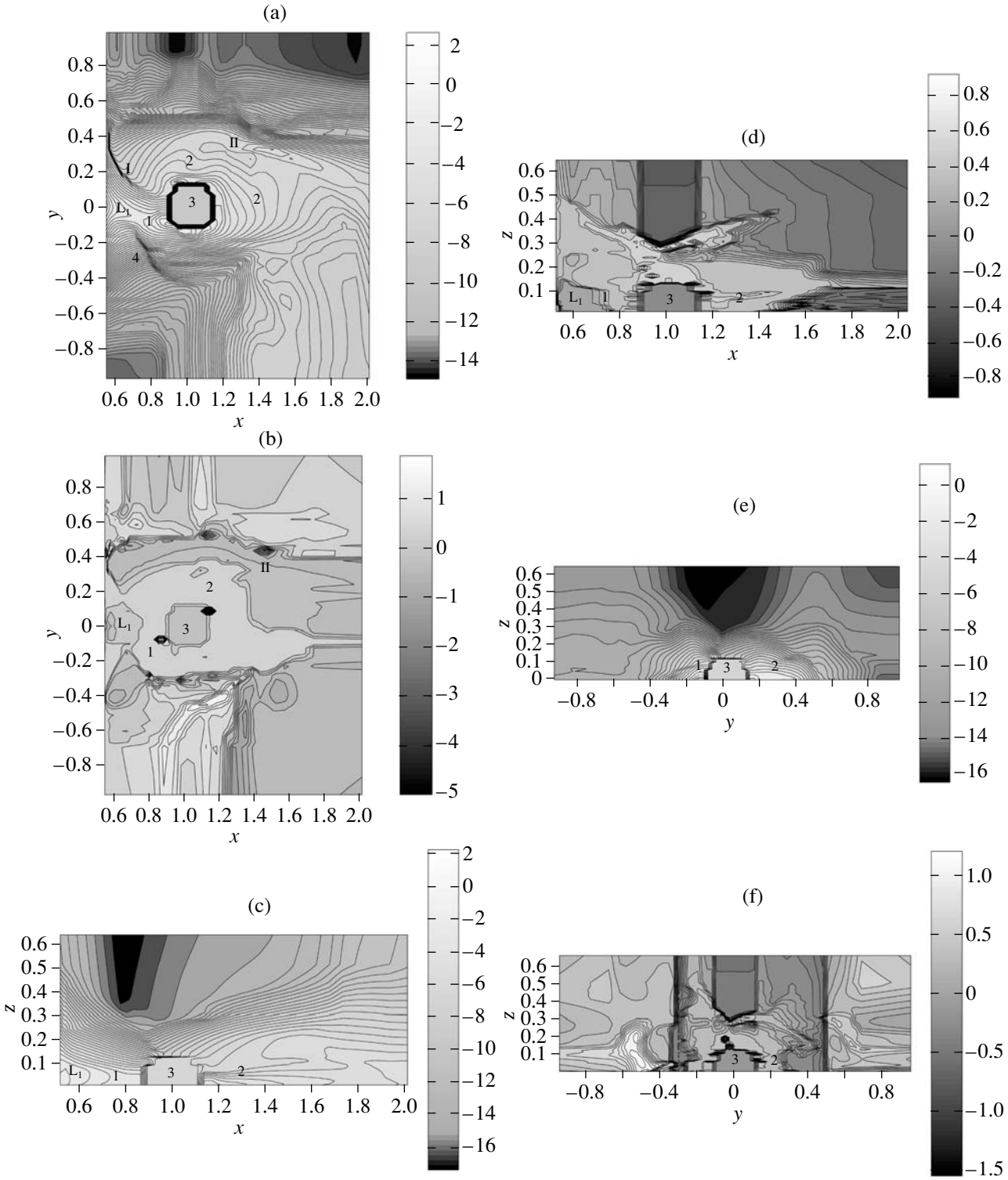

Fig. 5. Density (a, c, e) and temperature (b, d, f) contours in the orbital plane (a, b), the $z-x$ plane (c, d), and the $z-y$ plane containing the accretor (e, f) for V373 Cas.

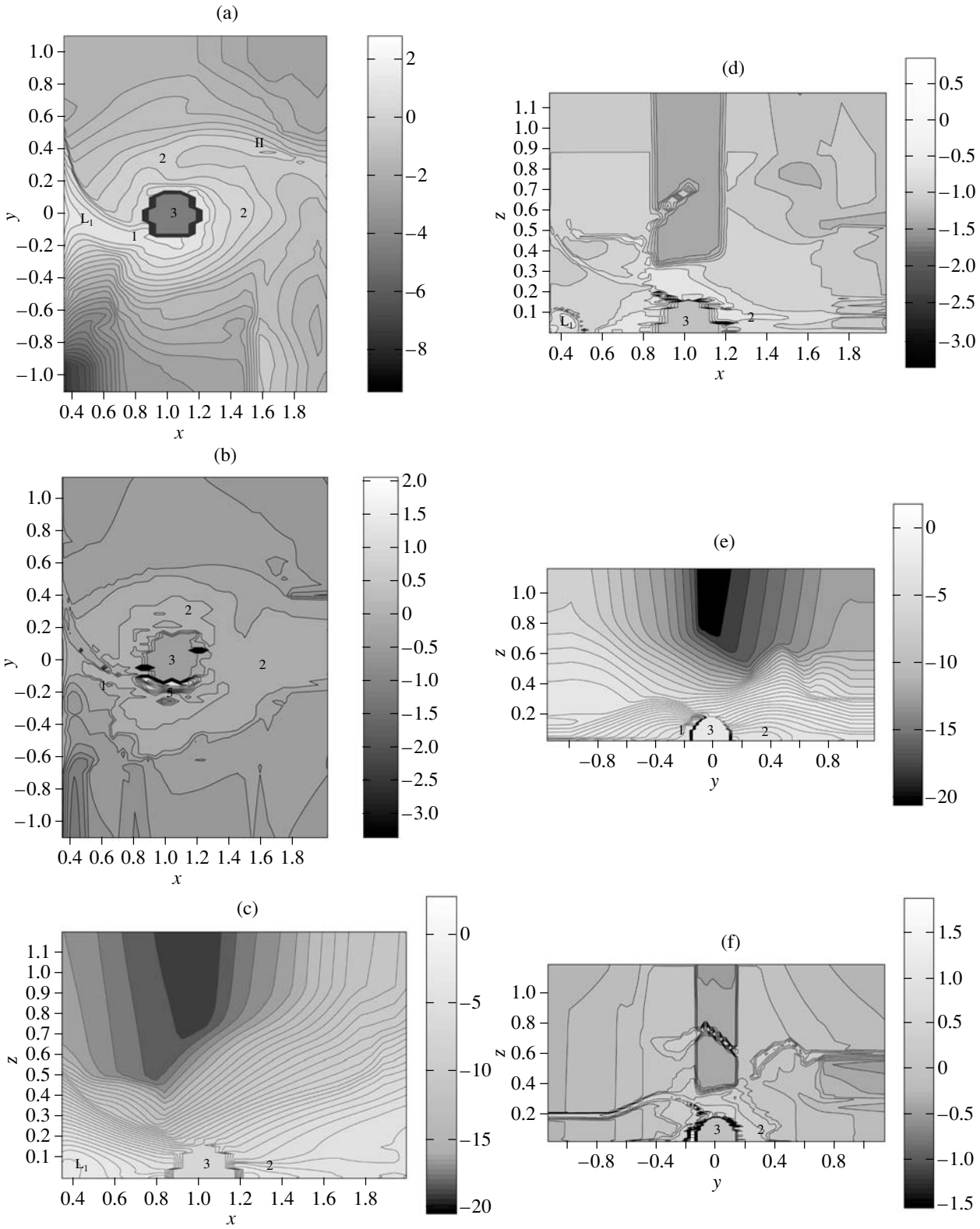

Fig. 6. Same as Fig. 5 for RZ Sct.

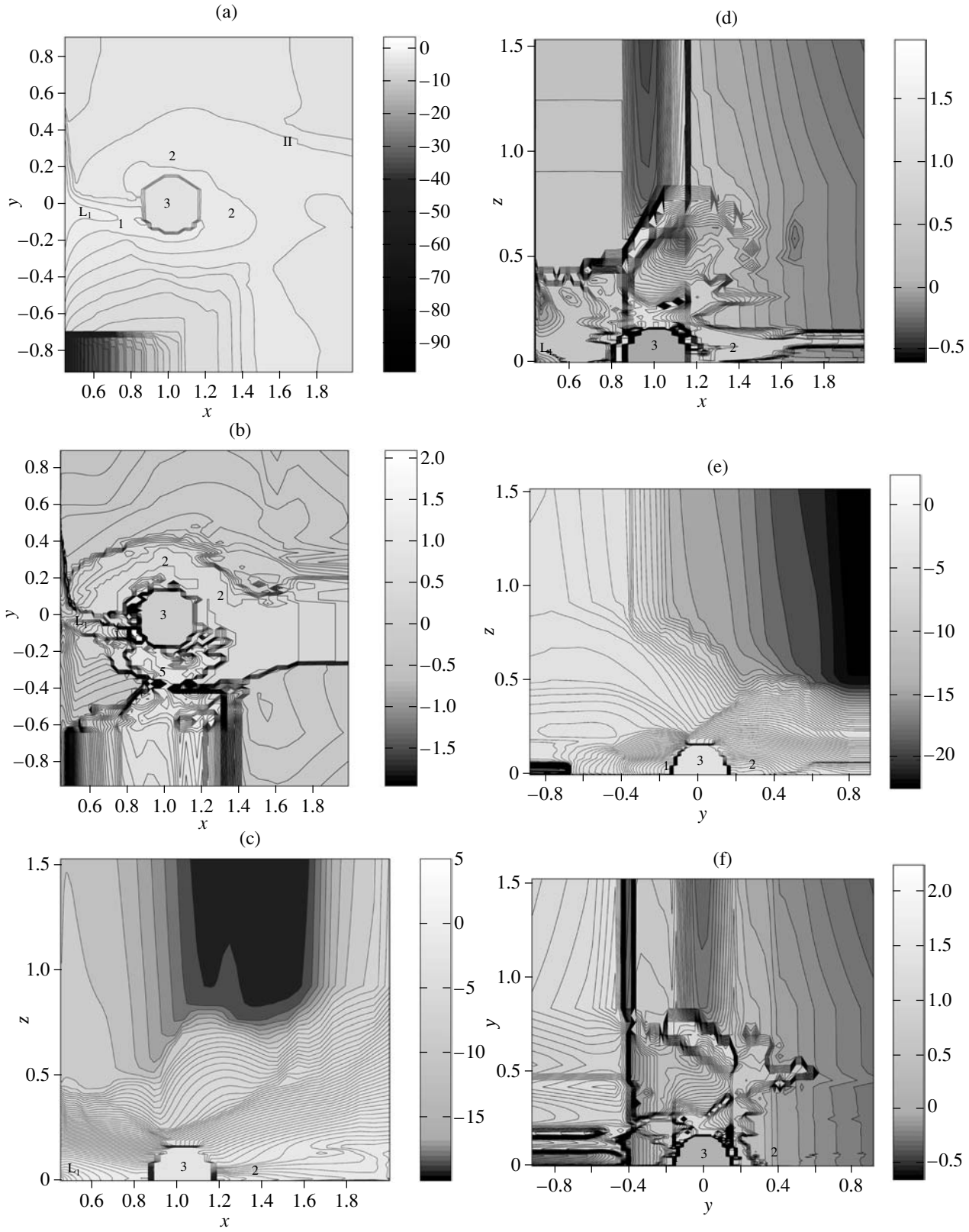

Fig. 7. Same as Fig. 5 for U Cep.

transfer in three Algol-type close binary systems, explicitly taking into account radiative cooling of the moving gas, as well as self-absorption of the radiation in the formed gaseous structures. The computations indicate that the radiative-cooling model we have used enables us to obtain temperatures for the disks and circumstellar envelopes that are consistent with the observed values: 20 000–30 000 K in the disks and 5000–15 000 K in the envelopes. When the two- and three-dimensional computations for the same close binary are compared, it is clear that the circumstellar envelopes are denser in the two-dimensional case, while the disks in some systems are less dense; this is probably due to numerical effects in the two-dimensional computations (the gas is not able to escape from the orbital plane, and hence forms massive gaseous structures there). A common feature of the two- and three-dimensional computations allowing for radiative cooling is that the interactions between the flow and accretor do not depend on the dimension of the computations, and are determined only by the degree of overfilling of the Roche lobe. Another common feature is the formation of a spiral shock in the disk, along which matter from the disk is transferred to the vicinity of the Lagrangian points L_2 and L_3, after which it leaves the binary. Note also the formation of a shock along the boundary of the flow in direct contact with the disk (the hot line) and, in V373 Cas and U Cep, the formation of a shock at the boundary of the flow facing orbital phases 0.6–0.8. Our three-dimensional computations display a high-temperature region in the zone of interaction between the flow and accretor. This region, together with the shocks originating in the disk and at the boundaries of the flow, may well be sources of line emission in the spectra of these three close binaries. According to our three-dimensional computations, the height of the accretion disk and circumstellar envelope in the z direction is approximately equal to the radius of the accretor, which supports our a priori assumption for the two-dimensional computations.

REFERENCES

1. K. Sawada, T. Matsuda, M. Inoue, *et al.*, Mon. Not. R. Astron. Soc. **224**, 307 (1987).
2. M. Różyczka and H. Spruit, *Theory of Accretion Disks* (Kluwer, Dordrecht, 1989), p. 341.
3. H. Spruit, *Theory of Accretion Disks* (Kluwer, Dordrecht, 1989), p. 325.
4. D. Molteni, G. Belvedere, and G. Lanzafame, Mon. Not. R. Astron. Soc. **249**, 748 (1991).
5. M. Hirose, Y. Osaki, and S. Mineshige, Publ. Astron. Soc. Jpn. **43**, 809 (1991).
6. G. Lanzafame, G. Belvedere, and D. Molteni, Mon. Not. R. Astron. Soc. **258**, 152 (1992).
7. G. Lanzafame, G. Belvedere, and D. Molteni, Mon. Not. R. Astron. Soc. **263**, 839 (1993).
8. K. Sawada and T. Matsuda, Mon. Not. R. Astron. Soc. **255**, 17 (1993).
9. Z. Meglicki, D. Wickramasinghe, and V. Bicknell, Mon. Not. R. Astron. Soc. **264**, 691 (1993).
10. R. Whiteburst, Mon. Not. R. Astron. Soc. **266**, 35 (1994).
11. J. Simpson, Astrophys. J. **448**, 822 (1995).
12. P. J. Armitage and M. Livio, Astrophys. J. **470**, 1024 (1996).
13. H. Yukawa, H. M. J. Boffin, and T. Matsuda, Mon. Not. R. Astron. Soc. **292**, 321 (1997).
14. D. V. Bisikalo, A. A. Boyarchuk, V. M. Chechetkin, *et al.*, Mon. Not. R. Astron. Soc. **300**, 39 (1998).
15. D. V. Bisikalo, A. A. Boyarchuk, V. M. Chechetkin, *et al.*, Astron. Zh. **76**, 905 (1999) [Astron. Rep. **43**, 797 (1999)].
16. D. V. Bisikalo, P. Harmanec, A. A. Boyarchuk, *et al.*, Astron. Astrophys. **353**, 1009 (2000).
17. M. T. Richards and G. E. Albricht, Astrophys. J., Suppl. Ser. **123**, 537 (1999).
18. J. M. Blondin, M. T. Richards, and M. L. Malinovski, Astrophys. J. **445**, 939 (1995).
19. D. P. Cox and E. Daltabuilt, Astrophys. J. **167**, 113 (1971).
20. V. V. Nazarenko and L. V. Glazunova, Astron. Zh. **80**, 1114 (2003) [Astron. Rep. **47**, 1027 (2003)].
21. V. V. Nazarenko and L. V. Glazunova, Astron. Zh. **80**, 1099 (2003) [Astron. Rep. **47**, 1013 (2003)].
22. R. L. Kurucz, Astrophys. J., Suppl. Ser. **40**, 1 (1979).
23. O. M. Belotserkovskiĭ and Yu. M. Davydov, *Large Particles in Gas Dynamics* (Nauka, Moscow, 1982) [in Russian].

Translated by K. Maslennikov

Astronomy Reports, Vol. 49, No. 4, 2005, pp. 295–308. Translated from Astronomicheskiĭ Zhurnal, Vol. 82, No. 4, 2005, pp. 331–346.

Evolution of the Masses of Neutron Stars in Binary Systems

A. I. Bogomazov[1], M. K. Abubekerov[2], V. M. Lipunov[1,2], and A. M. Cherepashchuk[1,2]

[1]*Moscow State University, Moscow, Russia*

[2]*Sternberg Astronomical Institute, Moscow State University, Moscow, Russia*

Received August 10, 2004; in final form, September 20, 2004

Abstract—We study the growth of the masses of neutron stars in binary systems due to the accumulation of mass from the optical donors accreted onto the neutron-star surface. Possible scenarios for this accretion are considered. The masses and magnetic-field strengths of radio pulsars derived using population-synthesis methods are compared to the observational data. The population-synthesis analysis indicates that a neutron star can increase its mass from the standard value of $m_x \simeq 1.35M_\odot$ to the Oppenheimer–Volkoff limit, $m_x \simeq 2.5M_\odot$, via accretion from a companion. © *2005 Pleiades Publishing, Inc.*

1. INTRODUCTION

Data from orbiting X-ray observatories have enabled the discovery of about a thousand X-ray sources in the Milky Way and nearby galaxies [1, 2]. Most are close binary systems in which an optical component supplies mass to a neutron star. Accretion onto the surface of a neutron star at subrelativistic velocities results in an enormous release of X-ray energy and luminosities of the order of 10^{36}–10^{37} erg/s [3–7]. The mechanism for this powerful generation of energy was first predicted and demonstrated by Zeldovich [3] and Salpeter [4].

According to our current understanding of such systems, superaccretion and hyperaccretion may occur in addition to ordinary accretion, depending on the parameters of the binary and the mass-loss rate of the optical star. In the case of superaccretion, the X-ray luminosity reaches the Eddington limit, thereby limiting further accretion. This happens at accretion rates of $\dot{m} \simeq 10^{-4}$–$10^{-5}M_\odot$/yr. Chevalier [8] showed that, when the accretion rate is higher ($\dot{m} \simeq 10^{-2}$–$10^{-3}M_\odot$/yr), energy is radiated away not by high-energy photons, but by neutrinos. Over the typical time scale for the hyperaccretion stage of $\sim 10^2$ yr, up to $\sim 1M_\odot$ of matter may be incident onto the surface of the neutron star.

In recent years, masses have been measured for more then ten radio and X-ray pulsars, and the number of mass estimates for neutron stars is continuously growing. We have carried out a population-synthesis analysis using the "Scenario Machine" [9] with the aim of elucidating possible values of the masses and magnetic-field strengths of neutron stars in binary systems.

2. THREE REGIMES OF MASS ACCRETION BY NEUTRON STARS

A considerable fraction of observed neutron stars have increased their masses in the course of their evolution, or are still increasing their masses (e.g., in X-ray sources). But how large can this mass increase be? It is clear that the only origin of a mass increase is accretion. It is evident that the overall change in the mass of a neutron star is determined not only by the accretion rate, but also by the duration of the accretion stage:

$$\Delta M = \int_0^{T_a} \dot{M}(t)dt = \dot{M}T_a, \qquad (1)$$

where $\dot{M}$ is the mean accretion rate and T_a is the lifetime of the accretion stage. We emphasize that, in the case under consideration, the accretion rate is the amount of matter falling onto the surface of the neutron star per unit time, and can differ significantly from the values indicated by the classical Bondi–Hoyle formulas. Three regimes of accretion are possible in a close binary containing a neutron star: ordinary accretion, superaccretion, and hyperaccretion.

Accretion

An ordinary accretion regime is realized when all the matter captured by the gravitational field of the neutron star falls onto its surface. This is possible only if the radiation pressure and electromagnetic forces associated with the magnetic field of the star and its rotation are small compared to the gravitational force.

In this case, the increase in the mass will be precisely determined by the gas dynamics of the accretion at the gravitational-capture radius or, if the donor

1063-7729/05/4904-0295$26.00

Table 1. Masses and rotational periods of neutron stars in radio pulsar + neutron star systems

System	p_{spin}, ms	$\dot{p}_{spin}$, s/s	B, G	$m_{\rm PSR}, M_\odot$	References
J1518+4904	40.9	4.0×10^{-20}	2.6×10^9	$1.56^{+0.20}_{-1.20}$	[13, 14]
B1534+12	37.9	2.4×10^{-18}	1.9×10^{10}	1.3332 ± 0.0020	[13, 15, 16]
B1913+16	59.0	8.6×10^{-18}	4.6×10^{10}	1.4408 ± 0.0006	[13, 17, 18]
B2127+11C	30.5	1.0×10^{-17}	3.5×10^{10}	1.349 ± 0.080	[13, 19]
J0737−3039(1)	22.7	1.7×10^{-18}	1.3×10^{10}	1.337 ± 0.010	[20]
J0737−3039(2)	2773.5	8.8×10^{-16}	3.2×10^{12}	1.250 ± 0.010	[20]

fills its Roche lobe, by the component-mass ratio and the evolutionary status of the optical component. In this case, the accretor is observed as an X-ray source with luminosity

$$L_x = \dot{M}\frac{GM_x}{R_*}, \tag{2}$$

where M_x and R_* are the mass and radius of the neutron star. The accretion rate $\dot{M}$ is determined by the Bondi–Hoyle formula

$$\dot{M} = \pi R_G^2 \rho v, \tag{3}$$

where R_G is the gravitational-capture radius of the neutron star, v is the velocity of the gas flow relative to the neutron star, and ρ is the density of the gas.

The X-ray luminosity of the accretor L_x and its other main parameters can be used to estimate the mass ΔM accumulated during the accretion phase:

$$\Delta M = \frac{L_x R_* T_a}{GM_x}. \tag{4}$$

For massive stars, with lifetimes of less than 10^7 yr, accretion via the stellar wind of the donor is negligibly small at the level of accuracy provided by modern computations. However, the mass increase for low-mass systems containing one or more components that fill their Roche lobes can be considerable, reaching several solar masses. We shall show this below.

Superaccretion

The most thorough analysis of the superaccretion regime for a magnetized neutron star was carried out by Lipunov [10]. Despite the absence of detailed models for supercritical disk accretion (supercritical accretion is realized precisely via an accretion disk), it is possible to estimate the main characteristics of the process—the accretion rate, magnetosphere radius, and evolution equations. Accretion is considered to be supercritical when the energy released at the radius where the accretion flow stops exceeds the Eddington limit:

$$\dot{M}\frac{GM_x}{R_{stop}} > L_{Edd} = 1.38 \times 10^{38}(M_x/M_\odot)\text{erg/s},$$

$$\dot{M} > \dot{M}_{crit} = 10^{-8} M_\odot/\text{yr},$$

where R_{stop} is either the radius of the neutron star or the magnetosphere radius R_A.

For strongly magnetized neutron stars with magnetic fields $B \gg 10^8$ G, all matter arriving from the magnetosphere is accreted onto the magnetic poles, where the corresponding gravitational energy is released. If the blackbody temperature T, roughly estimated as

$$S\sigma T^4 = \dot{M}\frac{GM_x}{R_*}, \tag{5}$$

is higher than 5×10^9 K (S is the area of the base of the accretion column), most of the energy will escape the surface from the neutron star in the form of neutrinos, and, hence, will not hinder accretion [11, 12]. In this case, the rate at which the neutron star accumulates mass will be

$$\dot{M} \simeq \dot{M}_{crit}\left(\frac{R_A}{R_*}\right)^2 \gg \dot{M}_{crit}.$$

If the temperature becomes lower, there will be an upper limit on the accretion rate equal to the standard Eddington limit.

Hyperaccretion

A considerable fraction of neutron stars in binary systems pass through a common-envelope stage in the course of their evolution. In this case, the neutron star is effectively immersed in its optical companion, and for a short time (10^2–10^4 yr) moves along spirals inside a region of dense matter. The formal accretion rate estimated using the Bondi–Hoyle formulas is four to six orders of magnitude higher than the critical rate and, as was suggested by Chevalier [8], this

Table 2. Masses and rotational periods of neutron stars in radio pulsar + white dwarf (optical star) systems

System	p_{spin}, ms	$\dot{p}_{spin}$, s/s	B, G	$m_{\rm PSR}, M_\odot$	References
J0437−4715	5.76	1.0×10^{-20}	4.86×10^8	1.58 ± 0.18	[13, 21]
J0621+1002	28.9	4.70×10^{-20}	2.36×10^9	$1.70^{+0.59}_{-0.63}$	[22, 23]
J1012+5307	5.26	1.20×10^{-20}	5.09×10^8	1.7 ± 1.0	[13]
J1141−6545	394	4.29×10^{-15}	2.63×10^{12}	1.30 ± 0.02	[24, 25]
J1713+0747	4.57	8.52×10^{-21}	4.00×10^8	1.65 ± 0.45	[13, 26, 27]
B1802−07	23.1	4.70×10^{-19}	6.67×10^9	$1.26^{+0.15}_{-0.67}$	[13]
B1855+09	5.36	1.78×10^{-20}	6.26×10^8	$1.57^{+0.25}_{-0.20}$	[13, 27]
B2303+46	1066.4	5.6×10^{-16}	1.57×10^{12}	1.34 ± 0.10	[13, 28]
J1740−5340	3.65	1.6×10^{-19}	1.55×10^9	1.53 ± 0.19	[29–31]

may result in hyperaccretion, when all the energy is carried away by neutrinos for the reasons described above. There are currently no detailed theories for hyperaccretion or the common-envelope stage. The amount of matter accreted by the neutron star can be estimated as

$$\Delta M = \int_0^{T_{hyper}} \frac{1}{4}\left(\frac{R_G}{a}\right)^2 \dot{M} dt \qquad (6)$$

$$\simeq \frac{1}{4}(M_{opt} - M_{core})\left(\frac{M_x}{M_{opt}}\right)^2,$$

where T_{hyper} is the duration of the hyperaccretion stage, R_G is the gravitational-capture radius of the radio pulsar, a is the initial semimajor axis of the close binary orbit, M_{core} is the mass of the core of the optical star, and M_{opt} and M_x are the total masses of the optical star and of the radio pulsar at the onset of the hyperaccretion stage.

Inserting the parameters of observed X-ray systems into (3), (4), and (6), we obtain for the masses of matter accreted in various accretion processes values from $\sim 0.1 M_\odot$ to $\sim 1 M_\odot$.

In recent years, masses have been measured for more than ten neutron stars, on average, with accuracies of $\sim(0.3-0.5)M_\odot$. Thus, the observational data already allow empirical tests of the hypothesis that neutron stars in binary systems can accumulate mass.

3. OBSERVED MASSES AND MAGNETIC FIELDS OF NEUTRON STARS

We consider here binary systems in which the mass-transfer stage is already over—radio pulsars paired with neutron stars and white dwarfs.

The masses of the radio pulsars and other parameters of these systems are listed in Tables 1 and 2 (see also Fig. 2 below). The masses listed in the tables are dynamical estimates derived from radial-velocity curves for point-mass models. Most of the values are taken from the 1999 review of Thorsett and Chakrabarty [13]. The uncertainties in the mass estimates for radio pulsars paired with neutron stars (Table 1) are given for the 68% confidence level. The uncertainties in the mass estimates for radio pulsars paired with white dwarfs (Table 2) are given for the 95% confidence level.

The observed rotation of an accreting neutron star is the result of two competing processes: acceleration due to the transfer of angular momentum from inner regions of the accretion disk, and braking due to the interaction of the toroidal component of the neutron star's magnetic field with outer regions of the accretion disk [10]. An equilibrium between the accelerating and braking torques is established over a time

$$t_{eq} \simeq \frac{I\omega}{\dot{M}\sqrt{GMR_c}} \simeq \frac{M_x}{\dot{M}}\left(\frac{R_x}{R_c}\right)^3 \ll \frac{M_x}{\dot{M}}.$$

The equilibrium rotational period of a neutron star p_{eq} is proportional to its magnetic dipole momentum μ (see, e.g., [10]). Thus, a neutron star that has experienced an accretion stage should display a correlation between its magnetic field and rotation. We accordingly investigated, for the radio pulsars considered here, the dependence between their observed rotational periods p_{spin} and the rates at which their rotations are slowing $\dot{p}_{spin}$ (Fig. 1). The value of $\dot{p}_{spin}$ is proportional to the square of the magnetic dipole momentum of the radio pulsar μ [see (7)]. Figure 1 shows that the radio pulsars considered by us display a clear correlation between $\dot{p}_{spin}$ and p_{spin}, suggesting that the radio pulsars listed in Tables 1 and 2

Table 3. Masses and rotational periods of neutron stars in close X-ray binaries

System	p_{spin}, s	$m_{NS}, M_\odot$	References
2A 1822-371	0.593	0.97 ± 0.24	[33, 34]
Her X-1	1.24	1.50 ± 0.30	[35, 36]
Cen X-3	4.8	$1.22^{+0.15}_{-0.14}$	[37, 39]
LMC X-4	13.5	$1.63^{+0.42}_{-0.47}$	[37, 40, 41]
SMC X-1	0.71	$1.48^{+0.47}_{-0.42}$	[37, 42]
4U 1538-52	528.2	$1.18^{+0.29}_{-0.27}$	[37, 42]
Vela X-1	283	$1.93^{+0.19}_{-0.21}$	[37, 44]

are neutron stars that have experienced an accretion stage.

The magnetic fields of radio pulsars can be derived assuming the neutron star loses angular momentum via the magneto-dipole mechanism. The strength of the magnetic field B is computed as

$$\mu = \left(\frac{3Ic^3 p_{spin}\dot{p}_{spin}}{8\pi}\right)^{1/2}, \qquad (7)$$

$$B = 2\mu/R_*^3, \qquad (8)$$

where p_{spin} is the rotational period of the radio pulsar, $\dot{p}_{spin}$ is the rate of deceleration of the rotation, c is the speed of light, I is the radio pulsar's moment of inertia, which is taken to be 10^{45} g cm^2, μ is its magnetic-dipole moment, and R_* is its radius, which we take to be 10^6 cm.

It is impossible to study accretion without mentioning X-ray pulsars. The magnetic fields B of all known X-ray pulsars derived from both gyroscopic lines in their X-ray spectra [32] and their X-ray luminosities [10] exceed 10^{12} G. The masses of X-ray pulsars are listed in Table 3; the errors are given for the 95% confidence level. However, we did not include X-ray pulsars in our study for two reasons. First, the accretion onto the neutron stars in these systems has just started. Most X-ray pulsars are accreting mass from the stellar wind of the optical companion (the only exception known with certainty is the X-ray pulsar Her X-1, which is accreting matter from a disk). Hence, X-ray pulsars have not had time to considerably increase their masses (by one to several tenths of a solar mass). Second, mass estimates for X-ray pulsars remain fairly inaccurate. For example, the high mass of the neutron star in the Vela X-1 system ($m_x = 1.93 M_\odot$) derived from a best-fit model is not trustworthy, since the model does not adequately describe the observational data (for more details, see [37]). For these reasons, we did not consider X-ray pulsars in this study.

We assumed that the magnetic fields of neutron stars decay exponentially to some minimum value $B_{min} = 8 \times 10^7$ G and do not decay further:

$$B = \begin{cases} B_0 \exp(-t/t_d), & t < t_d \ln(B_0/B_{min}), \\ 8 \times 10^7, & t \geq t_d \ln(B_0/B_{min}). \end{cases} \qquad (9)$$

The parameters B_0 and t_d in (9) are the initial field strength and the time scale for decay of the field. It is not possible to determine the exact ages of neutron stars since B_0 and t_d are not known. However, the magnetic-field strength itself can serve as an indicator of age. For this reason, we constructed the dependence between the magnetic-field strength and the neutron-star mass, shown in Figs. 2 and 3. We will call this dependence the magnetic field–mass diagram.

Figure 2 shows the observational estimates of the masses of radio pulsars together with their uncertainties. The errors are fairly large, and mask the scatter of the central values of observed masses. For this reason, we have plotted the central values only in Fig. 3.

The central values of the radio-pulsar masses show certain systematic variations (Fig. 3). We can distinguish two possible branches in the magnetic field—mass diagram: one showing evolution of neutron stars without increasing mass (the vertical gray strip in Fig. 3), and the other showing evolution with increasing mass (slanted gray strip in Fig. 3).

These observational data (despite their large errors) require interpretation. For this purpose, we carried out a population-synthesis analysis using the

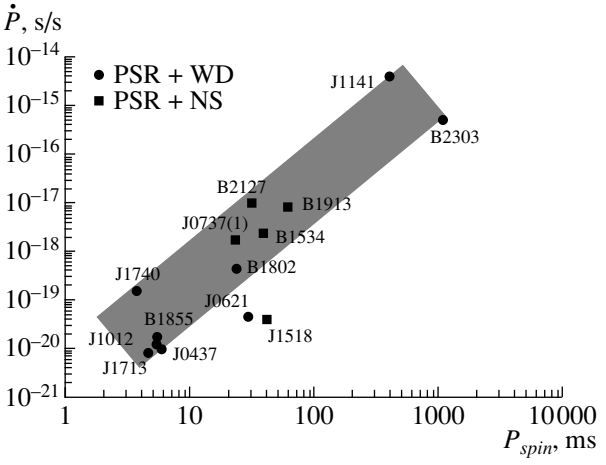

Fig. 1. Dependence between deceleration of the rotation $\dot{p}_{spin}$ and the rotational period p_{spin} for radio pulsars in pairs with white dwarfs (filled circles) and with neutron stars (filled squares).

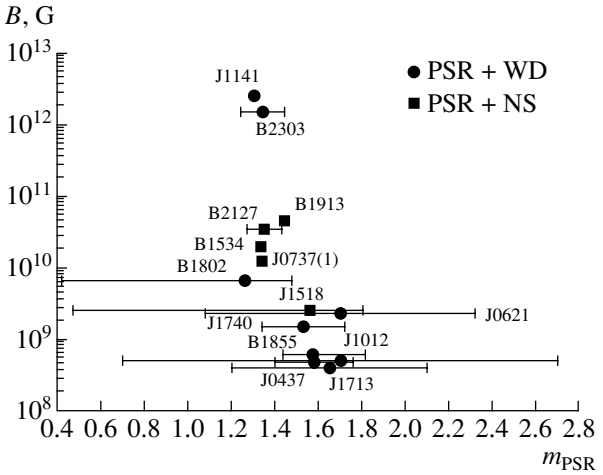

Fig. 2. Relation between the masses m_{PSR} and magnetic-field strengths B of radio pulsars (errors in m_{PSR} are shown). The filled squares and circles correspond to radio pulsars in pairs with neutron stars (PSR + NS) and white dwarfs (PSR + WD).

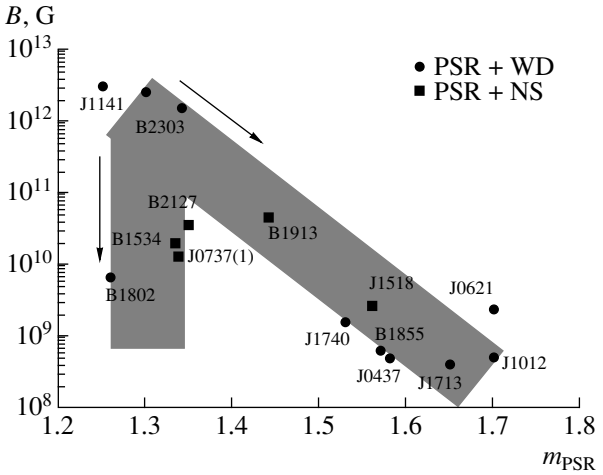

Fig. 3. Relation between m_{PSR} and B for radio pulsars (the errors for m are not shown) with neutron-star (PSR + NS; filled squares) and white-dwarf (PSR + WD; filled circles) companions. The arrows show the directions of the evolution of the mass and magnetic-field strength of the radio pulsars.

"Scenario Machine" [9]. This enabled us to investigate the range of possible observed parameters of the neutron stars, and also to determine qualitatively the types of evolutionary tracks that result in increases in the mass of a neutron star.

4. POPULATION SYNTHESIS

We used the "Scenario Machine" to carry out population syntheses for 19.5 million binary systems [9]. The initial component masses M_1 and M_2 were varied between $5M_\odot$ and $120M_\odot$, assuming a flat distribution of initial component-mass ratios. The initial semimajor axis of the orbit could have any value in the range $(10{-}10^6)R_\odot$.

Based on the population-synthesis output, we identified systems that resulted in the formation of radio pulsar + neutron star (PSR + NS) and radio pulsar + white dwarf (PSR + WD) pairs. We focused on radio pulsars in systems with degenerate dwarfs for our study.

Among the many parameters of binaries with radio pulsars (PSR + NS and PSR + WD), we were interested in the magnetic-field strengths B and masses m_{PSR} of the radio pulsars. Most radio pulsars in pairs with degenerate companions inevitably passed through an accretion phase, thereby increasing their masses by some amount ΔM (see Eq. (1)). The masses and magnetic-field strengths for the PSR + NS systems are presented for the time when the neutron star formed, while the masses and magnetic-field strengths for the PSR + WD systems are presented for the time of formation of the white dwarf. In other words, the magnetic fields and masses correspond to the "birth points" (on the evolutionary tracks) of the PSR + NS and PSR + WD binaries.

The evolution of radio pulsar + optical star systems depends strongly on the magnetic-field strength B and its decay time t_d. Since this decay time is not known, we carried out population-synthesis computations for several magnetic-field decay times: $t_d = 10^7$, 5×10^7, and 10^8 yr. The modeling was carried out for regimes both with and without hyperaccretion. It was assumed that all neutron stars have initial masses $1.35M_\odot$ and initial magnetic fields 2×10^{12} G. Recall that we assumed that the decay of the neutron-star magnetic field was exponential, $B = B_0 \exp(-t/t_d)$ [see (9)].

The population-synthesis algorithm also assumed that the anisotropic kick velocities acquired by the neutron stars during the supernova explosions in which they are formed have a Maxwellian-like distribution with dispersion $v_0 = 180$ km/s [44], and that the spatial distribution of the kick velocities is isotropic. The Chandrasekhar mass was set equal to $m_{Ch} = 1.4M_\odot$. The Oppenheimer–Volkoff limit was taken to be $m_{OV} = 2.5M_\odot$.

Figures 4–8 show the magnetic fields of the radio pulsars and their masses at the birth epochs of the PSR + NS and PSR + WD pairs derived from the population synthesis. Let us now consider in detail each possible scenario for the evolution of the masses and magnetic fields of the radio pulsars in these systems.

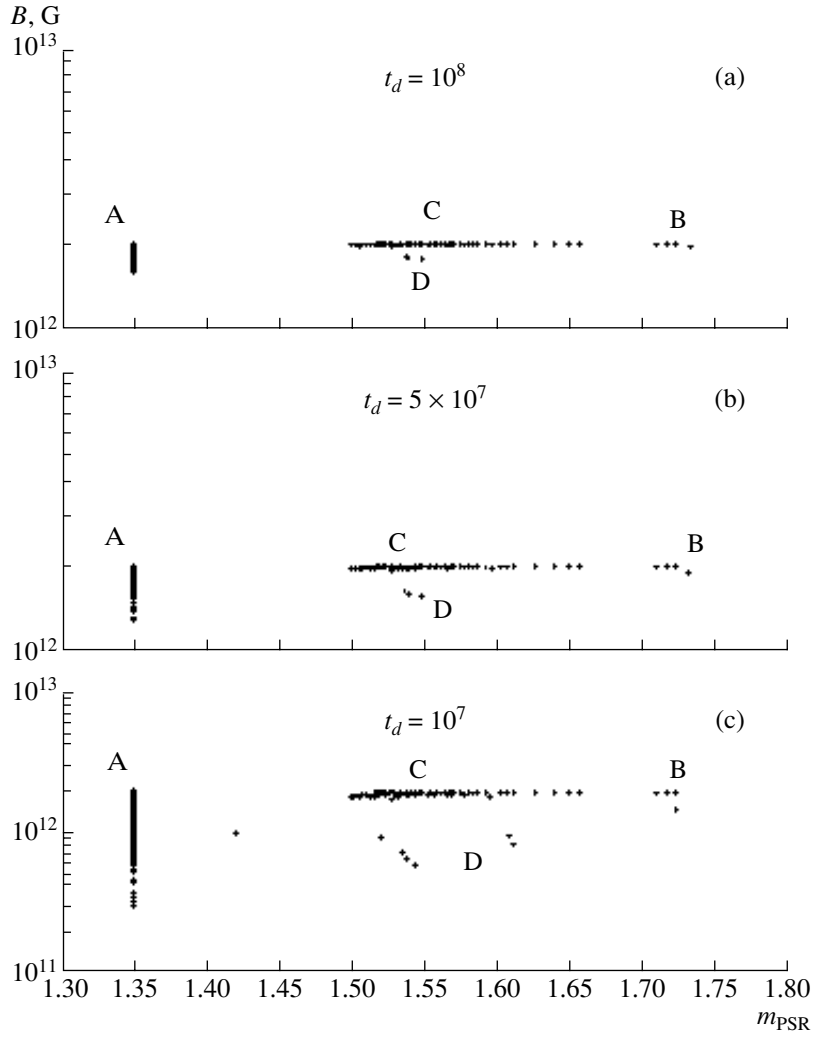

Fig. 4. Masses and magnetic-field strengths for radio pulsars in the $\sim 7 \times 10^4$ PSR + NS binaries generated in the population synthesis for 19.5 million initial systems, taking hyperaccretion into account. A detailed description of selected groups of pulsars is given in the text.

Radio Pulsars in PSR + NS Binaries (Population Synthesis with Hyperaccretion)

The population synthesis for the 19.5 million initial systems resulted in the formation of $\sim 7 \times 10^4$ PSR + NS systems. PSR + NS systems are produced by the evolution of binaries with initial component-mass ratios $q = M_1/M_2 = 1-4$, initial component masses $M_1 \geq 10M_\odot$, $M_2 \geq 10M_\odot$, and initial semimajor orbital axes $a \simeq (10-10^3)R_\odot$.

Figure 4 shows the magnetic fields and masses of radio pulsars in binaries with neutron stars at the epoch when the PSR + NS system was born. Figures 4a–4c present the population-synthesis results for magnetic-field decay time scales of $t_d = 10^8$, 5×10^7, and 10^7 yr, respectively. Four groups of radio pulsars can be distinguished in all the plots. The four groups of qualitatively similar (in terms of their accretion) groups of pulsars are for convenience labeled A, B, C, and D.

The radio pulsars of group A (Figs. 4a–4c) do not experience accretion, superaccretion, or hyperaccretion, so that their masses do not change: $m_{\rm PSR} = 1.35M_\odot$. However, their magnetic-field strengths decrease. These radio pulsars A are formed from binaries with initial component masses $M_1 \simeq 14-40M_\odot$, $M_2 \simeq 11-15M_\odot$, and initial semimajor orbital axes $a \simeq 10^2-10^3R_\odot$.

The radio pulsars of group B form during the evolution of binaries with $M_1 \simeq 15-22M_\odot$, $M_2 \simeq 14-19M_\odot$, and $a \simeq 10-10^3R_\odot$. These radio pulsars accumulate mass during superaccretion ($\Delta M \simeq 0.1-0.2M_\odot$) and hyperaccretion ($\Delta M \simeq 0.2-0.3M_\odot$) stages. We can see that the mass is accumulated relatively rapidly ($t < t_d$), and the

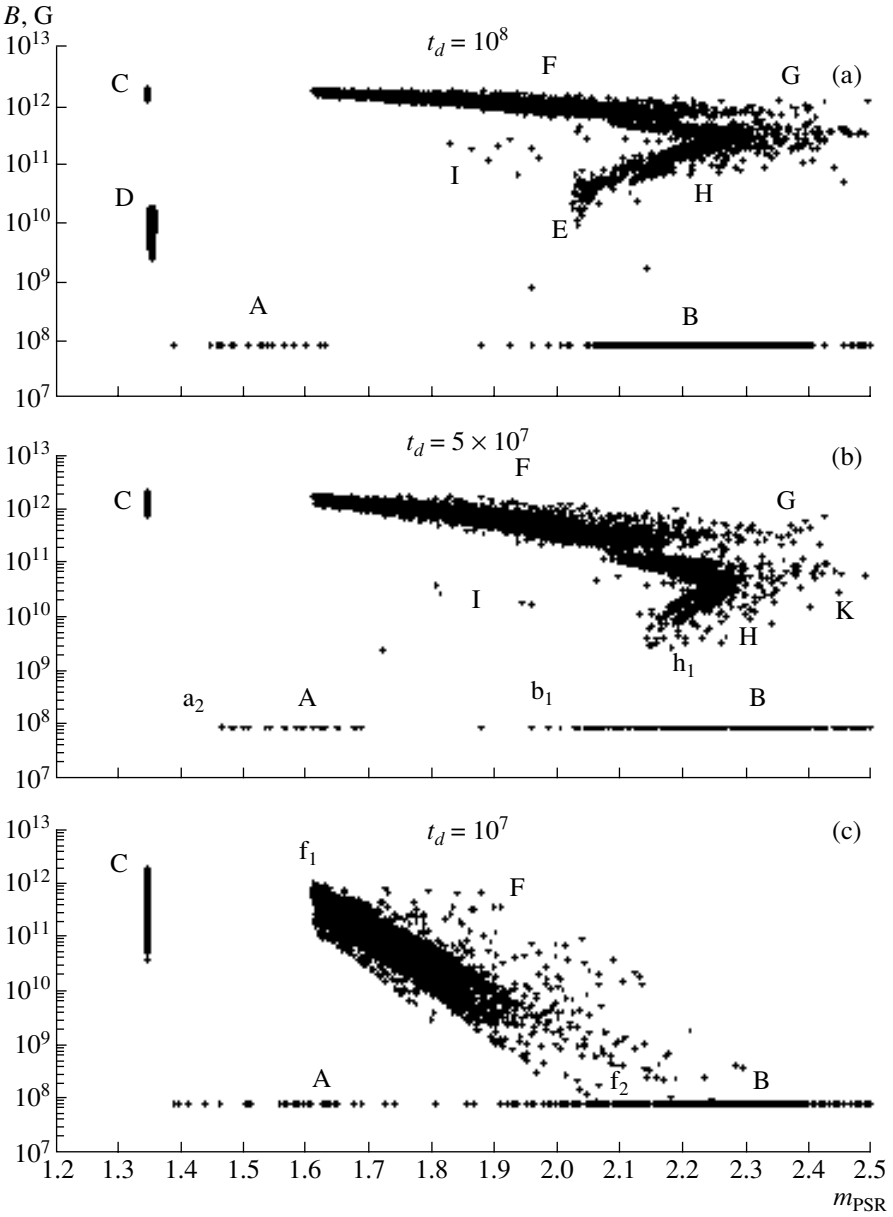

Fig. 5. Same as Fig. 4 for PSR + WD systems ($\sim 16 \times 10^4$ objects).

magnetic-field strength does not have time to change significantly ($B \simeq 2 \times 10^{12}$ G).

The radio pulsars of group C are produced by binary systems whose components have comparable masses ($q \simeq 1$), with the individual component masses being $M_1 \simeq 30{-}40M_\odot$, $M_2 \simeq 30{-}35M_\odot$. The initial semimajor orbital axes are between $\sim 5 \times 10R_\odot$ and $\sim 5 \times 10^2 R_\odot$. These radio pulsars pass through a hyperaccretion stage only, and increase their masses exclusively during this stage ($\Delta M \simeq 0.15{-}0.20M_\odot$). The magnetic-field strength does not have time to change significantly ($B \simeq 2 \times 10^{12}$ G); i.e., the mass is accumulated on a time scale $t < t_d$.

Like the group-B pulsars, the radio pulsars of group D experience both superaccretion and hyperaccretion. However, in contrast to the group-B pulsars, they accumulate only a small amount of matter in the superaccretion stage. For instance, the pulsar masses increase by no more than $0.03M_\odot$ in the superaccretion stage, while $\Delta M \simeq 0.3M_\odot$ in the hyperaccretion stage. The initial component masses for this group are $M_1 = 13{-}52M_\odot$, $M_2 = 10{-}20M_\odot$, and the initial semimajor orbital axes are $a \simeq (2{-}9) \times 10^2 R_\odot$.

The locations of pulsars in groups A, B, C, and D in Figs. 4a–4c are similar. The groups differ only in their magnetic-field strengths, due to the effect of different field-decay time scales. For example, in

Fig. 4c, which plots objects with the shortest decay times ($t_d = 10^7$ yr), the radio pulsars are located lower than their analogs in Figs. 4a and 4c. These differences in t_d do not lead to qualitative differences in the evolutionary scenarios for the formation of PSR + NS systems.

The population-synthesis results show that a radio pulsar can increase its mass from $M \simeq 1.35M_\odot$ to $M \simeq 1.70M_\odot$ during the superaccretion and hyperaccretion stages, over a time $t \leq t_d$.

Radio Pulsars in PSR + WD Binaries (Population Synthesis with Hyperaccretion)

The population synthesis for 19.5 million initial binaries resulted in the formation of $\sim 16 \times 10^4$ PSR + WD binaries. Figure 5 shows the masses and magnetic fields of these pairs at the epoch when the pair is born; i.e., when the white dwarf is formed. As in the previous case, we carried out population syntheses for magnetic-field decay times $t_d = 10^8$, 5×10^7, and 10^7 yr (Figs. 5a–5c).

In contrast to the previous case, variation of the magnetic-field decay time scale t_d led to both quantitative and qualitative differences. As t_d is decreased, the number of radio pulsars with low magnetic fields grows. This shows up as a change in the slope of the strip formed by the radio pulsars in Fig. 5. Decreasing t_d also results in an increase in the number of radio pulsars with the minimum possible magnetic field (Figs. 5a and 5c). The presence of quantitative differences is manifest in the absence of unique connections between the groups of pulsars in Figs. 5a–5c. This provides evidence that the scenario for variations of the radio-pulsar mass realized in a PSR + WD pair depends on the magnetic-field decay time scale. Note that qualitative changes in the mass-accumulation scenario with variation of t_d did not occur for the radio pulsars in PSR + NS systems: the groups of radio pulsars in Figs. 4a–4c are similar.

Let us discuss in detail all the groups of pulsars in Figs. 5a–5c and the evolutionary tracks resulting in their formation.

Magnetic-field Decay Time Scale 10^8 *yr*

Radio pulsars of groups A and B (Fig. 5a) are produced during the evolution of close binaries with initial component masses $M_1 \geq 10M_\odot$ and $M_2 \simeq 1.1$–$1.5M_\odot$ (group A) or $M_2 \simeq 1.5$–$2.5M_\odot$ (group B); the initial semimajor orbital axes are $a = (6$–$7) \times 10^2 R_\odot$. These pulsars accumulate mass only in an accretion stage. Matter flows toward the pulsars from their low-mass donors through the inner Lagrangian point. The pulsar magnetic field has already decayed to its minimum value by the onset of accretion (the low-mass optical companion fills its Roche lobe on the nuclear time scale, $t \sim 10^8$–10^9 yr), and so does not impede the infall of matter onto the surface of the radio pulsar. The pulsars of groups A and B are able to increase their masses by $\Delta M \simeq 0.02$–$1.2M_\odot$ via accretion (Fig. 5a).

Radio pulsars of group C (Fig. 5a) are produced by binaries with $M_1 \simeq 11$–$15M_\odot$, $M_2 \simeq 5.5$–$9.5M_\odot$ and $a = 2 \times 10^2$–$10^3 R_\odot$. Since the two component masses are comparable ($q \simeq 1.5$–2) and large, the pulsar magnetic field has not decayed by the time when the white dwarf forms. These pulsars do not pass through accretion, superaccretion, or hyperaccretion stages. The strong pulsar magnetic field, $B \simeq 10^{12}$ G, prevents the infall of matter from the donor, with the result that the mass of the radio pulsar remains constant: $m_{\rm PSR} = 1.35M_\odot$ (Fig. 5a).

Radio pulsars of group D (Fig. 5a) are produced by binaries with $M_1 \simeq 11$–$16M_\odot$, $M_2 \simeq 1.5$–$4M_\odot$, $q = 4$–6, and $a = 10^3$–$2 \times 10^3 R_\odot$. The time scale for the nuclear evolution of the primary is two orders of magnitude (a factor of $\sim 10^2$) shorter than the nuclear time scale of the secondary. Therefore, the magnetic field of the radio pulsar has already decayed to $\sim 10^{10}$ G by the onset of the accretion stage. The system goes through accretion and superaccretion stages, but, because the field of the neutron star is still strong ($\sim 10^{10}$ G), only a few hundredths of a solar mass fall onto the surface of the neutron star ($\Delta M \sim 0.01$–$0.02M_\odot$).

Radio pulsars of group F (Fig. 5a) are produced by binaries with $M_1 \simeq 10$–$30M_\odot$, $M_2 \simeq 5$–$8M_\odot$, and $a = (1$–$3) \times 10^2 R_\odot$. The masses of these pulsars are not increased significantly via superaccretion, $\Delta M \sim 0.01M_\odot$, and accumulate the most mass in a hyperaccretion stage: $\Delta M \simeq 0.3$–$0.7M_\odot$. The ΔM for the hyperaccretion stage increases with decreasing mass of the optical companion. For example, a radio pulsar with a companion with $M_2 \simeq 9M_\odot$ accumulates $\Delta M \simeq 0.3M_\odot$ in the hyperaccretion stage, while a radio pulsar with a companion with $M_2 \simeq 6M_\odot$ accumulates $\Delta M \simeq 0.7M_\odot$ in this stage.

Radio pulsars of group G (Fig. 5a) are produced by binaries with $M_1 \simeq 13$–$15M_\odot$, $M_2 \simeq 5.5$–$6.5M_\odot$, and $a = (5$–$9) \times 10^2 R_\odot$. These pulsars accumulate mass in accretion ($\Delta M \simeq 0.2M_\odot$) and hyperaccretion ($\Delta M \simeq 0.8M_\odot$) stages.

Radio pulsars of group E (Fig. 5a) are produced by binaries with $M_1 \simeq 10$–$15M_\odot$, $M_2 \simeq 2.5$–$4M_\odot$ and semimajor orbital axes from $a = 2 \times 10^2 R_\odot$ to $2 \times 10^3 R_\odot$. These pulsars increase their masses consecutively in an accretion, superaccretion, and second accretion stage. The pulsar accumulates a few

hundredths of a solar mass in the superaccretion stage. The main mass accumulation occurs in the accretion stages: $\Delta M \simeq 0.7M_\odot$. Like the group D pulsars, the strength of the magnetic field at the onset of the first accretion stage is $\sim 10^{10}$ G, but, in contrast to the group D pulsars, the group E radio pulsars have component separations an order of magnitude smaller. This enables them to increase their masses by $\Delta M \simeq 0.7M_\odot$, rather than $\Delta M \simeq 0.01-0.02M_\odot$.

Radio pulsars of group H (Fig. 5a) pass through a hyperaccretion stage only, in which their masses increase by $\Delta M \simeq 0.8M_\odot$. The initial parameters of their binaries are $M_1 \simeq 12-26M_\odot$, $M_2 \simeq 3-4M_\odot$, and $a \simeq (1-6) \times 10^2 R_\odot$.

The last group of radio pulsars (I) are produced by binaries with $M_1 \simeq 10-11M_\odot$, $M_2 \simeq 3-4M_\odot$, and $a \sim 3 \times 10^2 R_\odot$. They increase their masses only slightly in a superaccretion stage: $\Delta M \simeq 0.02M_\odot$. The pulsar masses grow mainly due to ordinary accretion of matter from the donor through the inner Lagrangian point, with $\Delta M \simeq 0.3-0.4M_\odot$.

Magnetic-field Decay Time Scale 5×10^7 *yr*

As was noted above, if the magnetic-field decay time scale t_d changes [see Eq. (9)], the evolution of close binaries giving rise to PSR + WD systems changes both quantitatively and qualitatively. Some groups of radio pulsars visible in Fig. 5a disappear, while new groups appear (Fig. 5b). For groups of pulsars displaying only quantitative changes with changes in t_d, we keep the same notation, while introducing new notation for qualitatively new groups. Let us start with a description of the new groups and the groups that are no longer present.

Groups of radio pulsars D and E in Fig. 5a disappear (Fig. 5b). Thus, the evolutionary scenarios that result in the formation of these groups are not realized when $t_d = 5 \times 10^7$ yr. Instead, four new groups of pulsars appear, which we denote a_1, b_1, h_1, and K.

Radio pulsars of group a_1 are produced by binaries with $M_1 \simeq 13M_\odot$, $M_2 \simeq 2-3M_\odot$, and $a \simeq (1-2) \times 10^3 R_\odot$. These pulsars undergo a superaccretion stage only, during which they accumulate a mass $\Delta M \simeq 0.01-0.2M_\odot$. At the same time, pulsars of the adjacent group A (Fig. 5b) increase their masses only during an accretion stage.

Radio pulsars of group b_1 are produced by binaries with $M_1 \simeq 17M_\odot$, $M_2 \simeq 2-3M_\odot$, and $a \simeq (5-7) \times 10^2 R_\odot$. These pulsars increase their masses purely due to superaccretion ($\Delta M \simeq 0.5-0.7M_\odot$).

Radio pulsars of group h_1 are produced by binaries with $M_1 \simeq 25M_\odot$, $M_2 \simeq 4-5M_\odot$, and $a \simeq 10^3 R_\odot$. These pulsars accumulate mass in superaccretion ($\Delta M \simeq 0.03M_\odot$) and hyperaccretion ($\Delta M \simeq 0.6M_\odot$) stages.

Radio pulsars of group K also undergo superaccretion and hyperaccretion phases, during which their masses increase by $\Delta M \simeq 0.1M_\odot$ and up to $\Delta M \simeq 1M_\odot$, respectively. Such a large mass increase in the hyperaccretion stage is possible thanks to the small initial separation of the components, $a \simeq 10^2 R_\odot$. The initial component masses for this group are close to those for group h_1: $M_1 \simeq 25M_\odot$ and $M_2 \simeq 5M_\odot$.

The radio pulsars of groups A, C, B, I, F, H, and G in Fig. 5b differ from their counterparts in Fig. 5a only in the strength of their magnetic fields, which have changed with t_d in accordance with (9). The accretion stages, their chronology, and the values of $\Delta M \simeq 1M_\odot$ remain the same. We note only that the pulsars of group F in Fig. 5b accumulate $\Delta M \simeq 0.2M_\odot$ in the superaccretion stage, in contrast to the corresponding pulsars in Fig. 5a, which accumulate only $\Delta M \simeq 0.01M_\odot$.

Magnetic-field Decay Time Scale 10^7 *yr*

Let us now compare the groups of radio pulsars in Figs. 5b and 5c. Groups a_1, a_2, h_1, I, H, K, and G have disappeared, while the qualitatively new groups f_1 and f_2 have emerged.

Radio pulsars of group f_1 (Fig. 5c) are produced by binaries with $M_1 \simeq 10M_\odot$, $M_2 \simeq 10M_\odot$, and $a \simeq 10^2 R_\odot$. These pulsars undergo a superaccretion stage only, accumulating a mass $\Delta M \simeq 0.3M_\odot$.

Like the group F pulsars, radio pulsars of group f_2 accumulate mass during superaccretion ($\Delta M \simeq 0.01-0.1M_\odot$) and hyperaccretion ($\Delta M \simeq 0.5-1M_\odot$) stages. However, in contrast to the group F pulsars, the magnetic-field strength decays to its minimum value, due to the fact that the optical donors are less massive ($M_2 \simeq 3M_\odot$) than the donors of the group F pulsars ($M_2 \simeq 5-8M_\odot$). For this reason, the nuclear time scales for the donors in f_2 group are long enough for the pulsar magnetic fields to decay. The initial masses of the primaries of the binaries giving rise to group f_2 radio pulsars are $M_1 \simeq 12-14M_\odot$, while the initial semimajor orbital axes are $a \simeq (4-5) \times 10^2 R_\odot$.

The remaining groups of radio pulsars in Fig. 5c, i.e., A, B, C, and F, are qualitatively the same as the corresponding groups in Figs. 5a and 5b. The only difference between the two analogous groups of radio pulsars is that the magnetic-field strength changes in accordance with (9), with $t_d = 10^7$ yr.

Thus, the model computations taking into account the common-envelope (hyperaccretion) stage indicate that the masses of radio pulsars in binaries with

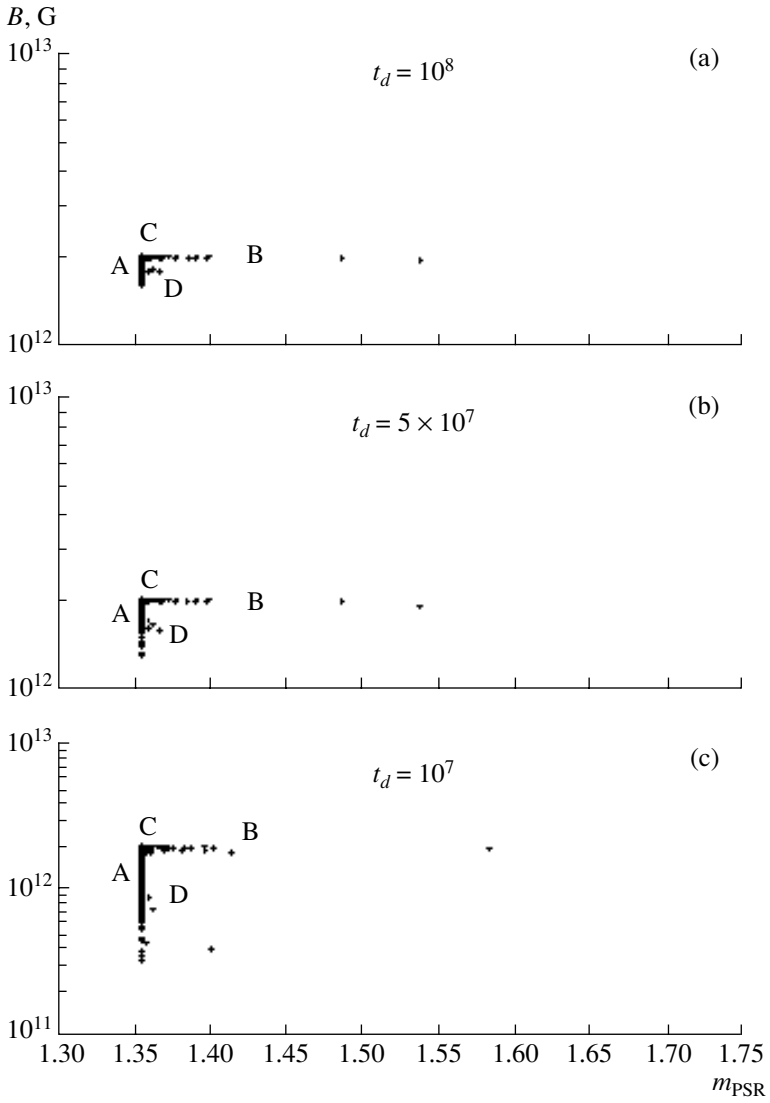

Fig. 6. Same as Fig. 4, but without a hyperaccretion stage.

white dwarfs are in the range $m_{\rm PSR} \simeq 1.35{-}2.5 M_\odot$. Such considerable growths in the masses of radio pulsars can come about due to both hyperaccretion and ordinary accretion from a low-mass optical donor. Note that the radio pulsars can sometimes increase their masses to the Oppenheimer–Volkoff limit, $m_{\rm OV} \simeq 2.5 M_\odot$.

Radio Pulsars in PSR+NS Binaries (Population Synthesis without Hyperaccretion)

The hyperaccretion stage is not well understood. Neither the time scale, nor the rate of infall of matter onto the surface of the neutron star during this stage are known. For this reason, we carried out an additional set of population-synthesis computations without including hyperaccretion; i.e., in which the radio pulsars could increase their masses only via conventional accretion and superaccretion.

As in the previous case, we carried out the population-synthesis computations for 19.5 million initial stellar pairs, with the same ranges of the initial stellar parameters. These computations produced $\sim 7 \times 10^4$ PSR + NS binaries. The masses $m_{\rm PSR}$ and magnetic-field strengths B of the radio pulsars for magnetic-field decay time scales of $t_d = 10^8, 5 \times 10^7$, and 10^7 yr are shown in Figs. 6a–6c, respectively. We can see that the locations of the groups of radio pulsars are similar to those for the other computations. Varying t_d resulted in quantitative changes

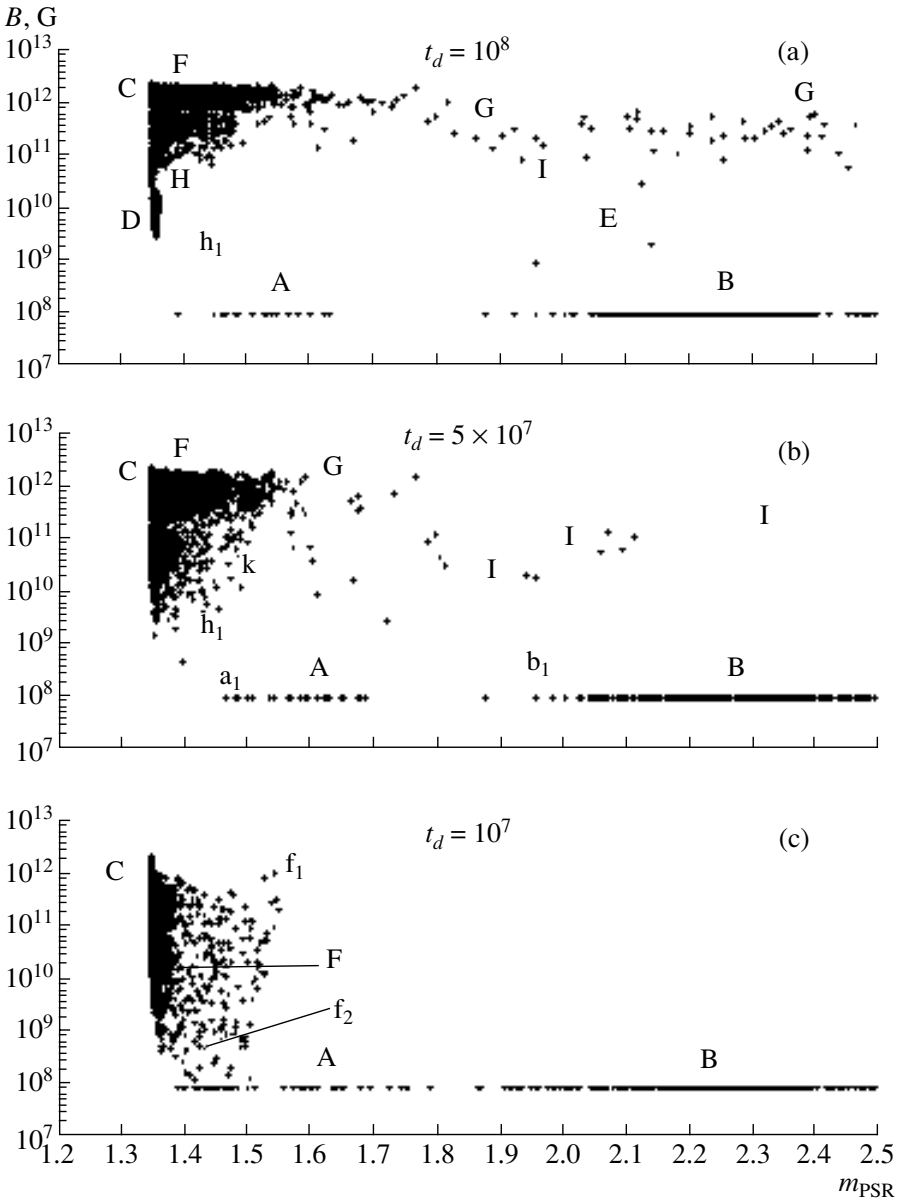

Fig. 7. Same as Fig. 4 for PSR + WD systems ($\sim 16 \times 10^4$ objects) for the computations without hyperaccretion.

only, namely, in a reduction of the magnetic-field strength with decreasing t_d.

Let us see how the population-synthesis computations without a common-envelope stage (Fig. 6) affected the locations of groups A, B, C, and D (Fig. 4). A comparison of Figs. 4 and 6 shows that the masses of the radio pulsars in groups B, C, and D have decreased by $\Delta M \simeq 0.5 M_\odot$: the positions of these pulsars are shifted along the horizontal axis toward lower masses. The positions of the group-A radio pulsars did not change, since these pulsars do not experience accretion, superaccretion, and hyperaccretion stages during their evolution. The initial parameters of the binaries giving rise to the pulsars in groups A, B, C, and D in Fig. 6 are identical to the corresponding parameters for these groups of pulsars in Fig. 4, listed above.

The radio pulsars of groups B, C, and D increase their masses only in a superaccretion stage. Figure 6 shows that the mass accumulated in this stage can range from $\Delta M \simeq 0.01$ to $\Delta M \simeq 0.20 M_\odot$. The accumulation of matter occurs over $t \lesssim t_d$.

Radio Pulsars in PSR + WD Binaries (Population Synthesis without a Common-envelope Stage)

The population-synthesis computations for the 19.5 million initial binaries carried out without a

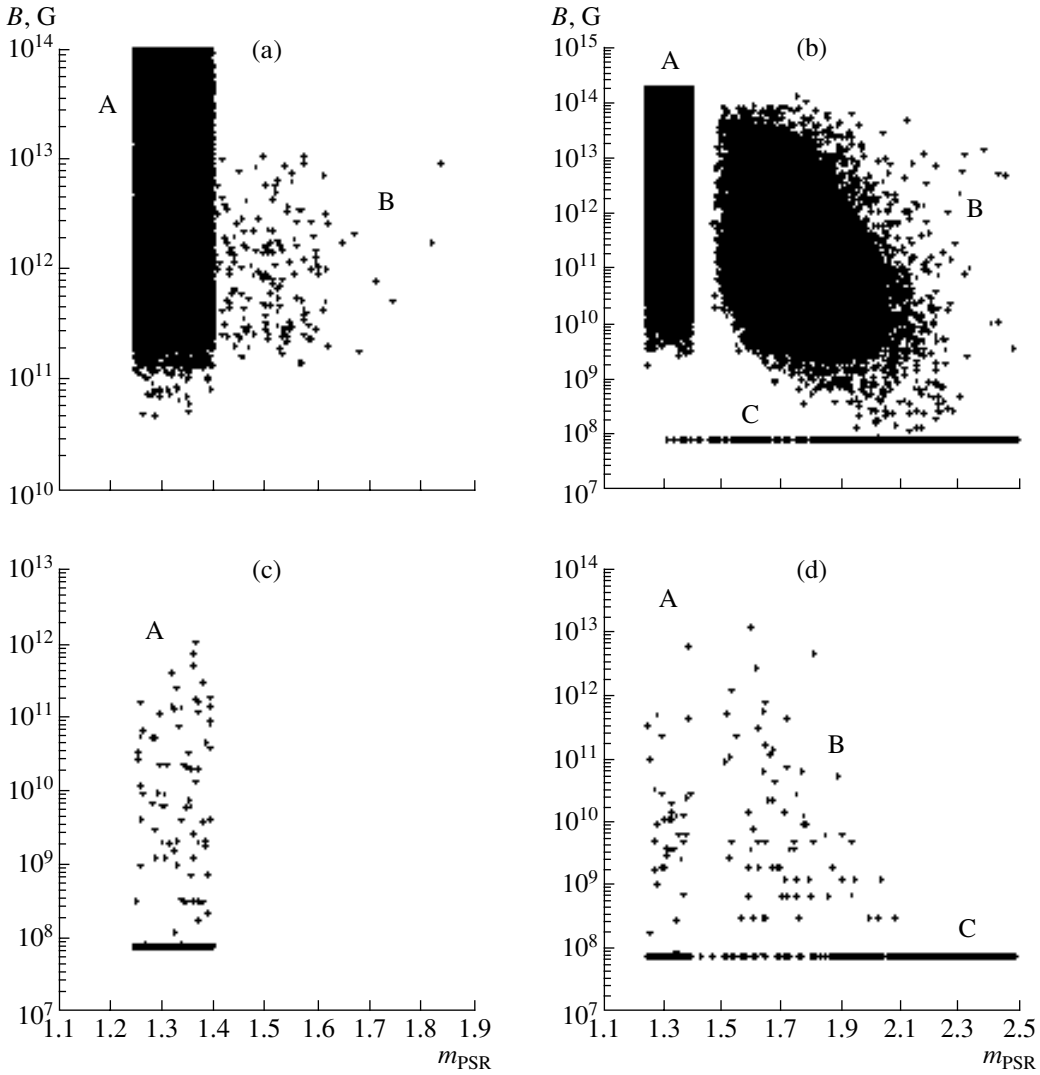

Fig. 8. (a) Masses and magnetic-field strengths of radio pulsars in PSR + NS pairs ($\sim 24 \times 10^4$ systems) obtained in the population-synthesis computations for 72 million initial binaries, taking into account a hyperaccretion stage and allowing for spreads in the initial masses and magnetic-field strengths of the radio pulsars in the ranges $m_{PSR} = 1.25-1.40 M_\odot$ and $B = 2 \times 10^{11} - 2 \times 10^{14}$ G. (b) Same as (a) for radio pulsars in PSR + WD pairs ($\sim 43 \times 10^4$ systems). (c) Masses and magnetic-field strengths of radio pulsars in PSR + NS pairs after correcting the observed number of such systems for selection effects ($\sim$900 systems). (d) Same as (c) for radio pulsars in PSR + WD binaries ($\sim$600 systems).

common-envelope (hyperaccretion) stage produced $\sim 16 \times 10^4$ PSR + WD systems. The masses and magnetic-field strengths for these pulsars are shown in Figs. 7a–7c for magnetic-field decay time scales of $t_d = 10^8$, 5×10^7, and 10^7 yr, respectively.

Let us compare the positions of the groups of radio pulsars in Figs. 7 and 5. In Fig. 7a, groups F and H, whose pulsars accumulate mass predominantly via hyperaccretion, are shifted horizontally toward lower masses compared to those for the same groups in Fig. 5a. In Fig. 7b, groups F, K, and h_1 are likewise shifted toward lower masses compared to those for these groups in Fig. 5b. The same occurs for groups F and f_1 in Fig. 7c (compare to Fig. 5c). The radio pulsars in the remaining groups, which accumulate mass in accretion and superaccretion stages, remained in the same positions (Figs. 5, 7). The initial binary parameters for the various groups of radio pulsars represented in Fig. 7 are listed above.

Note that a radio pulsar can increase its mass to the Oppenheimer–Volkoff limit, $m_{OV} \simeq 2.5 M_\odot$, without passing through a common-envelope stage. It is possible to increase the radio pulsar's mass to $m_{PSR} \simeq 2.5 M_\odot$ only if the stage of accretion from the low-mass donor is long (for radio pulsars of groups B and I in Fig. 7).

Radio Pulsars in PSR + NS and PSR + WD Binaries (Population Synthesis Allowing Ranges in the Initial Binary Parameters and All Types of Accretion)

In the population-synthesis algorithm described above, the initial magnetic-field strength and initial pulsar mass were set equal to $B = 2 \times 10^{12}$ G and $m_{\rm PSR} = 1.35 M_\odot$. Since these initial values can vary, we carried out an additional population-synthesis run for 72 million initial binaries allowing initial magnetic-field strengths from $B = 2 \times 10^{11}$ G to $B = 2 \times 10^{14}$ G and initial pulsar masses in the range $m_{\rm PSR} = 1.25{-}1.40 M_\odot$. The range of initial pulsar masses was based on the masses of the neutron star in the B1913+16 binary system and of the radio pulsar in the J0737−3039 binary. In the B1913+16 system (the Hulse–Taylor pulsar, PSR + NS) the mass of the neutron star, which is definitely not accreting matter from the optical donor, is $m_{NS} = 1.3873 \pm 0.0006 M_\odot$ [13]. The mass of the pulsar in the J0737−3039 system (PSR + PSR), which likewise does not accrete from an optical companion, is $m_{\rm PSR} = 1.250 \pm 0.010 M_\odot$ [20].

The parameters of the PSR + NS ($\sim 24 \times 10^4$) and PSR + WD ($\sim 43 \times 10^4$) systems obtained via the population synthesis are represented in Figs. 8a and 8b.

Group-A radio pulsars in PSR + NS binaries (Fig. 8a) do not increase their masses during their evolution. The range of masses of the group A pulsars is determined purely by the range of initial pulsar masses. The masses of group-B radio pulsars (Fig. 8a) grew predominantly due to hyperaccretion ($\Delta M > 0.1 M_\odot$) and, to a substantially lesser degree, superaccretion ($\Delta M \simeq 0.01{-}0.1 M_\odot$).

The group-A radio pulsars in PSR + WD binaries (Fig. 8b) did not undergo accretion, superaccretion, or hyperaccretion stages. The range of their masses is determined purely by the range of the initial masses. The group-B radio pulsars (Fig. 8b) accumulated masses of $\Delta M \simeq 0.2{-}1.2 M_\odot$ via accretion, superaccretion, and hyperaccretion from optical companions with masses $M_2 \simeq 5{-}10 M_\odot$. The group-C radio pulsars (Fig. 8b) accumulated masses of $\Delta M \simeq 0.1{-}1.2 M_\odot$ via accretion from their low-mass ($M_2 \simeq 1{-}3 M_\odot$) optical companions.

The lower panels of Fig. 8 (c, d) show the samples of PSR + NS and PSR + WD binaries that remain after allowing for observational selection effects. The selection was based on the lifetimes of PSR + NS and PSR + WD binaries. After this effect was taken into account, there remained ∼900 PSR + NS systems (Fig. 8c) and ∼600 PSR + WD systems (Fig. 8d).

The results of the population syntheses corrected for observational selection effects indicate that the masses of radio pulsars in observed PSR + NS systems are confined to the range of their initial masses: from $1.25 M_\odot$ to $1.44 M_\odot$ (Fig. 8c). Correcting for observational selection effects causes pulsars that accumulate mass via hyperaccretion to disappear (Figs. 8a, 8c). All previously selected groups of pulsars in PSR + WD binaries survived after correcting for observational selection effects (Figs. 8b and 8d), though the number of objects in each group decreased. The population-synthesis results indicate that observed masses of radio pulsars in binaries with white dwarfs should be in the range $m_{\rm PSR} = 1.25 M_\odot{-}2.5 M_\odot$.

5. CONCLUSION

The population-synthesis results are in qualitative and quantitative agreement with the observed parameters of radio pulsars in binaries with degenerate companions (Figs. 2, 3, and 8).

Our population syntheses show that PSR + NS systems can contain radio pulsars with masses exceeding the Chandrasekhar limit ($M_{Ch} \simeq 1.4 M_\odot$). The masses of radio pulsars in PSR + NS binaries grow predominantly via hyperaccretion of matter from a massive donor ($M_2 > 10{-}15 M_\odot$). However, it is difficult to observe massive radio pulsars in PSR + NS systems (Fig. 8c), since the lifetimes of PSR + NS pairs with "heavy" radio pulsars ($m_{\rm PSR} > 1.4 M_\odot$) are fairly short. The model computations suggest that radio pulsars with masses $m_{\rm PSR}$ considerably higher than the Chandrasekhar limit, $M_{Ch} \simeq 1.4 M_\odot$, are likely to be present among PSR + WD binaries (Fig. 8d).

The mechanisms via which radio pulsars in PSR + WD pairs accumulate mass are more diverse. In the course of the system's evolution, the pulsar mass can increase due to hyperaccretion, superaccretion, and accretion. Radio pulsars in PSR + WD systems gain the most mass due to accretion of matter from their low-mass optical companions ($M_2 = 1{-}3 M_\odot$). The population-synthesis results indicate that these radio pulsars have weak magnetic fields, $B \simeq 10^8$ G (group C in Figs. 8c and 8d), because their low-mass optical companions fill their Roche lobes on the nuclear time scale, $t \simeq 10^9$ yr. The magnetic fields of the radio pulsars have decayed by two to three orders of magnitude by the onset of the accretion. The radio pulsars J1012+5307 and J1713+0747 (Table 2, Figs. 2 and 3) may belong to this group. The accreted mass supplied by low-mass optical donors is able to increase the mass of the radio pulsar to the Oppenheimer–Volkoff limit, $M_{\rm OV} \simeq 2.5 M_\odot$.

Based on the population-synthesis results, we expect the observed masses of radio pulsars in

PSR + NS and PSR + WD binaries to display a significant scatter, from $1.3M_\odot$ to M_{OV}, due to the accumulation of matter from optical companions. The observed central masses of radio pulsars (Tables 1 and 2 and Fig. 3) are consistent with the population-synthesis results.

ACKNOWLEDGMENTS

The authors are grateful to A.G. Kuranov, K.A. Postnov, and M.E. Prokhorov for valuable remarks and advice. This study was supported by the Russian Foundation for Basic Research (project no. 02-02-17524) and the program "Leading Scientific Schools of Russia" (NSh-388.2003.2).

REFERENCES

1. A. M. Cherepashchuk, Usp. Fiz. Nauk **166**, 809 (1996) [Phys. Usp. **39**, 759 (1996)].
2. A. M. Cherepashchuk, Usp. Fiz. Nauk **173**, 345 (2003) [Phys. Usp. **46**, 335 (2003)].
3. Ya. B. Zel'dovich, Dokl. Akad. Nauk SSSR **155**, 67 (1964) [Sov. Phys. Dokl. **9**, 195 (1964)].
4. E. E. Salpeter, Astrophys. J. **140**, 796 (1964).
5. N. I. Shakura and R. A. Sunyaev, Astron. Astrophys. **24**, 337 (1973).
6. J. E. Pringle and M. J. Rees, Astron. Astrophys. **21**, 1 (1972).
7. I. D. Novikov and K. S. Thorne, in *Black Holes,* Ed. by C. De Witt and B. S. De Witt (Gordon and Breach, London, 1973), p. 343.
8. R. A. Chevalier, Astrophys. J. **411**, L33 (1993).
9. V. M. Lipunov, K. A. Postnov, and M. E. Prokhorov, *The Scenario Machine: Binary Star Population Synthesis*, Ed. by R. A. Sunyaev (Astrophysics and Space Physics Reviews, Harwood Academic Publishers, 1996), Vol. 9.
10. V. M. Lipunov, Astron. Zh. **59**, 888 (1982) [Sov. Astron. **26**, 537 (1982)].
11. Ya. B. Zel'dovich, L. N. Ivanova, and D. K. Nadezhin, Astron. Zh. **49**, 253 (1972) [Sov. Astron. **16**, 209 (1972)].
12. M. M. Basko and R. A. Sunyaev, Astron. Astrophys. **42**, 311 (1975).
13. S. E. Thorsett and D. Chakrabarty, Astrophys. J. **512**, 288 (1999).
14. D. J. Nice, R. W. Sayer, and J. H. Taylor, Astrophys. J. **466**, L87 (1996).
15. M. Konacki, A. Wolszczan, and I. H. Stairs, Astrophys. J. **589**, 495 (2003).
16. I. H. Stairs, S. E. Thorsett, J. H. Taylor, and A. Wolszczan, Astrophys. J. **581**, 501 (2002).
17. J. M. Weisberg and J. H. Taylor, astro-ph/0211217.
18. N. Wex, V. Kalogera, and M. Kramer, Astrophys. J. **528**, 401 (2000).
19. Z. Arzoumanian, M. Cordes, and I. Wasserman, Astrophys. J. **520**, 696 (1999).
20. A. G. Lyne, M. Burgay, M. Kramer, *et al.*, astro-ph/0401086.
21. W. Straten, M. Bailes, M. C. Britton, *et al.*, Nature **412**, 158 (2001).
22. E. M. Splaver, D. J. Nice, Z. Arzoumanian, *et al.*, Astrophys. J. **581**, 509 (2002).
23. F. Camilo, D. J. Nice, J. A. Shrauner, and J. H. Taylor, Astrophys. J. **469**, 819 (1996).
24. M. Bailes, S. M. Ord, H. S. Knight, and A. W. Hotan, astro-ph/0307468.
25. V. M. Kaspi, A. G. Lyne, R. N. Manchester, *et al.*, Astrophys. J. **543**, 321 (2000).
26. D. J. Nice, E. M. Splaver, and I. H. Stairs, in *IAU Symp. No. 218: Young Neutron Stars and Their Environments*, Ed. by F. Camilo and B. M. Gaensler (Astron. Soc. Pacif., San Francisco, 2004), p. 49; astro-ph/0311296.
27. D. J. Nice, E. M. Splaver, and I. H. Stairs, in *Radio Pulsars*, Ed. by M. Bailes, D. J. Nice, and S. E. Thorsett, Astron. Soc. Pacif. Conf. Ser., Vol. 302 (in press); astro-ph/0210637.
28. M. H. van Kerkwijk and S. R. Kulkarni, Astrophys. J. **516**, L25 (1999).
29. J. Kaluzny, S. M. Rucinski, and I. B. Thompson, Astron. J. **125**, 1546 (2003).
30. N. D'Amico, A. G. Lyne, R. N. Manchester, *et al.*, Astrophys. J. **548**, L171 (2001).
31. N. D'Amico, A. Possenti, R. N. Manchester, *et al.*, Astrophys. J. **561**, L89 (2001).
32. W. Coburn, W. A. Heindl, R. E. Rothschild, *et al.*, Astrophys. J. **580**, 394 (2002).
33. P. G. Jonker, M. van der Klis, and P. J. Groot, Mon. Not. R. Astron. Soc. **339**, 663 (2003).
34. P. G. Jonker and M. van der Klis, Astrophys. J. **553**, L43 (2001).
35. A. P. Reynolds, H. Quaintrell, M. D. Still, *et al.*, Mon. Not. R. Astron. Soc. **288**, 43 (1997).
36. H. Tananbaum, H. Gursky, E. Kellogg, *et al.*, Astrophys. J. **174**, L143 (1972).
37. M. K. Abubekerov, E. A. Antokhina, and A. M. Cherepashchuk, Astron. Zh. **81**, 108 (2004) [Astron. Rep. **48**, 89 (2004)].
38. R. Giacconi, H. Gursky, E. Kellogg, *et al.*, Astrophys. J. **167**, L67 (1971).
39. R. L. Kelley, J. G. Jernigan, A. Levine, *et al.*, IAU Circ. No. 3632 (2) (1981).
40. A. La Barbera, L. Burderi, T. Di Salvo, *et al.*, Astrophys. J. **553**, 375 (2001).
41. P. Kahabka and X.-D. Li, Astron. Astrophys. **345**, 117 (1999).
42. N. R. Robba, L. Burdert, T. Di Salvo, *et al.*, Astrophys. J. **562**, 950 (2001).
43. J. E. McClintock, S. Rappaport, P. C. Joss, *et al.*, Astrophys. J. **206**, 99 (1976).
44. V. M. Lipunov, K. A. Postnov, and M. E. Prokhorov, Mon. Not. R. Astron. Soc. **288**, 245 (1997).

Translated by L. Yungel'son

Astronomy Reports, Vol. 49, No. 4, 2005, pp. 309–315. Translated from Astronomicheskiĭ Zhurnal, Vol. 82, No. 4, 2005, pp. 347–354.

A New Classification Scheme for T Tauri Light Curves

N. Z. Ismailov

Shemakha Astrophysical Observatory, National Academy of Sciences of Azerbaijan, Shemakha, 373243 Azerbaijan

Received July 13, 2004; in final form, September 20, 2004

Abstract—Based on many years of observational data from a photometric database on young stars, we propose a new classification scheme for the light curves of classical T Tauri stars. Our analysis of master light-curve shapes for 28 classical T Tauri stars is used to distinguish up to five light-curve types. The proposed scheme suggests a qualitative interpretation in terms of interaction of the central star with its circumstellar accretion disk. © *2005 Pleiades Publishing, Inc.*

1. INTRODUCTION

In addition to their characteristic spectroscopic features, T Tauri stars display irregular brightness variations [1, 2]. Studies over the past fifty years have revealed a wide variety of light curve characters and shapes for various T Tauri stars. Some display strong brightness variations over comparatively short time intervals (months), with brightness increases of up to several magnitudes in some photometric bands [3].

It is currently believed that most "classical" T Tauri stars (CTT stars) can be described by models with a central star with a magnetically active surface surrounded by an accretion disk [4, 5]. The disk is responsible for the observed IR excess. In addition, accretion from the disk favors the generation of excess UV radiation and a stellar wind [6, 7]. Another group of T Tauri stars with lower accretion rates or even with no disk accretion is also known (weak T Tauri stars, WTT stars). How can we explain the observed variety of light curves in the framework of these ideas?

Many classification schemes have been suggested for the light curves of T Tauri stars, taking into account various photometric characteristics (see, for instance, [8–10]). Among existing classification schemes for T Tauri light curves, the scheme of Herbst *et al.* [11], which takes into account the mechanism for the brightness variations, is probably the most complete. Herbst *et al.* [11] assume that the variability of T Tauri stars is mainly associated with rotational brightness modulation due to the presence of a hot spot on the stellar surface (type I), or the appearance of excess radiation that veils the spectrum and brightness, in the case of WTT and CTT stars (type II). The scheme also contains type III variability, which probably occurs only among T Tauri stars with earlier spectral types (ETT stars), and is characterized by large variability amplitudes and insignificant veiling of the radiation. According to [11], the WTT stars belong to type I, both type I and type II are encountered among CTT stars, and both type I and type III are encountered among ETT stars. Transitional objects also exist: individual stars in this group can simultaneously represent different types according to different criteria.

In our opinion, the variability types in the scheme of [11] do not cover all possible T Tauri light-curve shapes. Herbst *et al.* [11] attempted to explain the variety of the light-curve shapes as a result of the simultaneous action of several mechanisms. At the same time, they did not clearly differentiate the studied stars according to their light-curve shapes. The classification scheme for "Orion variables"—now called T Tauri stars—suggested in 1954 by Parenago [8] based on photographic observations is still relevant today. In this scheme, the most important factor is the shape of the light curve.

We suggest here a new scheme distinguishing types of variability of classical T Tauri stars based on their observed light curves compiled from many years of photoelectric observations.

2. OBSERVATIONAL DATA AND RESULTS

We used the photoelectric $UBVR$ observations from the Wesleyan University database (ftp://sun.astro.wesleyan.edu), which is a collection of long-term observations by various authors. These data do not cover all available observations for individual objects, but the amount of material is sufficient to study the general characteristics of the T Tauri stars represented in the database. To avoid biases due to observational selection effects, we chose objects with as many data points as possible accumulated over decades.

1063-7729/05/4904-0309$26.00

Observational data for the studied sample of T Tauri stars

Star	N	T, d	ΔV_1	ΔV_2	$\Delta(U-B)$	$\Delta(B-V)$	Sp	Type	F_1/F	F_2/F	F_1/F_2
BM And	358	5555	2.35	1.04	0.79	0.38	K5V	II	8.71	2.61	3.34
RW Aur a	565	10885	2.66	1.09	0.93	0.69	K1V	II	11.59	2.73	4.25
SU Aur	1129	11665	1.1	0.17	0.51	0.38	G2III	IV	2.75	1.17	2.36
UY Aur	341	4792	3.18	0.82	1.06	1.61	K7V	III	18.71	2.13	8.79
GM Aur	430	4800	0.74	0.3	1.36	0.49	K3V	II	1.98	1.32	1.50
DI Cep	310	6359	0.57	0.19	0.54	0.37	K1V	IV	1.69	1.19	1.42
V521 Cyg	887	4144	1.77	0.31	0.32	0.47	G8	V	5.11	1.33	3.84
V1082 Cyg	464	1963	1.05	0.74	0.82	0.4		II	2.63	1.98	1.33
V1331 Cyg	740	3382	0.73	0.42	0.58	0.12		I	1.96	1.47	1.33
V1121 Oph	491	4090	0.74	0.45	0.68	0.51	k5	III	1.98	1.51	1.31
CO Ori	536	4766	2.68	0.45	0.72	0.37	F8	IV	11.80	1.51	7.80
GW Ori	628	5031	0.63	0.07	0.43	0.23	G5V	V	1.79	1.07	1.67
V866 Sco	354	2280	3.56	1.6	0.42	0.58	k5V	II	26.55	4.37	6.08
T Tau	1357	13050	1.1	0.18	0.79	0.26	K1V	IV	2.75	1.18	2.33
RY Tau	1503	11972	1.25	0.23	0.39	0.15	K1IV	IV	3.16	1.24	2.56
UX Tau ab	418	11612	2.13	0.93	0.78	0.51	K2V	V	7.11	2.36	3.02
AA Tau	386	11972	1.77	0.66	1.5	1.04	K7V	II	5.11	1.84	2.78
BP Tau	556	11969	1.31	0.19	0.78	1.25	K7V	II	3.34	1.19	2.81
CI Tau	332	11603	1.51	0.41	1.12	0.49	K7V	II	4.02	1.46	2.75
DF Tau	744	11972	1.95	0.23	1.8	1.22	M0	II	6.03	1.24	4.88
DG Tau	583	11972	2.15	0.75	0.36	0.36	M?	III	7.24	2.00	3.63
DK Tau	433	11972	1.95	0.23	0.42	0.81	K7V	V	6.03	1.24	4.88
DL Tau	360	11972	2.02	0.8	0.44	0.69	K7V	I	6.42	2.09	3.07
DN Tau	448	11972	0.55	0.34	0.42	0.18	M0V	III	1.66	1.37	1.21
DR Tau	542	11945	3.67	1.81	0.74	0.78	K?	II	29.38	5.30	5.55
GG Tau	443	11588	0.58	0.15	0.62	0.75	K7V	II	1.71	1.15	1.49
GI Tau	416	7296	2.95	1.39	2.18	1.29	K6V	II	15.14	3.60	4.21
GK Tau	501	7296	1.13	0.68	1.23	0.54	K7V	II	2.83	1.87	1.51

We selected a total of 28 classical T Tauri stars (with equivalent widths $W(\mathrm{H}\alpha) \geq 10$ Å) with more than 300 observations in various filters for each from the catalog [12]. The typical photoelectric-photometry uncertainties are about 0.01^m in B and V and, as a rule, no more than 0.03^m in U. We were not able to correct for systematic differences between the data of different authors, but most of the observations for individual stars appear uniform, indicating that such systematic differences are not significant. A list of selected objects and the numbers of measurements for each, N, are presented in the table. We plotted master light curves in various photometric bands for all these stars. After plotting the master light curves for all 28 stars, we attempted to identify general tendencies and differences among these curves.

Figure 1 displays an example of each of the light-curve types we found among the T Tauri stars in our sample. The arrows in Fig. 1b schematically explain our approach to estimating the amplitudes of brightness variations for (i) active states with high amplitudes (ΔV_1) and (ii) quiet states with low amplitudes (ΔV_2), at approximately the same brightness level.

Both existing photometric studies of T Tauri stars and our new results show the following *common features* in the light curves. All the T Tauri stars display irregular brightness variations over several days during various observing seasons. The stars show both quiet and active states. In the quiet state, the daily brightness variations (we will use this term to refer to all brightness variations with time scales within 1–15 days) for individual stars can have amplitudes from 0.07^m to 1.6^m (V866 Sco), but, in most cases,

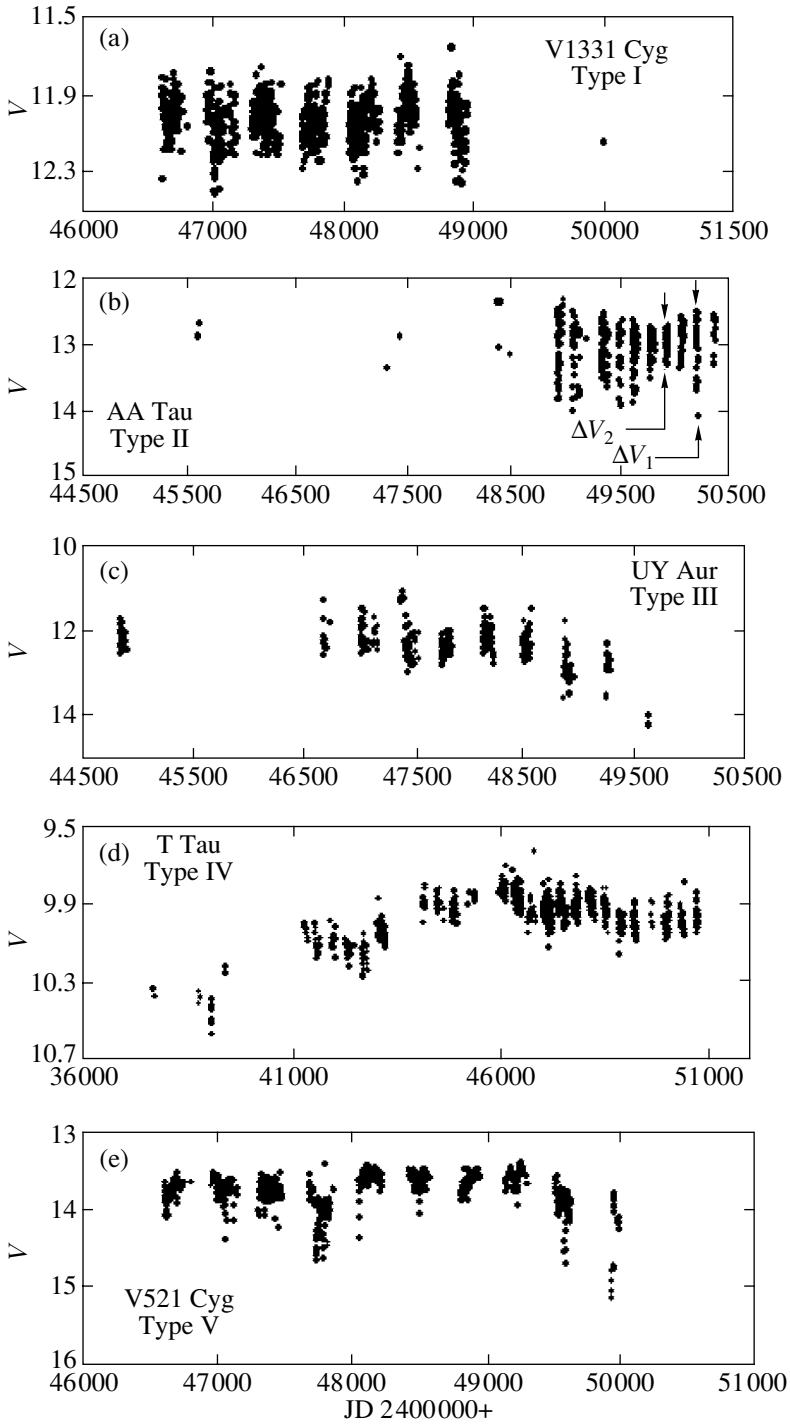

Fig. 1. Characteristic examples of CTT light curves. The arrows in panel (b) explain our technique for estimating amplitudes during different brightness states of the stars.

the V amplitude is within 1^m. Rapid daily brightness variations are observed in both the active and quiet states. The amplitudes of the brightness variations in the active and quiet states, ΔV_1 and ΔV_2 (Fig. 1b), differ, with their ratio being almost constant, on average higher than two.

We determine the active and quiet states of a star as follows. As a rule, during a given time interval, a star displays brightness variations that can be described with two parameters: the mean brightness and the amplitude of the daily variations. Both parameters can differ considerably from season to season. To

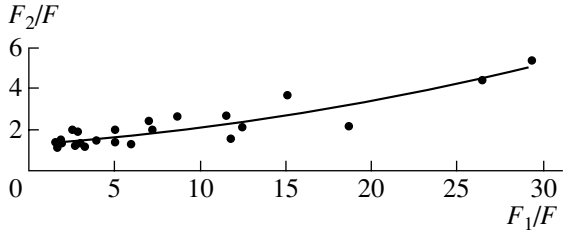

Fig. 2. Relation between the relative amplitudes of the flux variations in the active (F_1/F) and quiet (F_2/F) states for the T Tauri stars. The curve corresponds to a second-order polynomial fit to the data. The correlation coefficient is $r = 82\%$.

study these variations, we selected the extreme states of both parameters. Thus, we can characterize the states of the highest and lowest mean brightnesses. We call these extreme states of the amplitude of the daily variations the star's "active" and "quiet" states. The star's mean brightness in its active and quiet states can be different or virtually the same.

We converted the amplitudes of the brightness variations, ΔV_1 and ΔV_2, derived from the master light curves into relative fluxes, F_1/F and F_2/F, where F_1 and F_2 are the fluxes in the star's active and quiet states (together with any "excess" radiation), F is the flux from the star itself (without excess radiation, taken to be the flux corresponding to the lowest brightness for the whole time interval covered by the observations). The remaining columns of the table present the time interval covered by all available V observations T, the amplitudes for the star's active and quiet states, ΔV_1 and ΔV_2, the highest amplitudes of the color-index variations, $\Delta(U-B)$ and $\Delta(B-V)$, and the spectral type Sp from [12]. This information is followed by the light-curve type according to our classification and the star's relative active-state and quiet-state fluxes F_1/F and F_2/F, along with the ratio of the fluxes in the active and quiet states F_1/F_2.

A direct correlation between the relative fluxes in the active and quiet states of the program stars is observed, shown in Fig. 2. This direct correlation is significant at the 82% confidence level for the approximating polynomial:

$$F_2/F = 0.0024(F_1/F)^2 + 0.0593(F_1/F) + 1.2229.$$

The confidence level for a linear fit becomes lower by 2% compared to the second-power polynomial fit.

Our analysis of the various parameters in the table shows that there is no definite connection between the light-curve type and the rate of the brightness variations or the amplitudes of the brightness variations in different states. This probably indicates that the observed light-curve shapes (types) are not due to different stars having physical states with different natures, but instead reflects different states of essentially similar stars due to external factors, such as binarity, eclipses by dark material, accretion from a circumstellar disk, etc.

Blackbody models for the stellar radiation can be used to derive approximate color indices for individual T Tauri stars [13, 14]. As a rule, the amplitude ΔV of the brightness variations in the quiet state does not exceed 1^m, so that we obtain amplitudes of the $\Delta(U-B)$ and $\Delta(B-V)$ color indices in cool-spot models of 0.3^m and 0.2^m, respectively. However, various studies show that the brightness variations of most stars cannot be described well using such a model. The deviations for individual stars could be due to additional radiation influencing the observed fluxes that has not been taken into account. The largest color-index variations in the table show satisfactory agreement with the cool-spot model only for a few objects. For some stars, a model with a hot spot on the stellar surface can provide a satisfactory description of the data acquired during a single observing season. A typical example is DI Cep, whose seasonal brightness variations can be reproduced assuming variations of a spot's relative area by 2%, with the spot's temperature exceeding the photospheric temperature by 3000 K (cf. [15] and references therein).

We also believe that T Tauri brightness variations could be due to several mechanisms acting simultaneously. Our analysis shows that we can clearly distinguish five different types of light-curve shapes. Figure 3 presents schematic light curves corresponding to our classification scheme. We distinguish the following principal types based on light-curve shape:

type I: constant mean brightness without changes in the amplitude of the rapid brightness variability;

type II: constant mean brightness with changes in the amplitude of the rapid variability;

type III: varying mean brightness without changes in the amplitude of the rapid variability;

type IV: variations of both the mean brightness and the amplitude of the rapid variability;

type V: the variable is often bright, and rare brightness decreases are observed.

Type I stars exhibit brightness variations whose amplitude is almost the same in different years, and whose mean brightness does not vary. Only two stars like this were found in our sample, DL Tau and V1331 Cyg (Fig. 1a). Despite the presence of some scatter about the mean level, the mean brightness itself does not vary. Such variability can be explained by brightness modulation of a cool spot on the surface due to axial rotation of the star. In this case, we must assume that the spots are very stable and that their relative area does not vary within

a season or from season to season. Taking DL Tau ($T_{eff} = 4000$ K) as an example, the color-index variations $\Delta(U-B) = 0.44^m$ accompanied by the V variability amplitude $\Delta V = 2.74^m$ can be explained in a blackbody approximation assuming a change in the observed relative area of a hot spot with a temperature of 2500 K from 0 to 80%.

The mean brightness of the type II stars does not vary, but their rapid variations on time scales of several days are accompanied by gradual changes in their amplitude over several years. For different stars, the minimum and maximum amplitudes of the brightness variations in different years are not identical. Typical representatives of this group are DP Tau and AA Tau (Fig. 1b). This type has the most members in our list (13 stars of 28). Such variations could be due to modulation of the star's brightness in the presence of a hot spot or to variable activity of the star itself, similar to cyclic solar activity, as well as to the appearance of additional radiation associated with nonstationary disk accretion. The light curves of this type suggest that such activity appears and then gradually disappears over five to seven years.

Similar to the type I stars, the type III stars do not show variations in the amplitude of their rapid daily brightness variability; smooth changes of the mean brightness (trends) on time scales of several years are observed. A typical example is DN Tau (Fig. 1c). In our opinion, this type of variability requires the presence of a stellar companion whose brightness is comparable to that of the variable star and comparatively constant. Then, in principle, the brightness variations can be described fairly well using a cool-spot model. Our test calculations show that we can obtain maximum variations of the brightness $\Delta V_1 = 0.55^m$ (see the table) and color index $\Delta(B-V) = 0.18^m$ if the star's temperature is $T_{eff} = 4000$ K and there is a 50% change in the relative area of a cool spot with a temperature of 3500 K. Similarly, the color index variations of DG Tau can be described in a model with a spot having a temperature of 2800 K.

In addition to their rapid daily variations, the type IV stars exhibit simultaneous changes in their variability amplitude within a season, as well as long-term changes in their mean brightness over several years. Most ETT stars are of this type; typical representatives are T Tau and RY Tau. It is likely that, along with seasonal changes due to the star's chromospheric activity, eclipses by an invisible companion or a protoplanet also occur (Fig. 1d). This is essentially the most complex light-curve shape displayed by T Tauri stars from the point of view of interpretation, and requires an individual approach for each object.

The type V stars are usually bright. There are sometimes rapid daily variations with amplitudes of up to 0.5^m, but abrupt dimmings with amplitudes exceeding 1^m in V are also observed in some years. A typical representative is V521 Cyg. If objects such as this exhibit dimmings often and within short time intervals, then the star's light is probably blocked by circumstellar gas and dust (Fig. 1e). When rare dimmings happen only once every two to five years, eclipses by a secondary in a binary system are possible, as in the case of GW Ori [16, 17].

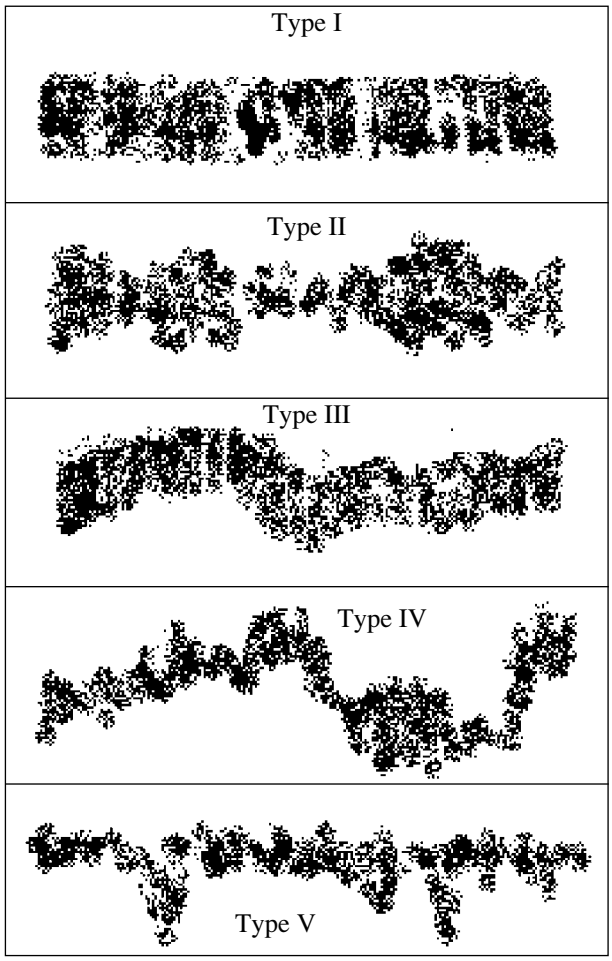

Fig. 3. Schematic classification of light curves for T Tauri stars. In all the diagrams, brightness is plotted along the vertical axis and time along the horizontal axis.

The distribution of the variability amplitudes is also of interest. Though the total number of stars is small, not favoring reliable statistical results, the number of objects is nevertheless sufficient to reveal interesting patterns. For example, Fig. 4a displays the distribution of the V variability amplitudes in the quiet state (ΔV_2). The distribution achieves its maximum near $\Delta V \approx 0.4^m$ and can be described with a fourth-order polynomial (the curves in Fig. 4). For comparison, Fig. 4b displays the distribution of variability amplitudes plotted using the statistical data

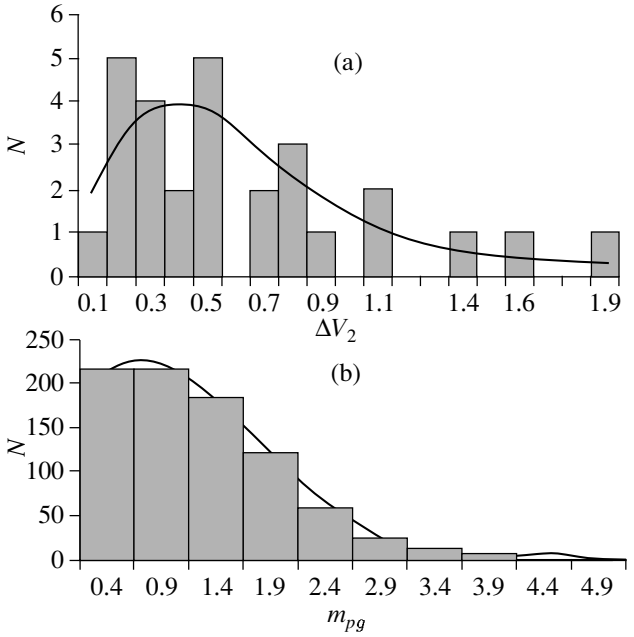

Fig. 4. Distributions of the brightness-variability amplitudes for (a) CTT stars and (b) "Orion variables" according to Parenago [8]. The number of stars, N, is shown along the vertical axis; while the (a) variability amplitude in the quiet state, ΔV_2, and (b) photographic brightness-variation amplitude m_{pg} are laid out on the horizontal axis. The curves are fourth-order polynomials.

of Parenago [8] for all variables in a young cluster in the Orion Nebula. The amplitude distributions for the two samples have approximately the same shape in both diagrams. This suggests that there is a common physical nature for the brightness variations of young stars.

3. FINAL REMARKS AND CONCLUSIONS

Our analysis of master light curves for 28 classical T Tauri stars has enabled us to distinguish five different light-curve types. The main feature—rapid daily variability—is observed for all light-curve types. The main spectroscopic features—hydrogen lines, CaII H and K emission lines, strong absorption in the LiIλ6707 Å line, and forbidden lines of metastable transitions—are observed for all types of T Tauri stars. In addition, the emission spectrum "veils" the star's absorption spectrum. Such distortions of the absorption spectrum are especially pronounced for the classical T Tauri stars [4]. Thus, the spectroscopic features observed for different T Tauri stars differ only in the strength of the radiation in emission; i.e., in the intensity of the shell spectrum.

Let us obtain a simple estimate of the accreted mass needed to provide a V-brightness variation of $\Delta V = 0.5^m$, as is typical of most CTT stars [11].

Many photometric observations of T Tauri stars show brightness variations in the quiet phase of up to several tenths of a magnitude. Let the star have a mass and luminosity equal to the solar values (G2V spectrum). A brightness change $\Delta V = 0.5^m$ will then imply an increase of the radiated flux by a factor of 1.58, and the additional flux for such a brightness variation is $\Delta E = 2.2 \times 10^{33}$ erg s^{-1}. The fastest motions indicated by the observed emission lines of T Tauri stars (including those related to accretion onto the star) have velocities of about 300 km/s (see, for example, [19]). With such velocities for the accreting matter, the energy balance of the additional radiation flux requires a mass of up to $\Delta M = 4.7 \times 10^{22}$ kg, which is about a factor of 100 lower than the mass of the Earth and is comparable to the mass of the Moon. This demonstrates that the variability of stars having type I light curves (constant mean brightness and constant amplitude) can probably not be due to the accretion of matter from a circumstellar disk, because the rate of accretion onto a star cannot be this constant. Type I brightness variations could be due to the presence of a cool spot and/or an active chromosphere.

A simple calculation shows that a large mass, comparable to that of the solar system's planets, can fall onto the stellar surface during an outburst, apparently within a short time (days). Such large brightness variations are characteristic of type IV T Tauri stars. Various stars experience such substantial variations from once every several years to once every several decades. This shows that the interaction between the circumstellar disk and central star is active, and is accompanied by appreciable mass transfer through the circumstellar disk.

All this suggests that a typical, comparatively inactive T Tauri star should have a type I light curve. The other types of light curves can result from additional physical processes influencing the star, such as the accretion of matter from a circumstellar disk, eclipses by circumstellar matter, outbursts, effects associated with binarity, etc. This suggests that the main "stationary" object for all the light-curve types is the star itself, which probably has a magnetically active, spotted surface [18, 19].

Thus, the proposed classification scheme for T Tauri light curves is in reasonable consistency with current concepts concerning mechanisms for the variability of young stars. Note, however, that, bearing all these general features in mind, individual interpretation is needed for each particular observed T Tauri light curve.

Let us summarize the conclusions of this study.

(1) All the light curves observed for classical T Tauri stars can be classified into five types. The

simplest light curves, type I, can be described with stationary cool spot models, while the other light-curve types become increasing complex with increasing type number.

(2) A correlation significant at the 82% level is observed between the brightness-variation amplitudes of T Tauri stars in their active and quiet states.

(3) The distributions of brightness amplitudes for different samples of stars are similar, providing evidence for a common physical nature of the brightness variations of various young stars.

ACKNOWLEDGMENTS

The author thank N.N. Samus' (Institute of Astronomy, Russian Academy of Sciences) for valuable discussions and his assistance during the preparation of the manuscript.

REFERENCES

1. A. H. Joy, Astrophys. J. **110**, 424 (1949).
2. G. H. Herbig, Adv. Astron. Astrophys. **1**, 47 (1962).
3. J. A. Holtzmann, W. Herbst, and J. Booth, Astron. J. **92**, 1387 (1986).
4. E. Gullbring, N. Calvet, J. Muzerolle, *et al.*, Astrophys. J. **544**, 927 (2000).
5. P. Hartigan, L. Hartmann, and J. S. Kenyon, Astrophys. J. **354**, L25 (1990).
6. F. Shu, J. Najita, E. Ostriker, *et al.*, Astrophys. J. **429**, 781 (1994).
7. J. Muzerolle, L. Hartmann, and N. Calvet, Astrophys. J. **550**, 944 (2001).
8. P. P. Perenago, Tr. Gos. Astron. Inst. Shternberga **25** (1954).
9. M. Cohen and R. D. Schwartz, Mon. Not. R. Astron. Soc. **174**, 137 (1976).
10. J. T. Schmelz, Astron. J. **89**, 108 (1984).
11. W. Herbst, D. K. Herbst, and E. J. Grossman, Astron. J. **108**, 1906 (1994).
12. G. H. Herbig and K. R. Bell, Lick Obs. Bull., No. 1111 (1988).
13. J. A. Holtzman, W. Herbst, and J. Booth, Astron. J. **92**, 1387 (1986).
14. J. Bouvier, S. Cabrit, M. Fernandez, *et al.*, Astron. Astrophys. **272**, 176 (1993).
15. N. Z. Ismailov, Astron. Zh. **81**, 431 (2004) [Astron. Rep. **48**, 393 (2004)].
16. N. Z. Ismailov, Kinematika Fiz. Nebesnykh Tel **9**, 65 (1993).
17. V. S. Shevchenko, K. N. Grankin, S. Yu. Mel'nikov, *et al.*, Pis'ma Astron. Zh. **24**, 614 (1998) [Astron. Lett. **24**, 528 (1998)].
18. C. M. Johns-Krull, J. A. Valenty, and J. L. Linsky, Astrophys. J. **539**, 815 (2000).
19. P. P. Petrov, G. V. Zajtseva, Yu. S. Efimov, *et al.*, Astron. Astrophys. **341**, 553 (1999).

Translated by N. Samus'

Astronomy Reports, Vol. 49, No. 4, 2005, pp. 316–326. Translated from Astronomicheskiĭ Zhurnal, Vol. 82, No. 4, 2005, pp. 355–367.

Methanol Proplyds and a Double Protoplanetary System in the Constellation Norma

I. E. Val'tts and S. Yu. Lyubchenko

Astro Space Center, Lebedev Physical Institute, Russian Academy of Sciences, Moscow, Russia

Received June 25, 2004; in final form, September 20, 2004

Abstract—We have carried out detailed studies of a star-forming region containing two maser sources in the constellation Norma. The sources display a complex spectral distribution of the maser lines and spatial distribution of the maser condensations. The maser condensations may have formed around objects that are hidden by dense molecular cocoons; the velocities of the maser features may represent Keplerian orbital motions. The cocoons, which radiate in thermal methanol and CS lines, correspond to the centers of mass in the maser sources + dense molecular core systems. The velocities of the CS lines or thermal methanol lines can be used to identify the locations of the centers of mass of these systems. If the maser radiation is generated in the atmospheres of protoplanets, the Norma radio source may correspond to two protoplanetary disks, each with a protostar and protoplanetary system. In this case, the masses of the protostars are approximately 13 $M_\odot$ and 38 $M_\odot$. © *2005 Pleiades Publishing, Inc.*

1. INTRODUCTION

Radio-spectroscopic observations of star-forming regions containing dense clumps of gas and dust with various molecular compounds are very promising for studies of the physical states of prestellar material. Radio lines emitted by such clumps can be related to various temporal, dynamical, and thermal evolutionary phases of the interstellar medium, and the parameters obtained from the observed emission of various molecules can be used to reconstruct the physical conditions in star-forming regions. Some molecules in prestellar condensates are subject to intense irradiation from neighboring, recently formed, young stars or to dynamical compression by flows of matter from neighboring stars, both of which can act to redistribute the level populations. This can result in nonequilibrium (maser) radiation by these molecules, which are virtually always found in association with protostellar objects. The spatial structures of the maser condensations shows that they are often laid out in chains or arcs, sometimes displaying characteristics consistent with Keplerian disks containing protoplanetary systems. Such disks are called protoplanetary disks, or proplyds [1].

Recent studies of methanol masers at 6.7 and 12.2 GHz are particularly relevant in this sense [2–9].

Interferometric observations can sometimes be used to estimate the sizes of condensates and distances between them, as well as the masses of the clumps of material in which the masers are formed, if some assumptions about the interactions between the maser clumps are adopted [3, 4, 7]. However, in some cases, the spectral distribution of the maser features is too complex to yield an unambiguous picture of the structure of the studied region. In such situations, additional detailed studies of the source morphology, including analyses of emission in thermal molecular lines or in other wavebands, are required. One example is a star-forming region containing two maser sources in the constellation Norma, with which we will be concerned in this paper.

2. DESCRIPTION OF THE MASER REGION

The studied region contains two maser sources with very similar coordinates: 328.237−0.547 and 328.254−0.532. The region is located in the southern hemisphere in the constellation Norma in the arm of Sagittarius, at a distance of about 3 kpc from the Sun (this is close to the "near" kinematic distance; one of the earliest distance estimates was 2.9 kpc [10]). It is not far from the Galactic center in a region that does not contain an especially large amount of gaseous and dusty material. As is often the case in very early stages of star formation, the region has no identification in the optical range. However, 6 cm radio observations show the presence of an HII region [11]. An OH maser was discovered at the edge of this HII zone [10, 12].

It later turned out that there are two OH masers in this region, which are also associated with methanol masers [13]: the southern (S) maser 328.237−0.547 and the northern (N) maser 328.254−0.532. The OH spectra of Caswell *et al.* [10] were obtained for the coordinates of the southern source using the Parkes

1063-7729/05/4904-0316$26.00

64-m telescope, which has a 12′ beam that also received emission from the northern source. The coordinates of the masers were obtained with an accuracy better than 1″ using the ATCA at Narrabri [2, 14]. The ATCA beam was only 7″ at the OH frequency, 1.6 GHz, and only 2″ at the methanol frequency, 6.7 GHz, making it possible to demonstrate that the two radiation maxima have different velocities (approximately −45 km/s and −37 km/s) and different spatial coordinates, being separated by 80″. The brighter methanol masers according to their peak line intensities are concentrated in the northern source, which also contains the source IRAS15541−5349, which is an ultracompact HII region according to the criterion of Wood and Churchwell [15]. On this basis, the list of ultracompact HII regions of Walsh *et al.* [16] presents the coordinates of the northern source, toward which Walsh *et al.* [16] had observed 6.7 GHz methanol emission, in the direction of the HII region.

However, ATCA continuum observations with higher angular resolution [4] showed that this ultracompact HII region is associated with the southern, weaker methanol-maser source, and has no relation to IRAS15541−5349. Walsh *et al.* [16] observed 6.7 GHz methanol maser emission in the direction of the ultracompact HII region using the 64-m Parkes telescope, whose beam encompasses both sources at both 6.7 GHz (3.3′) and 1665 MHz.

Note that the accuracy of the coordinates in the IRAS catalog is such that IRAS15541−5349 may not be coincident with the northern source, and could be located further to the south.

H_2O maser emission was discovered in this region using observations on the 14-m Itapetinga telescope of the University of São Paolo in Brazil, which has a 4.5′ beam [17]. Thus, it was not possible to determine whether this maser was associated with the northern or southern source. One of the H_2O maser spectral features has a velocity (−45 km/s) that is close to that of the southern methanol maser, while another feature has a velocity of −24 km/s, which is not clearly identifiable with either the northern or the southern source.

The maser region has apparently not been studied in thermal CS lines, which are formed in dense molecular clouds. The region was not included in the large survey of $C^{32}S$ and $C^{34}S$ line emission from H_2O masers carried out by Juvela [18]. In their catalog of IRAS sources with the characteristics of star-forming regions, Bronfman *et al.* [19] present CS(2−1) emission-line data for IRAS15539−5353, which is located about 1.5′ to the south of the southern maser. Since these CS(2−1) observations were carried out using the 15-m SEST telescope with a 50″ beam, which encompasses a region that is close to the maser region in which we are interested, it is possible that some of the molecular-cloud properties for IRAS15539−5353 derived from the CS(2−1) profile—in particular, the velocity of the quiescent gas, −42.5 km/s—are associated at least partially with the southern maser source.

The cloud velocity indicated by formaldehyde absorption lines at the 2_{11}-2_{12} transition at 14.5 GHz observed with a 2.15′ beam is −42.7 km/s, while the velocity observed for the 1_{10}-1_{11} transition at 4.8 GHz in the 4.2′ beam is $V_{LSR} = -42.4$ km/s [20]. The cloud velocity in the $C^{18}O(2-1)$ line is −43.69 km/s (SEST, 24″ beam, 219.6 GHz [21]). The radial velocities of the SiO(2−1) (87 GHz) and SiO(3−2) (130 GHz) lines (SEST, 57″ and 40″ beams, respectively) are approximately −41 km/s toward the southern maser and −43 km/s toward the northern maser [22]. In principle, the SiO lines could be blended with maser lines, but we will take them to be thermal, as did Harju *et al.* [22]. We will make use of all this observational information below.

Figure 1 shows various images of the sources described above. Table 1 presents the parameters of the radio lines observed in this region (peak fluxes of the strongest features and velocities of the peaks).

Figures 2a and 2b present collected spectra of observed lines for the southern and northern sources, respectively. For convenience, all the spectra are presented on a single radial-velocity scale. The figure contains seven windows, which present, from top to bottom, (1) the 6.7 GHz methanol spectrum of [4], (2) the 12.2 GHz methanol spectrum of [24], (3) the 44 GHz methanol spectrum of [25], (4) the 95 GHz methanol spectrum of [26], (5, double window) the OH-maser spectrum published by Robinson *et al.* [12] and then later by Caswell *et al.* [10], (6) the H_2O spectrum, and (7) the thermal SiO line spectrum [22]. The methanol masers whose spectrum is presented in the third and fourth windows from the top are associated with the southern source, while only an upper limit for the intensities of these lines was obtained for the northern source [25, 26], and we accordingly present for the northern source only the corresponding noise corridors from the windows for the southern source. The OH (window 5) and H_2O (window 6) spectra were obtained with beams that were large enough to encompass both sources. Let us now consider the methanol spectra in more detail.

3. METHANOL: MASER AND THERMAL EMISSION

The most powerful methanol masers in this region are those observed at 6.7 and 12.2 GHz, and belong

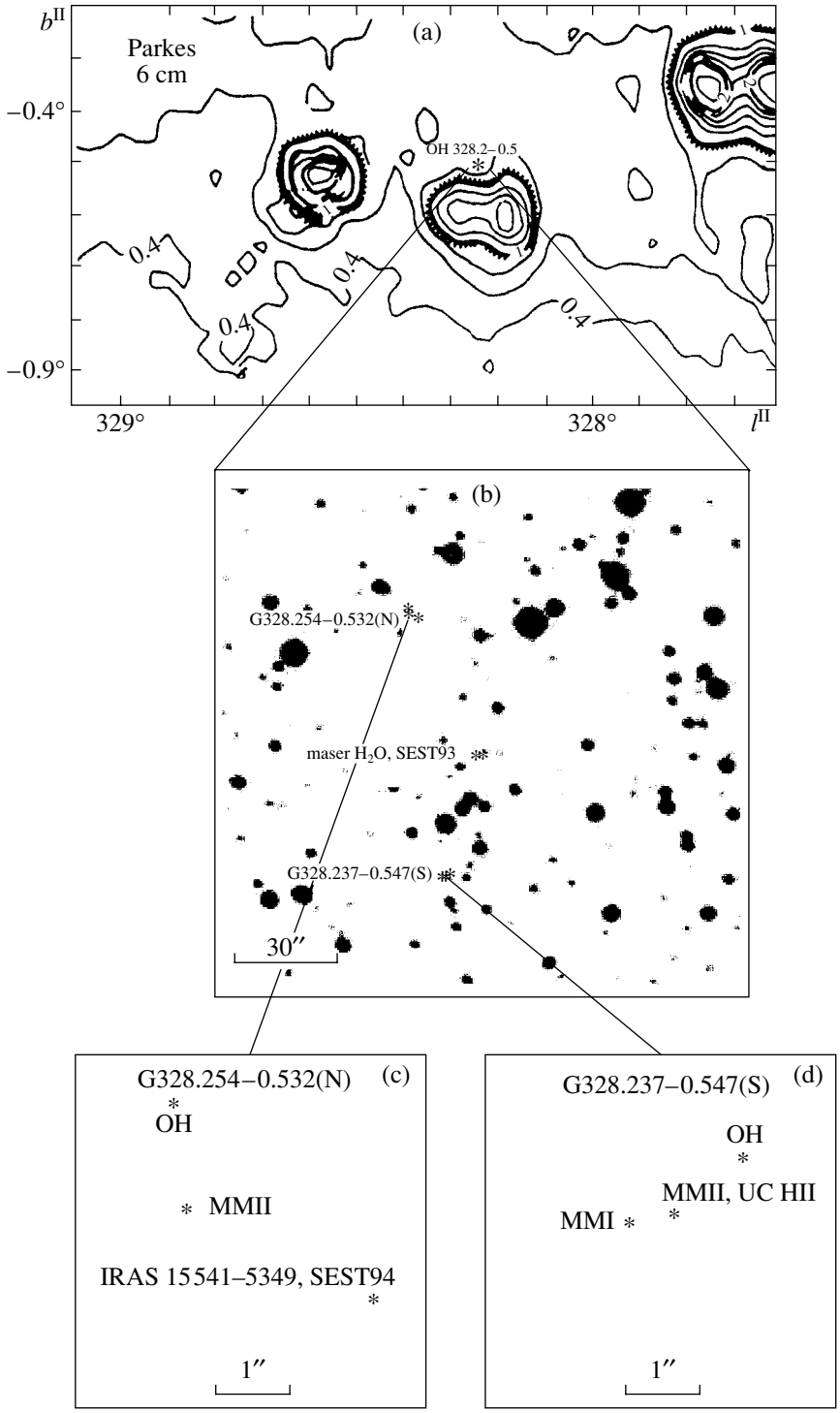

Fig. 1. Locations of the methanol masers G328.237−0.547(S) and G328.254−0.532(N) in the constellation Norma. (a) An extensive HII region in 6 cm [11], at the edge of which are located OH and methanol masers. (b) Optical image from the CDS database (Aladin Sky Atlas, http://aladin.u-strasbg.fr; the scale is indicated in the lower left-hand corner). (c, d) The maser regions on a larger scale.

to class II [27]. Thermal emission is observed at 107 and 156.6 GHz, where class-II maser emission is also sometimes observed [23]. Images of the 6.7 GHz maser region obtained with the ATCA with a resolution of 0.02″ by Norris *et al.* [2] showed the complex spatial structure for the source, and confirmed that the source has a northern and southern part separated by 80″ North−South. Each of these parts, in turn, contains several spatial features (Fig. 1). Each source has both strong and weak maser components.

Table 1. Parameters of radio lines observed toward the maser sources G328.237−0.547 (S) and G328.254−0.532 (N)

Molecule frequency, GHz, or transition	G328.237−0.547(S) RA(1950) = $15^h54^m05.99^s$ Dec(1950) = $-53°50'46.9''$			G328.254−0.532(N) RA(1950) = $15^h54^m07.46^s$ Dec(1950) = $-53°49'24.7''$		
	peak flux of strongest feature, Jy	V_{LSR}, km/s	Ref.	flux at peak of strongest feature, Jy	V_{LSR}, km/s	Ref.
1	2	3	4	5	6	7
CH_3OH						
(6.7)	400	−44.8	[14]	430	−37.4	[14]
CH_3OH						
(12.2)	13	−44.8	[23]	3.3	−37.0	[23]
CH_3OH						
(107)	<0.9	−41.6	[27]	2.6	−42.8	[27]
CH_3OH						
(156.6)	3.6	−41.6	[27]	?	−42.8	[27]
CH_3OH						
(44)	11.9	−41.1	[24]	<(5−10)	−45.0	[24]
CH_3OH						
(95)	7.3	−41.2	[25]	−	−	[25]
OH						
(1.665)	12.0	−45 . . . − 40	[13]	8.0	−45 . . . − 35	[13]
H_2O						
(22)	5.3	−45.0	[17]	−	−	[17]
SiO						
(2-1)	0.21*	−40.8	[22]	0.43*	-43.2	[22]
(3-2)	0.15*	−41.4	[22]	0.49*	-43.0	[22]

Note: Coordinates taken from [23]. The asterisks mark antenna temperatures in K.

The spectral components corresponding to the spatial features are arranged in the spectrum crosswise in radial velocity (Fig. 2) and symmetrically about the center of the spectrum. This is intriguing, since it is most natural to expect that maser features belonging spatially to one of the sources should be concentrated in velocity near the maximum for that source, and, in any case, should not be arranged symmetrically about the center of the spectrum for both sources.

In their high-resolution study of the vicinity of the methanol-maser region, Phillips *et al.* [4] determined the masses of central objects assuming Keplerian disks corresponding to this maser region using the interferometric data of Norris *et al.* [2]. Imaging of the 8.6 GHz continuum emission using the ATCA ($1.5'' \times 1.1''$ beam) [4] revealed an ultracompact HII region in the southern source, as we indicated above. We will consider this work further in Section 5 below. In the following section, we will determine to what physically correspond the centers of the maser spectra.

4. CENTERS OF THE SYSTEMS

To determine the positions of the centers of the masers in these two sources, we will turn to our previous paper [28], which was dedicated to the relative positions of maser and thermal methanol lines in the spectra of a large sample of sources. In [28], we analyzed the spectra of 30 class II methanol masers at 6.7 and 12.2 GHz and their associated maser, quasi-maser and thermal lines at 107 and 156.6 GHz,

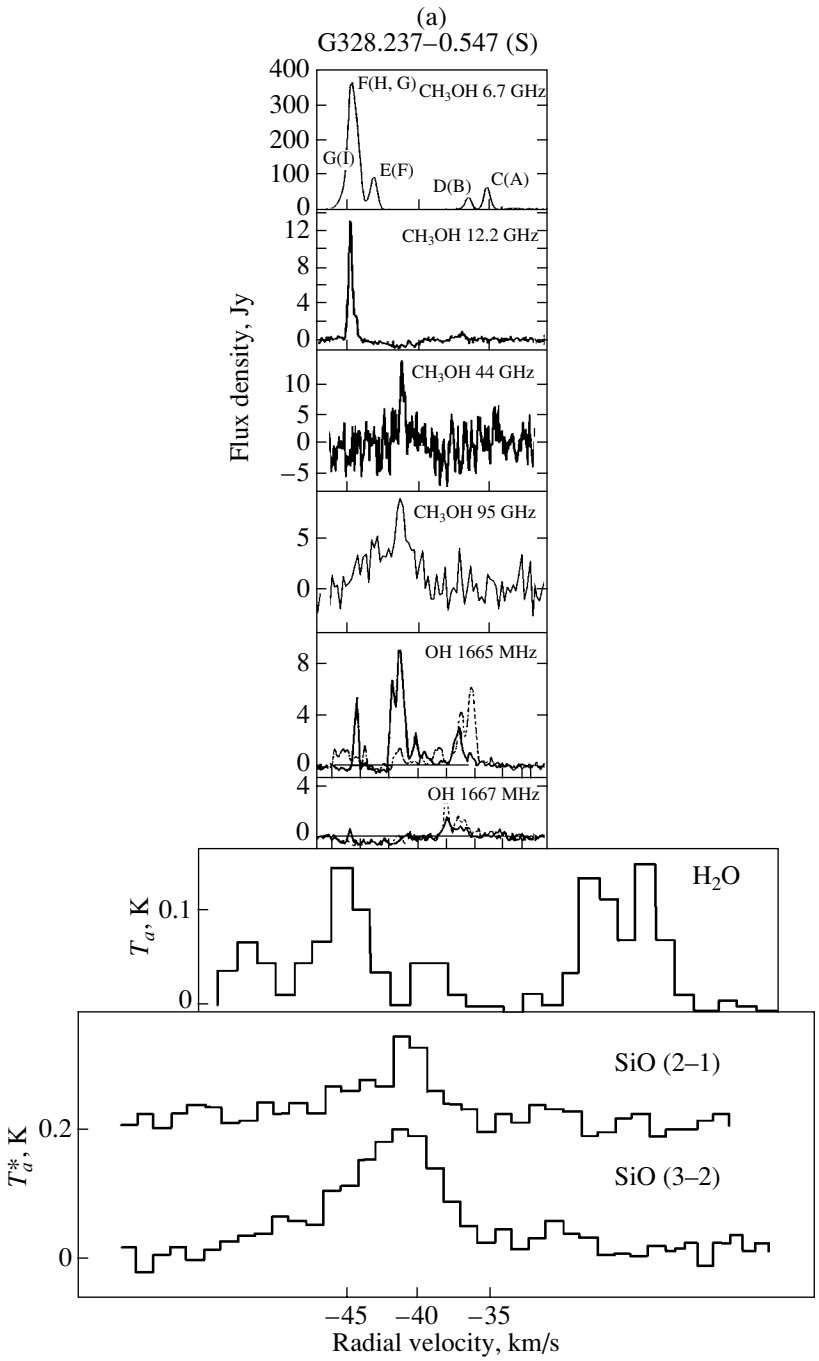

Fig. 2. Radio-line spectra for (a) G328.237−0.547(S) and (b) G328.254−0.532(N). A description of the original data is given in the text.

together with the thermal CS(2−1) line. In many cases, class II methanol maser lines form two clusters positioned symmetrically about the radial velocity at which the thermal methanol and thermal CS molecular emission is observed. This result was subsequently confirmed using a larger sample (80 sources) containing only maser lines at 6.7 and 12.2 GHz and thermal CS lines.

The results of [28] suggested that the velocities of the masers and of the sources of thermal emission are connected. If we suppose that the maser condensations are orbiting around some object hidden by a dense molecular cocoon, the velocities of the maser features could represent Keplerian orbital velocities, while the cocoon, which radiates in thermal methanol and CS lines, corresponds to the center of mass of the system formed by the maser sources and the dense molecular core. In this case, it is a simple matter to explain the presence of two clusters of lines on either side of a thermal line: they correspond to the

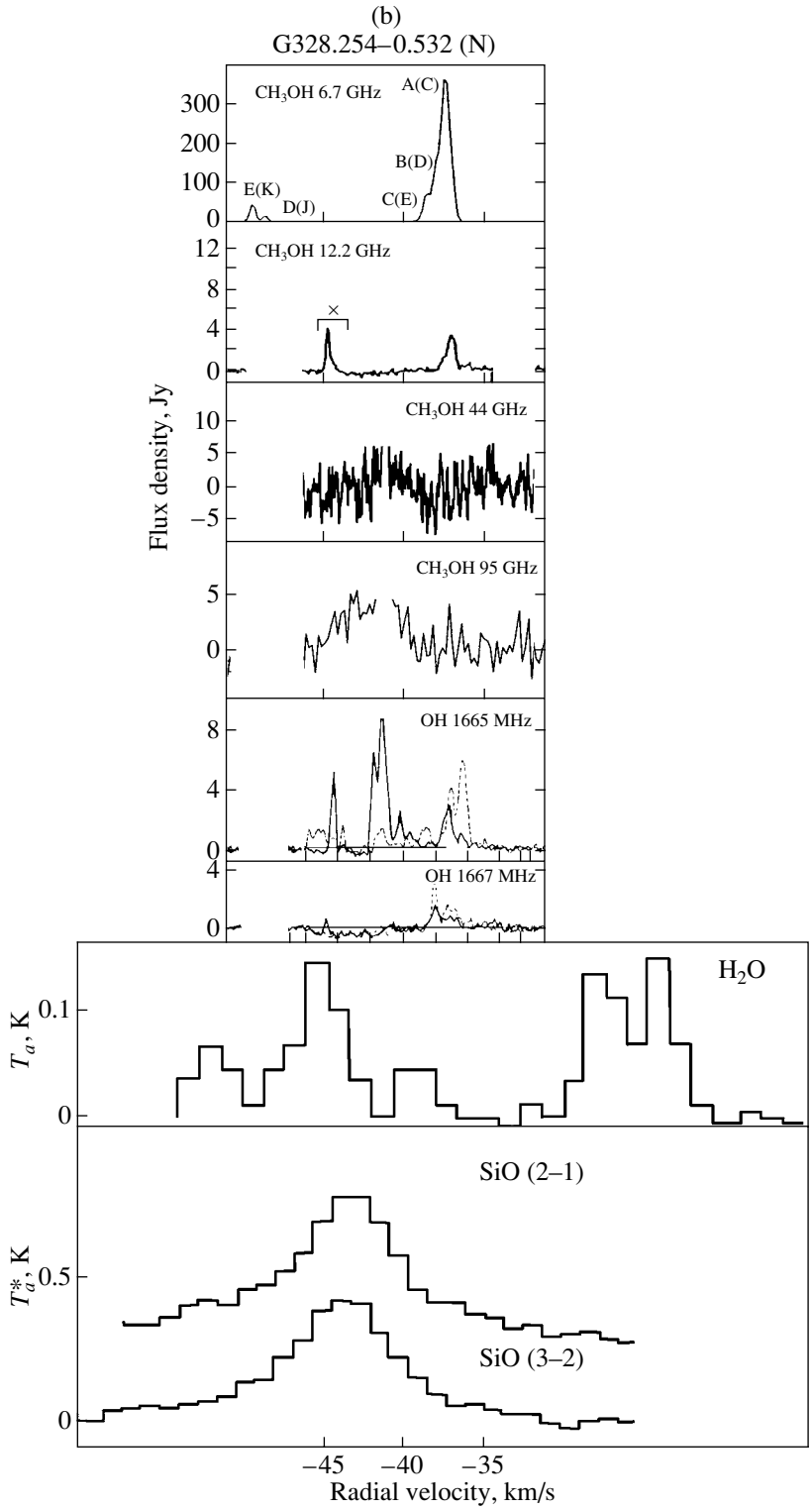

Fig. 2. (Contd.)

two sections of an orbit where the motion is along the line of sight, two parts of a ring centered on the central object, or two edges of a disk (about the central object) that is hidden by a gas–dust core that radiates thermal line emission at the velocity of the unperturbed molecular cloud.

Slysh *et al.* [6] showed that class II maser emission could arise in the atmospheres of icy protoplanets. Some arguments in support of this hypothesis were also presented in [9]. As a protoplanet forms, it acquires a Keplerian velocity, determined as the radial velocity of maser features emitted in its atmosphere,

while the center of mass of the system retains the former velocity of the molecular cloud. The velocity of thermal CS or methanol lines corresponds to the spatial location and center-of-mass velocity of the protoplanetary system [9].

Let us suppose that we are observing Norma protoplanetary systems surrounding two protostars. There are no thermal CS data for this star-forming region, and the thermal methanol emission is very weak. It may be that the evolutionary stage in the southern and northern sources is such that they do not yet have molecular cocoons. The ultracompact HII region is observed in the southern source, whose maser emission is weaker, consistent with the idea that the southern protostar has become a young star that is capable of ionizing the surrounding gas. The fact that no HII region is observed in the northern source may indicate that the northern protostar is in an earlier stage of evolution. However, in both the northern and southern sources, information about the velocity of these central bodies—the southern star and northern protostar—is preserved. This information can be extracted from the parameters of the weak thermal methanol lines at 107 and 156.6 GHz and the thermal SiO lines, as well as the class I methanol masers (for the southern source), which are known to have nearly the same velocity as the parent molecular cloud (see, for example, [29, 30]). According to the data in Table 1, the mean velocities for these lines are -41.2 km/s for the southern source and -43.5 km/s for the northern source. We will take these to be the velocities of the two protostars. In this case, the parameters of the Keplerian disks, i.e., the velocities of protoplanets in Keplerian orbits corresponding to the velocities of the class II masers, are known, as well as the velocities of the protostars, and the masses of the central objects can be determined.

5. MASSES OF THE CENTRAL PROTOSTARS

Figures 3a–3c present the total spectrum together with separate maps of the 6.7 GHz methanol masers of the southern and northern sources, taken from Norris *et al.* [2]. The linear scales in Figs. 3b and 3c from [2] are indicated in the lower left-hand corners of the maps. Figures 3d and 3e present the corresponding velocity–distance diagrams of [4]. Phillips *et al.* [4] used the data of Norris *et al.* [2] to construct these diagrams; the maps presented in [4] are the same as those in [2] but on a larger scale.

The component names in parentheses in the velocity–distance diagrams (Figs. 3d and 3e) correspond to the notation of [4]; see also the spectra of [4] presented in Figs. 2a and 2b. Components (A) and (B) in the southern source are not present on the maps of Norris *et al.* [2]. We modified the labeling of the components in the diagrams in order to denote the correspondences to the line intensities.

If the radial velocities of the methanol features are Keplerian, then spectral components with higher velocities should be located in space closer to the center of the system, while those with lower velocities should be located further from the center. The general pattern shown by the spectra and maps is consistent with Keplerian rotation of spatial features corresponding to the methanol masers, but is not entirely adequately described by this simple picture: generally speaking, the positions of the components could reflect some configuration of protoplanets in orbits, or their angle to the plane of the sky.

In the map of the southern source, component HG(F) is located closer to the center of the system than component F(E). Component I(G) is poorly resolved in the spectrum, and it is possible that its spatial position is not determined with certainty. The positions of components B(D) and A(C) do not correspond to the expectations of our hypothesis, and we did not use these components when finding the mass of the protostars. Note that the weaker components (A) and (B) distinguished by Phillips *et al.* [4] have the expected spectral positions (see also the spectrum in Fig. 2a).

In the map of the northern source, components C(A), D(B), and E(C) can be considered "degenerate." However, component K(E) is located in the spectrum further from the center than component J(D), and is located closer to the center of the system in the diagram, if we crudely estimate their spatial positions using the projection of their spatial coordinates onto the line joining the group CDE and these two components—as is appropriate if the velocities of the spectral components reflect the circular velocities of protoplanets in their orbits.

We can refine the positions of the centers of mass (assuming the motion of protoplanets in circular orbits) using equations for pairs of methanol-maser spatial components:

$$\Delta V_i^2 x = \Delta V_j^2 (r - x), \qquad (1)$$

where ΔV_i is the velocity of a component relative to the central object in km/s, r is the distance between the components in the pair in milliarcseconds (mas), and x is the distance between one of these components and the central object in mas.

The mass of the central object is determined from the equation

$$\frac{GMm}{x^2} = \frac{mV_i^2}{x} \qquad (2)$$

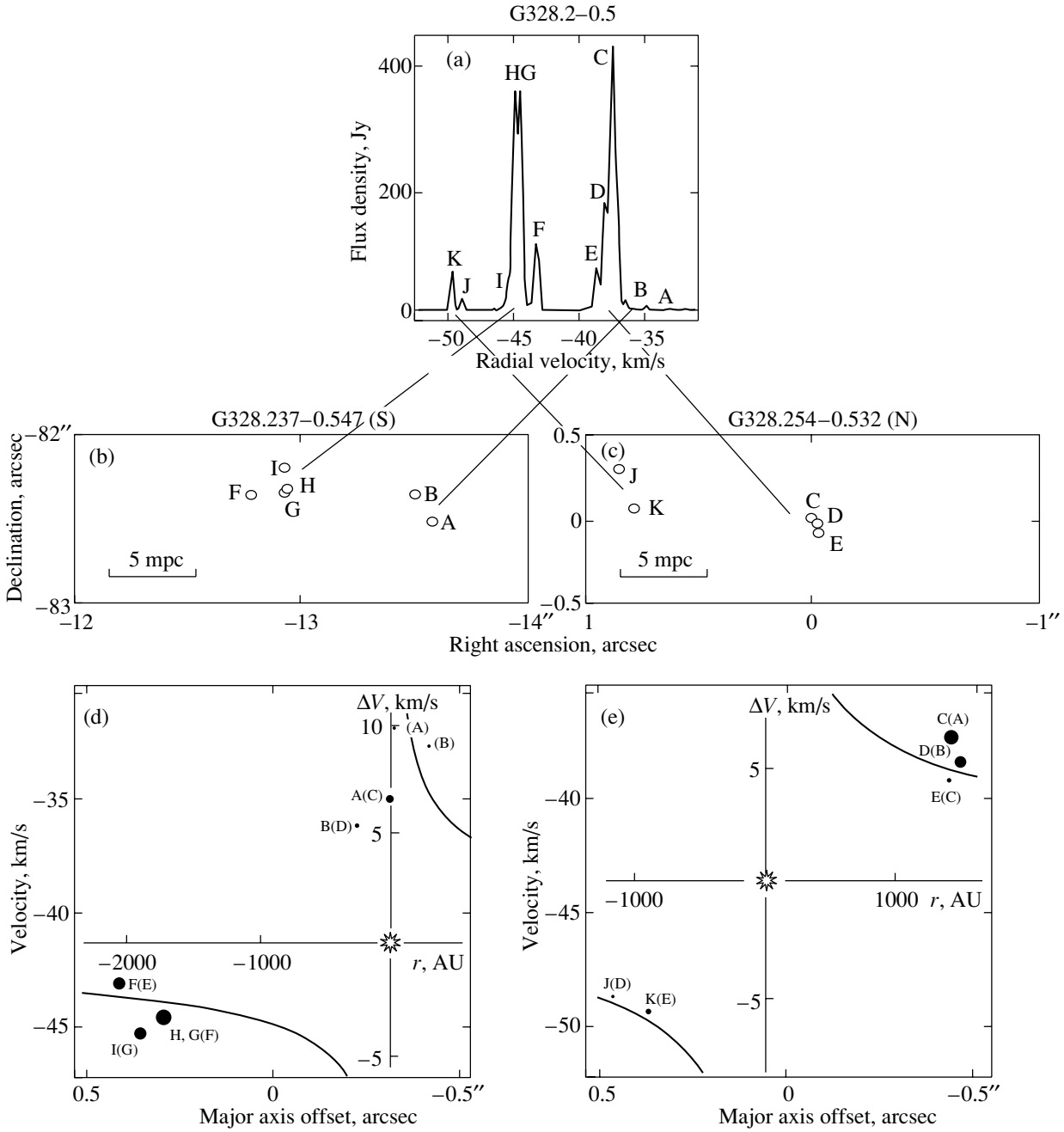

Fig. 3. (a) Total spectrum for the northern and southern components of G328.2−0.5. (b, c) Individual maps of the southern (b) and northern (c) sources based on the 6.7 GHz ATCA observations of [2]. (d, e) Velocity–distance diagrams from [4] (see text for more detail). Superposed are the new source axes and the positions of the protostars derived from the ratios of the velocities of the maser and thermal lines. The positions of the protostars in the southern and northern sources are shown in (c) and (d): the velocity of the protostar corresponds to the mean velocity of the thermal lines, and the position of the protostar along the distance axis is calculated using the spectral and spatial characteristics of the methanol maser lines presented in Table 2. The curves correspond to a Keplerian dependence of the velocity on the mass for protostar masses $\overline{M} = 13.3M_\odot$ in the southern source and $\overline{M} = 37.6M_\odot$ in the northern source.

(where G is the gravitational constant, m is the mass of the protoplanet, M is the mass of the central object, and V_i is the orbital velocity of the protoplanet), from which we can obtain the relation

$$M = \Delta V_i^2 x D \times 10^{-3}, \qquad (3)$$

where M is the mass of the central object in solar masses ($M_\odot$), ΔV_i is the velocity of the protoplanet in km/s, x is the distance of the protoplanet from the central object in mas, and D is the distance of the protoplanetary system from the Earth in kiloparsec.

Table 2. Masses of the protostars in the two radio sources in Norma

Components of the system of protoplanets	ΔV_i, km/s	ΔV_j, km/s	r, mas	x, mas	M, $M_\odot$
G328.237−0.547(S)					
$V_{\rm therm} = -41.2$ km/s					
H,G(F)–(B)	3.4	8.4	720	617	20.0
H,G(F)–(A)	3.4	9.2	620	546	17.7
F(E)–(B)	1.9	8.4	840	799	8.1
F(E)–(A)	1.9	9.2	740	710	7.2
			$\overline{r} = 730$ mas (2044 AU)		$\overline{M} = 13.3M_\odot$
G328.254−0.532 (N)					
$V_{\rm therm} = -43.5$ km/s					
J(D)–D(B)	5.3	5.0	920	438	33.8
J(D)–C(A)	5.3	6.3	900	527	40.7
K(E)–D(B)	6.0	5.0	820	336	33.9
K(E)–C(A)	6.0	6.3	800	417	42.0
			$\overline{r} = 860$ mas (2408 AU)		$\overline{M} = 37.6M_\odot$

Note: The calculations were carried out for a near kinematic distance of 2.8 kpc. The components of the protoplanetary system are denoted in accordance with Norris *et al*. [2], with the notation of Phillips *et al*. [4] given in parentheses.

If we suppose that each pair can formally represent an individual ring with two protoplanets, we can compare the equations for the pairs listed in Table 2. The calculated corrections to the positions of the centers of the systems and masses for the central sources are also presented in Table 2.

The velocity–distance diagrams (Figs. 3d, 3e) also show the positions of the protostars in the southern and northern sources derived from our calculations. The velocity of a protostar corresponds to the mean velocity of the thermal lines presented in Table 1, and its distance to the average of the three distances between the protoplanet and central object obtained for the pairs of methanol components presented in Table 2. The position of the protostar is at the center of a new system of coordinates, shown together with dependences in this new system corresponding to (2), in which the mass of the protostar is a parameter; we obtained $\overline{M} = 13.3M_\odot$ for the southern source and $\overline{M} = 37.6M_\odot$ for the northern source.

Of course, our calculations are only approximate, since numerical values for the interferometric data and velocities of the spectral features were not published, and we read the required information off the published plots. It would be interesting to determine the real errors on the masses, based on the correct numerical values for the input data.

6. UNCERTAINTIES IN THE ESTIMATED PROTOSTAR MASSES

6.1. Distances to the Regions

The largest errors contributed by distances derived from the differential rotation curve for the Galaxy is associated with the choice of solution for the rotation curve—"near" or "far." In our case, using the far distance solution would lead to an increase in the estimated masses for the central objects in both sources by a factor of five, making these masses much less plausible. The uncertainties in both the near and far distance estimates are due to the uncertainty in the velocity of the molecular cloud relative to the Local Standard of Rest. Zinchenko *et al*. [21] obtained the value −43.69 km/s for the velocity of the molecular cloud via Gaussian fitting of the CO line profile toward G328.24–0.54. At the same time, this velocity, −43.69 km/s, corresponds to a near distance of 2.8 kpc if we use the values of the constants presented by Brand and Blitz [31], rather than a distance of 2.9 kpc [10]. Although Brand and Blitz [31] did

not use southern-hemisphere HII regions in their approximations, they did use such data when calculating the distances to southern-hemisphere objects. We accordingly adopted 2.8 kpc as the near distance to the sources. Given the peculiar nature of the velocity along the line of sight and the deviations of the real physical pattern for the spiral arm containing the molecular cloud from the model for this pattern described by the adopted constants, an uncertainty in the velocity of 10 km/s leads to an uncertainty in the distance of 0.5 kpc, i.e., by less than 20%.

Phillips *et al.* [4] also used the constants of Brand and Blitz [31] to estimate the near kinematic distance to these sources, obtaining 3.0 kpc for G328.236–0.547 and 2.6 kpc for G328.254–0.532. The exact velocity values used to derive these kinematic distances are not presented in [4]; it may be that the mean values over velocity intervals for the maser features, which are different for the northern and southern source, were adopted, leading to the two different kinematic distances. However, we assume here that the north–south velocity difference is associated with orbital motions about protostars and not with differential rotation of the Galaxy. Therefore, in our case, we should use the same distance for both sources, for example, by adopting the average of the two values derived by Phillips *et al.* [4], which coincides with the value of 2.8 kpc that we obtained based on the CO line velocities. The spread of these distance estimates suggests that the uncertainty in the distance is approximately 0.1 kpc, which corresponds to an uncertainty in the mass of about 5%.

Caswell *et al.* [13] present a near kinematic distance of 3.1 kpc for both sources. Note that these authors present arguments suggesting that this region may be located at the far kinematic distance: the HII zone associated with these sources is not visible in the optical, suggesting that its radiation is strongly absorbed. At the same time, if these masers were very distant, their luminosities would be extremely high.

6.2. Coordinates and Positions of the Masers from Single-Dish Observations

The determination of the coordinates of a source from observations obtained using a single antenna requires mapping at several points relative to the pointing coordinates in order to find the response maximum. This requires additional observation time, which, as a rule, is not regularly included in large surveys. For this reason, the accuracy of the coordinates for such survey observations is usually no better than half a beamwidth. The most accurate of the data we have used are the SEST coordinates of the thermal SiO lines, while the least accurate are the H_2O maser coordinates. These uncertainties do not influence the mass estimates, but the overall pattern of the distribution of peculiar sources in the star-forming region could be different than we have supposed. For example, as we noted above, the IRAS source could, in principle, belong to the southern and not the northern source, as is currently believed (Fig. 1). This could, in turn, affect our understanding of the evolutionary status of the sources, and even the mechanisms for pumping of the masers.

6.3. Distances between the Maser Components Derived Using VLBI

We used ATCA data to derive our estimates of the protostar masses, for which the accuracy in the relative positions of the 6.7 GHz maser features is no worse than 0.01″ for spectral features brighter than 50 Jy [2]. Such uncertainties lead to uncertainties in the masses of about 1–2%. However, this uncertainty is about a factor of 10 larger for weaker features. Since we have used the fairly weak components (A) and (B) in the southern source in our analysis, we will take the uncertainty in the maser component separations to be 0.1″, which contributes an uncertainty in the masses of about 15%.

6.4. Orbital Velocities of the Protoplanets

The uncertainty in the central velocity of a maser feature in the spectrum, i.e., the velocity of one of the protoplanets in its orbit, depends on the brightness and width of the feature. However, all the spectral features we have considered have brightnesses of more than 5 Jy, which is sufficient to provide an accuracy in the line velocity based on Gaussian fitting of the line profile of no worse than 10% of the line width (<1 km/s for maser lines, or 0.1 km/s). The velocities of the methanol features derived from the Gaussian profile fitting are not published, but we estimate the uncertainty in our determinations of the positions of the line peaks to be 0.1 km/s. The velocities of the peaks of the thermal lines we used to estimate the velocities of the protostars are determined with comparable accuracy. These uncertainties contribute an uncertainty in the mass of no more than 5%.

Thus, including all the above sources of uncertainty, the overall relative uncertainty in the mass estimates is about 25%.

7. DISCUSSION AND CONCLUSION

We believe that the N and S methanol masers in the region G328.2–0.5 are associated with two protoplanetary systems. In the center of each system, there is a protostar surrounded by a gas–dust cocoon that radiates thermal methanol line emission. The system

of two protostars should not be considered a binary: they are separated by a distance of slightly more than 1 pc, which is about equal to the distance between the Sun and Proxima Centauri.

Interferometric measurements of the relative spatial arrangement of the spectral components do not rule out the possibility that the motions of some of the maser components in both the northern and southern sources are Keplerian. Assuming the velocities of the class II methanol masers at 6.7 GHz are Keplerian and adopting the velocity of the thermal lines as the velocity of a central object surrounded by a Keplerian disk in which the maser's orbit yields masses for the protostars of $M_S = 13 \pm 4M_\odot$ (disk size 2044 AU) and $M_N = 38 \pm 10M_\odot$ (disk size 2408 AU).

Our mass for the northern protostar coincides within the errors with the value obtained in [4] based on the presence of velocity gradients assumed to be in a disk ($M_S = 35.5M_\odot$ with a disk size of 2080 AU). Our mass for the southern protostar is about half the value obtained in [4] ($M_S = 33.8M_\odot$ with a disk size of 2400 AU).

Thus, observations of molecular maser lines, which can be interpreted as being associated with protoplanets moving with Keplerian velocities, can be used together with observations of thermal lines of these molecules, which most likely form in a molecular cocoon surrounding the protostar and whose velocities correspond to the protostar velocity, to determine the protostar mass. A joint analysis of the maser and thermal velocities can potentially appreciably influence the resulting estimate for the protostar mass.

ACKNOWLEDGMENTS

The authors thank V.I. Slysh for useful discussions. This work was carried out as part of the preparation of a program of observations of maser sources in star-forming regions on the Kalyazin Radio Telescope, and was partially financially supported by the Russian Foundation for Basic Research (project no. 01-02-17057), the CRDF (grant no. RP1-2392-MO-02), and the Basic Research Program of the Physical Sciences Section of the Russian Academy of Sciences "Extended Objects in the Universe."

REFERENCES

1. C. R. O'Dell, Zheng Wen, and Xihai Hu, Astrophys. J. **410**, 696 (1993).
2. R. P. Norris, J. B. Whiteoak, J. L. Caswell, *et al.*, Astrophys. J. **412**, 222 (1993).
3. R. P. Norris, S. E. Byleveld, P. J. Diamond, *et al.*, Astrophys. J. **508**, 275 (1998).
4. C. J. Phillips, R. P. Norris, S. P. Ellingsen, *et al.*, Mon. Not. R. Astron. Soc. **300**, 1131 (1998).
5. V. I. Slysh, I. E. Val'tts, V. Migenes, *et al.*, Astrophys. J. **526**, 236 (1999).
6. V. I. Slysh, I. E. Val'tts, S. V. Kalenskii, *et al.*, Astron. Zh. **76**, 751 (1999) [Astron. Rep. **43**, 657 (1999)].
7. V. Minier, R. S. Booth, and J. E. Conway, Astron. Astrophys. **362**, 1093 (2000).
8. V. Minier, J. E. Conway, and R. S. Booth, Astron. Astrophys. **369**, 278 (2001).
9. I. E. Val'tts and S. Yu. Lyubchenko, Astron. Zh. **79**, 328 (2002) [Astron. Rep. **46**, 293 (2002)].
10. J. L. Caswell, R. F. Haynes, and W. M. Goss, Aust. J. Phys. **33**, 639 (1980).
11. R. F. Haynes, J. L. Caswell, and L. W. J. Simons, Aust. J. Phys. Astrophys. Suppl., No. 45, 1 (1978).
12. B. J. Robinson, J. L. Caswell, and W. M. Goss, Aust. J. Phys. **27**, 575 (1974).
13. J. L. Caswell, R. A. Vaile, S. P. Ellingsen, *et al.*, Mon. Not. R. Astron. Soc. **272**, 96 (1995).
14. J. L. Caswell, R. A. Vaile, and J. R. Forster, Mon. Not. R. Astron. Soc. **277**, 210 (1995).
15. B. O. S. Wood and E. Churchwell, Astrophys. J. **340**, 265 (1989).
16. A. J. Walsh, A. R. Hyland, G. Robinson, *et al.*, Mon. Not. R. Astron. Soc. **291**, 261 (1997).
17. E. Scalise, Jr. and M. A. Braz, Astron. Astrophys. **85**, 149 (1980).
18. M. Juvela, Astron. Astrophys., Suppl. Ser. **118**, 191 (1996).
19. L. Bronfman, L. A. Nyman, and J. May, Astron. Astrophys., Suppl. Ser. **115**, 81 (1996).
20. F. F. Gardner and J. B. Whiteoak, Mon. Not. R. Astron. Soc. **210**, 23 (1984).
21. I. Zinchenko, C. Henkel, and R. Q. Mao, Astron. Astrophys. **361**, 1079 (2000).
22. J. Harju, K. Lehtinen, R. S. Booth, *et al.*, Astron. Astrophys., Suppl. Ser. **132**, 211 (1998).
23. J. L. Caswell, Yi. Jiyune, R. S. Booth, *et al.*, Mon. Not. R. Astron. Soc. **313**, 599 (2000).
24. J. L. Caswell, R. A. Vaile, S. P. Ellingsen, *et al.*, Mon. Not. R. Astron. Soc. **274**, 1126 (1995).
25. V. I. Slysh, S. V. Kalenskii, I. E. Val'tts, *et al.*, Mon. Not. R. Astron. Soc. **268**, 464 (1994).
26. I. E. Val'tts, S. P. Ellingsen, V. I. Slysh, *et al.*, Mon. Not. R. Astron. Soc. **317**, 315 (2000).
27. K. M. Menten, in *Astrophysical Masers*, Ed. by A. W. Clegg and G. E. Nedoluha; Lect. Notes Phys. **412**, 199 (1992).
28. I. E. Val'tts and S. Yu. Lyubchenko, Astron. Zh. **81**, 234 (2004) [Astron. Rep. **48**, 210 (2004)].
29. I. E. Val'tts, Astron. Zh. **76**, 189 (1999) [Astron. Rep. **43**, 157 (1999)].
30. I. E. Val'tts and G. M. Larionov, Astron. Zh. (2004) (in press).
31. J. Brand and L. Blitz, Astron. Astrophys. **275**, 67 (1993).
32. V. I. Slysh, M. A. Voronkov, I. E. Val'tts, *et al.*, Astron. Zh. **79**, 1074 (2002) [Astron. Rep. **46**, 969 (2002)].
33. J. L. Caswell, Mon. Not. R. Astron. Soc. **289**, 203 (1997).

Translated by D. Gabuzda

Astronomy Reports, Vol. 49, No. 4, 2005, pp. 327–336. Translated from Astronomicheskiĭ Zhurnal, Vol. 82, No. 4, 2005, pp. 368–377.

The Possible Escape of Electron Cyclotron Maser Radiation from Hot Stellar Coronas through a Window of Transparency

V. V. Zaĭtsev[1], V. E. Shaposhnikov[1], and H. O. Rucker[2]

[1] *Applied Physics Institute, Nizhni Novgorod, Russia*

[2] *Space Research Institute, Schmiedlstrasse 6, A-8042 Graz, Austria*

Received July 1, 2004; in final form, September 20, 2004

Abstract—The main argument against the idea that the intense radio emission observed from active regions on the Sun and flare stars is electron-cyclotron maser (ECM) radiation is that such radiation should be strongly absorbed in higher-lying layers where the condition for the cyclotron resonance at harmonics of the electron gyrofrequency is fulfilled. Cyclotron absorption lowers the efficiency of ECM radiation virtually to zero for a broad range of angles between the direction of propagation of the radiation and the magnetic field. Less severe absorption is possible only in narrow angular "windows" along (for ordinary and extraordinary waves) and perpendicular to (for ordinary waves) the magnetic field. However, the ECM radiation that is generated does not fall into these windows of transparency due to the kinematic conditions corresponding to coronal magnetic traps. We investigate the efficiency of induced scattering of ECM radiation on ions in the equilibrium plasma in the source. Under certain conditions, induced scattering leads to the formation of a condensate of ECM radiation with the direction of its wave vectors approximately along the magnetic field, enabling the escape of the radiation through windows of transparency. The most favorable conditions for this phenomenon are realized for ordinary waves. We estimate the optical depths of the sources of the ECM radiation to the scattering and the angular width of the condensate for ordinary and extraordinary waves for the cases of the flare radio emission of the star AD Leo and the sources of type I noise storms in the solar corona. In both cases, the polarization of the emergent radiation should correspond to the ordinary wave. © *2005 Pleiades Publishing, Inc.*

1. INTRODUCTION

It is well established that stars of virtually all spectral classes represented on the Hertzsprung–Russell diagram are sources of powerful radio emission (see, for example, the reviews [1–6] and the monograph [7]). Considerable interest is presented by flare stars, such as dMe stars, which make up a large fraction of the stars in and near our Galaxy. The radio emission of dMe stars resembles solar radio emission in many ways—it displays rapidly drifting flares, pulsations, a continuum, and so forth [6, 8, 9]—but has a higher brightness temperature. The brightness temperature can reach 10^{16} K in flares [1], which is four to five orders of magnitude higher than the most powerful solar radio flares [10]. Two mechanisms for the generation of the powerful, sporadic radio emission emerging from the corona are usually considered: (i) the generation of plasma waves by nonequilibrium populations of fast electrons, with subsequent transformation into electromagnetic radiation, and (ii) the electron-cyclotron maser (ECM) mechanism, which involves the direct generation of electromagnetic radiation by nonequilibrium electrons. The plasma mechanism as applied to solar radio emission has been studied in detail in [11–18] and a number of other works, and has been applied to the radio emission of late-type stars in [8, 9, 19]. The ECM mechanism is considered to be more efficient, since it supposes the direct amplification of electromagnetic waves at harmonics of the gyrofrequency, and can be realized for electrons with both anisotropic and isotropic velocity distributions [20–27].

The main problem with using the ECM mechanism to explain solar and stellar radio emission with high brightness temperatures is the expected strong absorption of the ECM radiation in higher-lying layers of the corona, where the cyclotron-resonance condition at harmonics of the electron gyrofrequency ω_{Be}, i.e., $\omega = s\omega_{Be}$, $s = 1, 2, 3, \ldots$, is satisfied. In other words, if ECM radiation is emitted in a source at frequency $\omega = \omega_{Be}$, this radiation will undergo gyroresonance absorption in other layers with weaker magnetic fields, in which the frequency of the radio emission coincides with twice, three times, and other multiples of the gyrofrequency. Estimates of the optical depth to gyroresonance absorption for radiation at 4.85 GHz propagating through the corona of the red dwarf AD Leo were obtained in [9] based on an analysis of the observational properties of the flare emission of the star. These estimates indicate

1063-7729/05/4904-0327$26.00

that ECM radiation leaving the corona of the star should be attenuated by a factor of $\exp(10^4)$ for the extraordinary wave and by a factor of $\exp(10^3)$ for the ordinary wave. At the same time, there exists a "window" for the ECM radiation with a width of several degrees along the magnetic field, through which this radiation can escape without being absorbed. In the case of the ordinary wave, there is also a window near an angle near $\pi/2$, also with a width of several degrees [9].

This raises the question of whether these windows could serve as channels for the escape of ECM radiation from hot stellar coronas. This would require that an appreciable fraction of the generated radiation be scattered within the source, such that it was concentrated near a window of transparency. This scattering must be induced, since only then is it possible to accumulate the optical depth required to transform the angular spectrum of the radiation. An induced nature for the scattering is also suggested by the relatively high intensities of the radiation arising during stellar flares.

We study here the induced scattering of ECM radiation on thermal particles in the main plasma, and demonstrate the possibility of forming condensates in the angular spectrum of the radiation near a window of transparency, enabling the escape of the ECM radiation from the source without appreciable cyclotron absorption. We consider results for various ratios of the plasma frequency ω_{Pe} to the electron gyrofrequency ω_{Be}, corresponding to the generation of extraordinary and ordinary waves when an ECM instability is realized in the radio source. We estimate the angular extent of the condensate and determine the type of wave that emerges from the source. We used the parameters of the coronal source in AD Leo at 4.85 GHz derived in [9] from observational data to carry out our estimates, as well as the characteristics of the sources of type I noise storms in the solar corona.

Section 2 presents the main characteristics of ECM radiation arising as a result of cyclotron instability of fast electrons with a transverse (relative to the magnetic field) anisotropy velocity distribution. Equations describing the induced scattering of ECM radiation on particles of the equilibrium plasma are presented together with their specific forms for the cases of interest to us. Section 3 presents an analysis of the angular dependence of the scattering probabilities for various ratios ω_{Pe}/ω_{Be}, and we determine the type of wave that is scattered and the width of the resulting angular "condensate" near a window of transparency. Our main conclusions are summarized in Section 4.

2. BASIC EQUATIONS

As a rule, the radio emission of solar and stellar flares arises in coronal magnetic traps. When fast electrons are injected into a trap, a nonequilibrium particle distribution with an anisotropic velocity distribution transverse to the magnetic field rapidly forms. This anisotropy is associated with the presence of a loss cone in the trap, which causes energetic electrons with small transverse velocities to enter the loss cone and thermalize as a result of collisions with particles of the main plasma at the footpoints of the trap. This gives rise to an excess of energetic electrons with high transverse velocities in the trap. Under appropriate conditions, the resulting transverse-velocity anisotropy brings about the direct amplification of electromagnetic waves due to the development of ECM instability [27–29]. ECM instability has been studied for various types of fast-particle distribution functions with a loss cone for a wide range of temperatures for the main plasma, $T = 10^6$–10^7 K, and various ratios $\omega_{Pe}/\omega_{Be} = 0.1$–$1.4$. If the magnetic field is sufficiently strong ($\omega_{Pe}/\omega_{Be} < 0.24$–$0.4$), the ECM generates predominantly extraordinary waves at the first harmonic of the gyrofrequency (more precisely, at a frequency slightly higher than ω_{Be}). In the interval of parameters 0.24–$0.4 < \omega_{Pe}/\omega_{Be} < 1$, ordinary waves are generated at the first harmonic of the gyrofrequency. The maximum increment is on the order of

$$\gamma_e \simeq 10^{-2}\frac{N_h}{N_0}\omega_{Be} \qquad (1)$$

for the extraordinary wave and

$$\gamma_o \simeq 2\times 10^{-3}\frac{N_h}{N_0}\omega_{Be} \qquad (2)$$

for the ordinary wave (here, N_h and N_0 are the densities of the hot electrons and of the cool main plasma, respectively). In both cases, the maximum increment is realized for waves propagating at an angle of $\theta_m \simeq 70^\circ$ to the magnetic field. The angular width of the spectrum of the excited waves is $\Delta\theta \simeq 3^\circ$. When $\omega_{Pe}/\omega_{Be} > 1$, the maximum increments are possessed by plasma waves at the upper hybrid frequency, $\omega \simeq \sqrt{\omega_{Pe}^2 + \omega_{Be}^2}$, while ECM radiation in the form of extraordinary waves at the frequency $\omega \simeq 2\omega_{Be}$ has an increment that is several orders of magnitude smaller, and does not contribute significantly to the flux of radio radiation from the traps.

The high power of the radiation emitted by active regions on the Sun and stars and the relatively small size of the corresponding sources suggest there is a high radiation-energy density in the generation region. This suggests that induced scattering processes may dominate, and that the source may have

a high optical depth to these processes. Under these conditions, the radiative-transfer equation describing induced scattering can be written

$$\frac{\partial W_\sigma(\mathbf{k})}{\partial t} = W_\sigma(\mathbf{k}) \int G_{\sigma\sigma'}(\mathbf{k}\mathbf{k}') W_{\sigma'}(\mathbf{k}') d\mathbf{k}', \quad (3)$$

where $G_{\sigma\sigma'}(\mathbf{k},\mathbf{k}')$ is the coefficient for scattering a wave σ' with wave vector $\mathbf{k}'$ and spectral density $W_{\sigma'}(\mathbf{k}')$ into a wave σ with wave vector $\mathbf{k}$ and spectral density $W_\sigma(\mathbf{k})$, described by the expression [30, 31]

$$G_{\sigma\sigma'}(\mathbf{k},\mathbf{k}') = \frac{\omega}{\omega'} G_{\sigma'\sigma}(\mathbf{k}',\mathbf{k}) = \frac{8\pi e^2\kappa^2}{m_e^2\omega^2\omega'} |\chi|^2 \quad (4)$$
$$\times \left[\frac{\partial\omega^2 D(\omega,\mathbf{k})}{\omega\partial\omega}\right]^{-1}_{\omega=\omega_\sigma(\mathbf{k})} \left[\frac{\partial\omega^2 D(\omega,\mathbf{k})}{\omega\partial\omega}\right]^{-1}_{\omega=\omega'_{\sigma}(\mathbf{k}')}$$
$$\times \left(\left|\frac{1+\delta\epsilon_i(\Omega,\boldsymbol{\kappa})}{\epsilon_l(\Omega,\boldsymbol{\kappa})}\right|^2 \Im m\delta\epsilon_e(\Omega,\boldsymbol{\kappa}) + \left|\frac{\delta\epsilon_e(\Omega,\boldsymbol{\kappa})}{\epsilon_l(\Omega,\boldsymbol{\kappa})}\right|^2 \Im m\delta\epsilon_i(\Omega,\boldsymbol{\kappa}) \right).$$

Here, $\Omega = \omega - \omega'$, $\boldsymbol{\kappa} = \mathbf{k} - \mathbf{k}'$, $\delta\epsilon_{e,i}(\Omega,\boldsymbol{\kappa})$ are the electron (e) and ion (i) parts of the longitudinal component of the dielectric constant $\epsilon_l(\Omega,\boldsymbol{\kappa}) = 1 + \delta\epsilon_e(\Omega,\boldsymbol{\kappa}) + \delta\epsilon_i(\Omega,\boldsymbol{\kappa})$, written as a function of the differences of the frequency Ω and of the wave vector $\boldsymbol{\kappa}$, e and m_e are the charge and mass of the electron,

$$D(\omega,\mathbf{k}) = a_i^* \epsilon_{ij}(\omega,\mathbf{k}) a_j + \frac{c^2}{\omega^2} (\mathbf{ka})(\mathbf{ka}^*), \quad (5)$$

$\epsilon_{ij}(\omega,\mathbf{k})$ is the dielectric tensor of the equilibrium plasma, which is a function of the frequency ω and the wave vector $\mathbf{k}$, $\mathbf{a}$ is the polarization vector of the interacting wave, and $\sigma = x, o$, (x and o are the extraordinary and ordinary modes).

We can see from (4) that the scattering coefficient depends substantially on the type of interacting wave, and also on the conditions under which this interaction occurs. The character of the interacting wave is taken into account by the polarization and dispersion factors [32]:

$$|\chi|^2 = \frac{1+u}{2(1-u)^2}\left\{(1+a_\sigma a_{\sigma'})^2 + (a_\sigma + a_{\sigma'}^2)\right\} \quad (6)$$
$$+ \frac{2\sqrt{u}}{(1-u)^2}(1+a_\sigma a_{\sigma'})(a_\sigma + a_{\sigma'}) + (b_\sigma b_{\sigma'})^2,$$

$$\left[\frac{\partial\omega^2 D(\omega,\mathbf{k})}{\omega\partial\omega}\right]^{-1}_{\omega=\omega_\sigma(\mathbf{k})} = \frac{1+K_\sigma^2+\Gamma_\sigma^2}{(1+K_\sigma^2)\left(\dfrac{\partial\omega^2 n_\sigma^2}{\omega\partial\omega}\right)}, \quad (7)$$

where $a_\sigma = K_\sigma\cos\theta - \Gamma_\sigma\sin\theta$, $b_\sigma = -K_\sigma\sin\theta - \Gamma_\sigma\cos\theta$,

$$n_\sigma \frac{\partial(\omega n_\sigma)}{\partial\omega} = 1 + \frac{v\sqrt{u}\cos\theta K_\sigma}{2(K_\sigma - \sqrt{u}\cos\theta)^2} \quad (8)$$
$$\times \left(1 + \frac{(1+v)(1-K_\sigma^2)}{(1-v)(1+K_\sigma^2)}\right),$$

n_σ is the index of refraction of the electromagnetic wave, K_σ and Γ_σ are the polarization coefficients of the electromagnetic wave in a coordinate system with the z axis along the wave vector $\mathbf{k}$, and θ is the angle between the magnetic field and the wave vector of the interacting wave. According to [33],

$$K_\sigma = \frac{\sqrt{u}(1-v)\cos\theta}{0,5u\sin^2\theta \mp \sqrt{u^2\sin^4\theta + 4u(1-v)^2\cos^2\theta}}, \quad (9)$$

$$\Gamma_\sigma = -\frac{v\sqrt{u}\sin\theta + K_\sigma uv\sin\theta\cos\theta}{1-u-v+uv\cos^2\theta}, \quad (10)$$

where $u = \omega_{\mathrm{Be}}^2/\omega^2$, $v = \omega_{\mathrm{Pe}}^2/\omega^2$, and ω_{Be} and ω_{Pe} are the electron gyrofrequency and plasma frequency.

During the scattering of waves on particles in a magnetoactive plasma with an equilibrium distribution function, the influence of the magnetic field on the particle motions can be neglected (the particles are not magnetized) if [33]

$$\frac{\kappa_\perp v_{\mathrm{T}\alpha}}{\omega_{\mathrm{B}\alpha}} \gg 1, \quad (11)$$

where $\kappa_\perp$ is the component of the difference vector $\boldsymbol{\kappa}$ perpendicular to the magnetic field. In this approximation for $\delta\epsilon_\alpha(\Omega,\boldsymbol{\kappa})$ and $\Im m\delta\epsilon_\alpha(\Omega,\boldsymbol{\kappa})$ ($\alpha = e, i$), we can use the expressions obtained for an isotropic plasma. According to [33],

$$\delta\epsilon_\alpha(\Omega,\boldsymbol{\kappa}) = \frac{\omega_{\mathrm{P}\alpha}^2}{\kappa^2 v_{\mathrm{T}\alpha}^2}\left(1 + \imath\sqrt{\pi} Z_\alpha W(Z_\alpha)\right), \quad (12)$$

$$\Im m\delta\epsilon_\alpha(\Omega,\boldsymbol{\kappa}) = \sqrt{\pi}\frac{\omega_{\mathrm{P}\alpha}^2}{\kappa^2 v_{\mathrm{T}\alpha}^2} Z_\alpha \exp\left(-Z_\alpha^2\right), \quad (13)$$

where $\omega_{\mathrm{P}\alpha}^2 = 4\pi e^2 N_o/m_\alpha$, $Z_\alpha = \Omega/\sqrt{2}\kappa v_{\mathrm{T}\alpha}$, and $W(Z_\alpha)$ is the Cramp function.

When the inequality (11) is violated, the magnetic field must be taken into account (the particles are magnetized), and the expressions for $\delta\epsilon_\alpha(\Omega,\boldsymbol{\kappa})$ and $\Im m\delta\epsilon_\alpha(\Omega,\boldsymbol{\kappa})$ have the form

$$\delta\epsilon_\alpha(\Omega,\boldsymbol{\kappa}) = \frac{\omega_{\mathrm{P}\alpha}^2}{\kappa^2 v_{\mathrm{T}\alpha}^2} \quad (14)$$
$$\times \left[1 + \imath\sqrt{\pi} Z_{\alpha,o} \sum_{s=-\infty}^{+\infty} W(Z_{\alpha,s}) I_s(\chi_\alpha)\exp(-\chi_\alpha)\right],$$

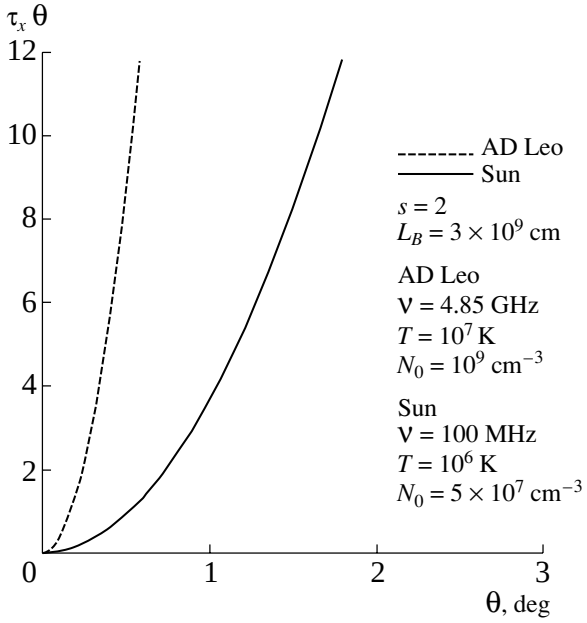

Fig. 1. Dependence of the optical depth to cyclotron absorption in a layer with $s = 2$ on the angle between the magnetic field and the wave vector for the extraordinary wave for the sources in the corona of the red dwarf AD Leo and in the solar corona. The width of the window of transparency in which $\tau_x \lesssim 1$ is $\Delta\theta_w \lesssim 0.15°$ for the corona of AD Leo and $\Delta\theta_w \lesssim 0.25°$ for the corona of the Sun.

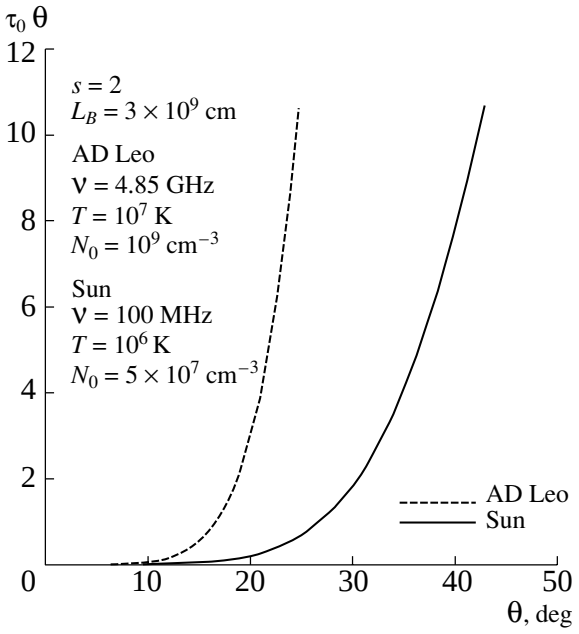

Fig. 2. Same as Fig. 1 for the ordinary wave. The width of the window of transparency is $\Delta\theta_w \lesssim 15°$ for the corona of AD Leo and $\Delta\theta_w \lesssim 25°$ for the corona of the Sun.

$$\Im m\delta\epsilon_\alpha(\Omega,\boldsymbol{\kappa}) = \sqrt{\pi}\frac{\omega_{Pe}^2}{\kappa^2 v_{T\alpha}^2} Z_{\alpha,o} \qquad (15)$$
$$\times \exp(-Z_{\alpha,s}^2) I_o(\chi_\alpha)\exp(-\chi_\alpha),$$

where $Z_{\alpha,s} = (\Omega - s\omega_{B\alpha})/\sqrt{2}\kappa_{||}v_{T\alpha}$, $\chi_\alpha = \kappa_\perp^2 v_{Te}^2/\omega_{Be}^2$, $I_s(\chi_\alpha)$ is a modified Bessel function, and $\kappa_\perp$ is the component of the difference vector $\boldsymbol{\kappa}$ perpendicular to the magnetic field.

Expression (4) for the scattering coefficient $G_{\sigma,\sigma'}(\mathbf{k},\mathbf{k}')$ is a sum of two terms due to scattering on electrons (the first term) and ions (the second term), whose contributions to $G_{\sigma\sigma'}(\mathbf{k},\mathbf{k}')$ depend on the ratio of the coefficients $|(1+\delta\epsilon_i)/\epsilon_l|^2$ and $|\delta\epsilon_e/\epsilon_l|^2$ of the imaginary parts of the corresponding dielectric tensors.

Let us consider two limiting cases of (4) for the scattering coefficient. The first case corresponds to the conditions

$$Z_i = \frac{\omega-\omega'}{\sqrt{2}|\mathbf{k}-\mathbf{k}'|v_{Ti}} \lesssim 1, \qquad (16)$$

$$Z_e = \frac{\omega-\omega'}{\sqrt{2}|\mathbf{k}-\mathbf{k}'|v_{Te}} \ll 1, \qquad (17)$$

when the main contribution to the scattering is made by ions. In this case,

$$G_{\sigma\sigma'}(\mathbf{k},\mathbf{k}') = \frac{8\pi e^2}{m_e^2\omega\omega'}\frac{\sqrt{\pi}\omega_{Pi}^2}{v_{Ti}^2} \qquad (18)$$
$$\times \left(1+\frac{T_e}{T_i}\right)^{-2} \Psi_{\sigma\sigma'}(\theta,\theta') Z_i e^{-Z_i^2},$$

where

$$\Psi_{\sigma\sigma'}(\theta,\theta') = |\chi|^2 \left[\frac{\partial\omega^2 D(\omega,\mathbf{k})}{\omega\partial\omega}\right]^{-1}_{\omega=\omega_\sigma(\mathbf{k})} \qquad (19)$$
$$\times \left[\frac{\partial\omega^2 D(\omega,\mathbf{k})}{\omega\partial\omega}\right]^{-1}_{\omega=\omega'_\sigma(\mathbf{k}')}$$

is a function determining the angular pattern of the induced scattering.

If $Z_i \gg 1$, $Z_e \lesssim 1$, the main contribution to the scattering is made by electrons, and

$$G_{\sigma\sigma'}(\mathbf{k},\mathbf{k}') = \frac{8\pi e^2}{m_e^2\omega\omega'}\frac{\sqrt{\pi}\kappa^4 v_{Te}^2}{\omega_{Pe}^2}\Psi_{\sigma\sigma'}(\theta,\theta') Z_e e^{-Z_e^2}. \qquad (20)$$

Formulas (18) and (20) are valid for scattering on nonmagnetized particles, when condition (11) holds. In the case of scattering on magnetized particles, when the inequality

$$\frac{\kappa_\perp v_{T\alpha}}{\omega_{B\alpha}} \lesssim 1 \qquad (21)$$

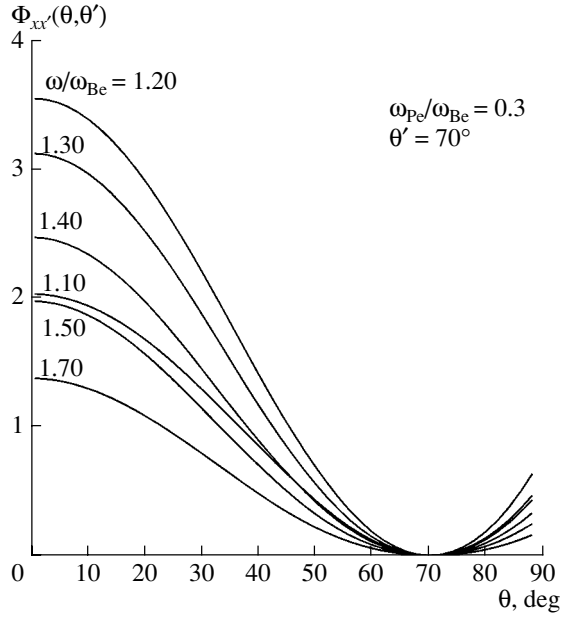

Fig. 3. Dependence of the probability of induced scattering of an extraordinary wave into an extraordinary wave $\Phi_{xx'}(\theta,\theta')$ on the angle θ between the wave vector of the scattered wave and the magnetic field for $\theta' = 70°$ and various frequencies.

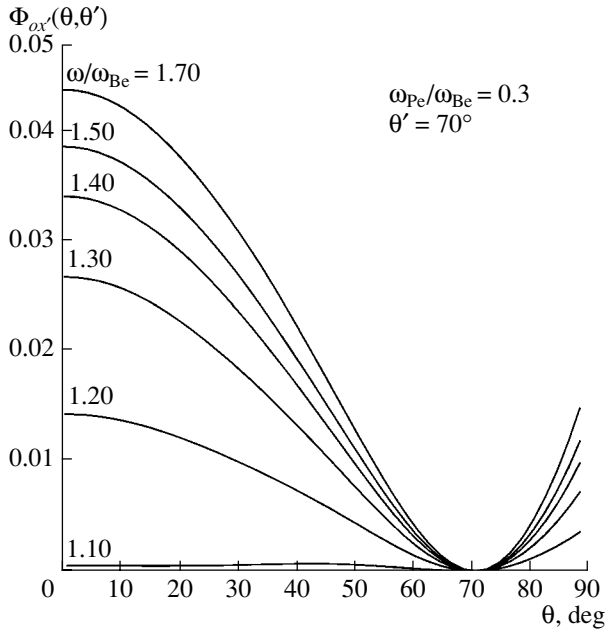

Fig. 4. Same as Fig. 3 for the probability of induced scattering of an extraordinary wave into an ordinary wave $\Phi_{ox'}(\theta,\theta')$.

holds, $Z_\alpha = \dfrac{\Omega}{\sqrt{2}\kappa v_{T\alpha}}$ in (18) and (20) must be replaced by $Z_\alpha = \dfrac{\Omega}{\sqrt{2}\kappa_{||} v_{T\alpha}} = \dfrac{\omega(\mathbf{k}) - \omega(\mathbf{k}')}{\sqrt{2}|k_{||} - k'_{||}| v_{T\alpha}}$.

3. SCATTERING OF ECM RADIATION INTO A WINDOW OF TRANSPARENCY

As we noted in the Introduction, cyclotron absorption as the radiation propagates through regions with weaker magnetic fields where $\omega = s\omega_{Be}$ ($s = 2, 3, 4\ldots$) leads to strong attenuation of the radio emission, with the dominant contribution being made by absorption at the second harmonic of the gyrofrequency, $s = 2$. Figure 1 shows the optical depth τ_x to gyroresonance absorption of extraordinary waves at the second harmonic of the gyrofrequency, $s = 2$, in the corona of the star AD Leo and in the solar corona as a function of the angle θ between the wave vectors of the extraordinary and ordinary waves and the magnetic field [9]. The plasma is assumed to be Maxwellian, with $T = 10^7$ K and density $N_0 = 10^9$ cm^{-3} in the corona of AD Leo and $T = 10^6$ K and $N_0 = 5 \times 10^7$ cm^{-3} in the solar corona. The characteristic scale for variations of the magnetic field in the source of radio emission (a coronal magnetic arch) was taken to be $L_B = 3 \times 10^9$ cm in both cases. Figure 2 presents the analogous dependence of the optical depth to gyroresonance absorption for the ordinary wave for $s = 2$. It follows from Figs. 1 and 2, and also from the detailed computations of [8, 19] for realistic coronal temperatures ($T \sim (0.3{-}3) \times 10^7$ K) and densities ($n \sim 10^9{-}10^{11}$ cm^{-3}) for dMe stars, that there is only one narrow window along the magnetic field for the extraordinary wave, with width $\Delta\theta_w \lesssim 0.2°$ for the corona of AD Leo and $\Delta\theta_w \lesssim 0.5°$ for the solar corona. The window of transparency along the magnetic field is appreciably broader for the ordinary wave, with widths of $\Delta\theta_w \lesssim 15°$ for the corona of AD Leo and $\Delta\theta_w \lesssim 25°$ for the corona of the Sun. In addition, there is another window of transparency for the ordinary wave with a width of a fraction of a degree near the orthogonal direction of propagation, however, we will see below that this window does not play a significant role in the escape of radiation from the source. The ECM radiation is generated at an angle of $\theta \simeq 70°$ to the magnetic field in a narrow cone with width $\Delta\theta \simeq 3°$ [27], so that propagation of the radiation without appreciable attenuation is possible only if the scattering concentrates a substantial fraction of the radiation in the windows of transparency.

3.1. Scattering of the Extraordinary Wave

If the plasma in the radio source is sufficiently rarified ($\omega_{Pe}/\omega_{Be} < 0.2{-}0.4$), the ECM mechanism generates primarily extraordinary waves [27]. The frequency spectrum of the radiation is fairly narrow.

When $\omega_{Pe}/\omega_{Be} \simeq 0.1$, the relative width of the spectrum is $\Delta\omega/\omega \simeq 3 \times 10^{-2}$, with its maximum at $\omega_m \simeq 1.03\omega_{Be}$ [27], which corresponds to the wave vector $k_m \simeq 0.5\omega_{Be}/c$. Scattering on magnetized ions dominates in the temperature interval $T \simeq 10^6$–10^7 K. This scattering is differential in frequency, since the width of the core of the integral equation (3) is smaller than the width of the frequency spectrum of the excited electromagnetic waves; i.e., $|k_{||} - k'_{||}|v_{Ti} \ll \Delta\omega$. The scattering is integral in angle, i.e., the direction of the wave vector $\mathbf{k}$ can be appreciably changed in a single scattering act. Taking into account the differential character of the scattering in frequency and the small angular width of the excited spectrum, Eq. (3) can be written in the form

$$\frac{\partial W_{\mathbf{k}}}{\partial t} = \frac{\sqrt{8\pi e}\omega_{Pe}^4 v_{Ti}}{\omega_{Be}^3 N_0 \kappa_B T_i}\left(1+\frac{T_e}{T_i}\right)^{-2} \times \Psi_{\sigma\sigma'}(\theta,\theta')(k')^2\left(\frac{k}{k'}\cos\theta - \cos\theta'\right)^2 W_{\mathbf{k}}\frac{\partial W_{k'}}{\partial\omega}, \quad (22)$$

where κ_B is Boltzmann's constant. $W_{k'}$ is related to the energy density of the excited waves by the expression

$$W' = \int (k')^2 W_{k'} dk', \quad (23)$$

and by θ and θ', which are the angles between the magnetic field and the wave vectors of the wave after and before scattering; $e \simeq 2.7$. The dependence of the function

$$\Phi_{\sigma\sigma'}(\theta,\theta') = \Psi_{\sigma\sigma'}(\theta,\theta')\left(\frac{k}{k'}\cos\theta - \cos\theta'\right)^2 \quad (24)$$

on θ with $k = k'$ is presented in Figs. 3 and 4. Figure 3 corresponds to the scattering of an extraordinary wave into an extraordinary wave $\Phi_{xx'}(\theta,\theta')$ for the case $\omega_{Pe}/\omega_{Be} = 0, 3$, $\theta' = 70°$ for various values of ω/ω_{Be}. Figure 4 corresponds to the scattering of an extraordinary wave into an ordinary wave $\Phi_{ox'}(\theta,\theta')$ for the same parameters. A comparison of these two figures shows that the increment for scattering an extraordinary wave into an extraordinary wave is approximately two orders of magnitude greater than that for scattering into an ordinary wave. Therefore, extraordinary waves will dominate in the spectrum of the scattered waves. In addition, it follows from the form of (22) and Fig. 3 that the scattering probability grows as the angle θ between the wave vector of the scattered wave and the magnetic field decreases. This means that, if the optical depth of the source to the process $x' \to x$ is sufficiently high, a narrow condensate of scattered extraordinary waves will arise along the magnetic field, which will propagate through the window of transparency along the magnetic field.

The appearance of this condensate is associated with the angular dependence in the argument of the exponential in the case of an exponential growth in the energy density of the scattered waves, described by (22). We obtain from (22) an estimate of the increment of the scattered radiation:

$$\gamma_{xx'} = \sqrt{8\pi e}\omega_{Pe}\frac{\omega_{Pe}^3}{\omega_{Be}^3}\left(1+\frac{T_e}{T_i}\right)^{-2} \times \frac{W'}{N_0\kappa_B T_i}\frac{k'_*}{\Delta k'}\frac{k'_* v_{Ti}}{\Delta\omega'}\Phi_{xx'}(\theta,\theta'). \quad (25)$$

Here, k'_* and $\Delta k'$ are the characteristic values of the wave number and the width of the spectrum generated in the source of ECM radiation and $\Delta\omega'$ is the frequency width of the radiation spectrum.

Since the magnetic field in the source is inhomogeneous and has a variation scale L_B and the frequency of the radiation is close to ω_{Be}, a wave of a specified frequency ω will interact with the excited waves until ω_{Be} is shifted by an amount of the order of the width $\Delta\omega'$ of the spectrum of the excited waves. Therefore, we can adopt

$$\Delta x = \frac{\Delta\omega'}{\omega'}L_B \quad (26)$$

as the effective length of the region in which waves of a specified frequency ω' are scattered. The optical depth of the region with length Δx to induced scattering will be

$$\tau_{xx'} = \frac{\gamma_{xx'}\Delta x'}{v_{gr}(\omega,\theta)} \simeq \frac{\gamma_{xx'}\Delta\omega' L_B}{\omega' v_{gr}(\omega,\theta)}, \quad (27)$$

where $v_{gr}(\omega,\theta)$ is the group velocity for the extraordinary wave for frequencies corresponding to the maximum of the spectrum of the excited waves. Assuming $k \simeq k'_*$, $\cos\theta' \simeq 70°$, $\Delta k' \simeq 0.5k'_*$, and $T_e \simeq T_i \simeq T$, we obtain for the optical depth

$$\tau_{xx'} \simeq 4\frac{\omega_{Pe}^3}{\omega_{Be}^3}\frac{v_{Ti}}{c}\frac{\omega_{Pe}L_B}{v_{gr}(\omega,\theta)}\Phi_{xx'}(\theta,70°)\frac{W'}{N_0\kappa_B T}. \quad (28)$$

We can see from (28) that the optical depth to induced scattering depends on the energy density of the electromagnetic waves excited by the ECM mechanism. This energy density is determined both by the efficiency of the induced scattering causing the generated waves to go out of resonance with the fast particles responsible for the ECM instability, and by quasilinear effects that lead to deformations of the fast-particle distribution function and tend to suppress the instability. Our analysis shows that these quasilinear effects are more important in our case. In the case of ECM radiation, such quasilinear effects lead to an energy density for the electromagnetic waves in the source

$$W' \simeq 5 \times 10^{-3} N_h \kappa_B T_h, \quad (29)$$

which is virtually independent of the magnitude of ω_{Pe}/ω_{Be}, the "temperature" of the radiating particles T_h, and the degree of anisotropy of the fast-particle distribution function in terms of the particle velocities perpendicular to the magnetic field [27].

3.1.1. The Corona of AD Leo. Let us estimate the optical depth to induced scattering for the corona of the star AD Leo, under the assumption that the observed flare radio emission at 4.85 GHz [9] corresponds to the extraordinary wave of an ECM instability. Setting in this case $\omega \simeq \omega_{Be}$, we find for a frequency of 4.85 GHz a magnetic field in the radio source of $B \simeq 1700$ G, which is consistent with the measured photospheric magnetic field of AD Leo [34]. The required condition for excitation of the extraordinary wave provides an upper limit for the plasma density in the source: $\omega_{Pe}/\omega_{Be} \lesssim 0.3$, whence we obtain $N_0 \lesssim 3 \times 10^{10}$ cm^{-3}. Following the analysis of [9], we will assume that the temperature of the source plasma for AD Leo is $T \simeq 10^7$ K, the scale for inhomogeneity of the magnetic field is $L_B \simeq 3 \times 10^9$ cm, and the temperature of the fast particles is $T_h \simeq 3 \times 10^8$ K. In accordance with Fig. 3 for $\omega_{Pe}/\omega_{Be} = 0.3$ and $\omega/\omega_{Be} \lesssim 1.1$, we can set $\Phi_{ee'}(/\theta, \theta') \lesssim 2$. For the indicated values of ω_{Pe}/ω_{Be} and quasilongitudinal propagation, $v_{gr}/ \lesssim 0.7c$. This yields the estimate of the optical depth to induced scattering

$$\tau_{xx'} \simeq 1.6 \times 10^6 \frac{N_h}{N_0}(\cos\theta - \cos\theta')^2. \qquad (30)$$

The angular spectrum of the scattered radiation escaping from the layer will have the form

$$W_{\mathbf{k}(\theta)} \simeq W^0_{\mathbf{k}} e^{\tau_{xx'}(\theta)}, \qquad (31)$$

where $W^0_{\mathbf{k}}$ is the spectral energy density of the waves upon their entry to the layer with length Δx. It follows from (30) that, if the density of fast particles in the source satisfies the condition $N_h/N_0 \gg 6 \times 10^{-7}$, the optical depth is high, and, when they emerge from the amplification region, the extraordinary waves will be concentrated in a narrow angular cone along the magnetic field, in the direction of the window of transparency for the extraordinary waves. The angular width of the resulting condensate is

$$\Delta\theta \simeq 3.8 \times 10^{-2} \left(\frac{N_h}{N_0}\right)^{1/2} \text{deg}. \qquad (32)$$

For example, when $N_0/N_h \simeq 10^{-4}$, we have $\Delta\theta \simeq 3.8$ deg. Since the angular width of the window in which the optical depth is less than unity for extraordinary waves is approximately $\Delta\theta_w \simeq 0.2°$ (Fig. 1), only a very small fraction of the scattered radiation (of the order of $(\Delta\theta_w/\Delta\theta)^2 \simeq 2 \times 10^{-3}$) can escape from the source in the form of extraordinary waves. The remaining radiation will be absorbed as it passes through the gyroresonance level $s = 2$.

3.1.2. The Solar Corona. One of the types of sporadic radio emission of the Sun that could be produced by the ECM mechanism are so-called type I noise storms. The radio emission of noise storms displays a high degree of circular polarization, long durations (up to several hours), a high brightness temperature, and a burstlike character. As a rule, the sources of type I noise storms are located near sunspots [10]. If we suppose that the emission associated with these noise storms arises at $\omega \simeq \omega_{Be}$, a characteristic frequency of $\nu = 100$ MHz corresponds to a source magnetic field of $B \simeq 36$ G. If $\omega_{Pe}/\omega_{Be} \lesssim 0.3$, we obtain a plasma density in the radio source of $N_0 \lesssim 1.2 \times 10^7$ cm^{-3}. Assuming the temperature of the plasma in the solar corona is $T \simeq 10^6$ K, the temperature of the hot particles is $T_h \simeq 3 \times 10^8$ K, and the scale for inhomogeneity in the source magnetic field is $L_B \simeq 3 \times 10^9$ cm (of the order of a sunspot diameter), we obtain for the optical depth in the solar corona using (30) and (32)

$$\tau_{xx'} \simeq 10^5 \frac{N_h}{N_0}(\cos\theta - \cos\theta')^2, \qquad (33)$$

and for the width of the angular spectrum of the extraordinary waves in the condensate that arises along the magnetic field as a result of the induced scattering

$$\Delta\theta \simeq 1.5 \times 10^{-1} \left(\frac{N_0}{N_h}\right)^{1/2} \text{deg}, \qquad (34)$$

which, for $N_h/N_0 = 10^{-4}$, gives an angular width of $\Delta\theta \simeq 5°$. As is shown in Fig. 2, which presents the angular dependence of the optical depth to gyroresonance absorption for $s = 2$ (gyroresonance absorption is appreciably lower for $s = 3$), the width of the window of transparency (in which $\tau < 1$) is $\Delta\theta_w \simeq 0.5°$. In this case, the transmission coefficient of the window for extraordinary radiation is $(\Delta\theta_w/\Delta\theta)^2 \simeq 2.5 \times 10^{-3}$; i.e., we obtain a value that is similar to the value for the corona of AD Leo.

3.2. Scattering of the Ordinary Wave

The induced scattering of an ordinary wave into an ordinary ($o' \to o$) or extraordinary ($o' \to x$) wave is also described by (22) if $\Psi_{\sigma\sigma'}(\theta, \theta')$ is replaced by $\Psi_{oo'}(\theta, \theta')$ or $\Psi_{xo'}(\theta, \theta')$, respectively, and we take the spectrum of the excited ordinary waves for $W_{\mathbf{k}'}$. The angular spectrum of the scattered radiation will be

$$W_{\mathbf{k}}(\theta) \simeq W^0_{\mathbf{k}} e^{\tau_{\sigma o'}(\theta)}, \qquad (35)$$

where

$$\tau_{\sigma o'} \simeq 2 \times 10^{-2} \frac{N_h T_h}{N_0 T} \frac{\omega^4_{Pe}}{\omega^4_{Be}} \frac{v_{Ti}}{c} \frac{\omega_{Be} L_B}{v_{gr}(\omega, \theta)} \Phi_{o\sigma}(\theta), \qquad (36)$$

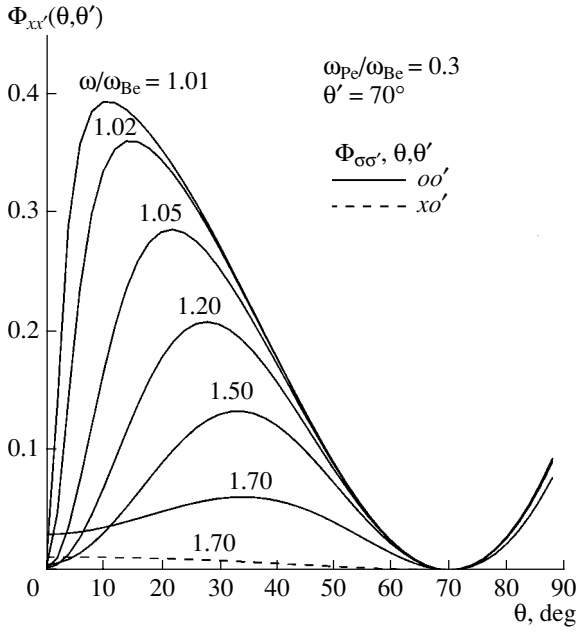

Fig. 5. Dependence of the probability of induced scattering of an ordinary wave into an ordinary wave $\Phi_{oo'}(\theta,\theta')$ on the angle θ between the wave vector of the scattered wave and the magnetic field for $\theta' = 70°$. The dashed curve shows the dependence $\Phi_{xo'}(\theta,\theta')$ for frequencies above the cutoff frequency for $\omega_{Pe}/\omega_{Be} = 1$.

$$\Phi_{\sigma o'}(\theta) = \left(\cos\theta - \cos\theta'\right)^2 \Psi_{o\sigma}(\theta,\theta')\big|_{\theta'=70°}. \quad (37)$$

We can see from (36) that the optical depth $\tau_{\sigma o'}$ grows with the ratio ω_{Pe}/ω_{Be}, reaching its maximum value at the outer boundary of the region in which predominantly ordinary waves are generated; i.e., when $\omega_{Pe}/\omega_{Be} \simeq 1$. Figure 5 shows the dependence of the function $\Phi_{xo'}(\theta,\theta' = 70°)$ on the scattering angle for $\omega_{Pe}/\omega_{Be} = 1$ and various values of ω/ω_{Be}. The dashed curve shows the dependence $\Phi_{xo'}(\theta,\theta' = 70°)$ for $\omega/\omega_{Be} = 1.7$; i.e., for a frequency exceeding the cutoff frequency for the extraordinary waves, at which these waves can escape the source. We can see that scattering into an ordinary wave is appreciably more efficient than scattering into an extraordinary wave, and this latter process can be neglected. The function $\Phi_{oo'}(\theta,\theta')$ has a relatively sharp maximum, which falls into the window of transparency for ordinary waves when $\omega/\omega_{Be} = 1.02-1.2$. It is easy to convince oneself of this using Fig. 2, which presents the gyroresonance absorption at the second harmonic of the gyrofrequency ($s = 2$) for the corona of AD Leo and the solar corona (recall that the width of the window of transparency for the corona of AD Leo is about 15°, while that for the solar corona is about 25°).

3.2.1. The Corona of AD Leo. Let us adopt, as in our previous estimates, the gyrofrequency in the radio source of AD Leo $\omega_{Be} \simeq 3\times10^{10}$ rad/s, which corresponds to a frequency of 4.85 GHz. In this case, the ECM mechanism generates ordinary waves at $\omega \simeq \omega_{Be}$. It follows from the form of the function $\Phi_{oo'}(\theta,\theta')$ presented in Fig. 5 that the maximum of this function is shifted toward the window of transparency, and increases as the generation frequency approaches the gyrofrequency. Formula (36) for the optical depth of the source to induced scattering yields

$$\tau_{oo'}(\theta) \simeq 3\times10^6 \Phi_{oo'}(\theta,\theta')\frac{N_h}{N_0}. \quad (38)$$

The numerical coefficient has been written for a temperature of the main plasma $T = 10^7$ K and a temperature for the energetic particles $T_h = 3\times10^8$ K. When $\omega \simeq \omega_{Be}$, the function takes on its maximum value for $\theta_m \simeq 15°$. Near θ_m, the angular dependence of $\tau_{oo'}(\theta)$ can be approximated by the function

$$\tau_{oo'}(\theta) \simeq 10^6 \cos^n(\theta-\theta_m)\frac{N_h}{N_0}, \quad (39)$$

where $n \simeq 10$. We can see that the optical depth is high, so that induced scattering efficiently moves the excited waves into the window of transparency, and the angular width of the condensate of scattered waves is

$$\Delta\theta \simeq \frac{10^{-3}}{n}\left(\frac{N_0}{N_h}\right)^{1/2} \text{ rad}, \quad (40)$$

which yields $\Delta\theta \simeq 6°$ in the limiting case $N_h/N_0 \simeq 10^{-6}$. Thus, the bulk of the excited waves fall into the window of transparency along the magnetic field due to induced scattering, and leave the source as ordinary waves without appreciable absorption.

3.2.2. The Solar Corona. Let us estimate the optical depth to induced scattering for the parameters characteristic of type I noise storms, assuming that ordinary waves are excited in the source by the ECM mechanism. We will assume $\omega_{Be} \simeq 6\times10^8$ rad/s (a frequency for the radio emission of about 100 MHz), $\omega_{Pe}/\omega_{Be} = 1$, $T = 10^6$ K, $T_h = 3\times10^8$ K, and $L_B = 3\times10^9$ cm. The optical depth,

$$\tau_{oo'}(\theta) \simeq 7\times10^4 \cos^n(\theta-\theta_m)\frac{N_h}{N_0}, \quad (41)$$

where $n \simeq 10$, has a sharp maximum near $\theta_m \simeq 15°$ with an angular width of

$$\Delta\theta \simeq \frac{3.7\times10^{-3}}{n}\left(\frac{N_0}{N_h}\right)^{1/2} \text{ rad}. \quad (42)$$

The scattering is efficient if the density of fast particles in the source is sufficiently high, $N_h/N_0 \gg 1.4\times10^{-5}$. The maximum width of the angular spectrum of the scattered waves is $\Delta\theta_{max} \simeq 5.6°$. Since the condensate of scattered waves falls into the window

of transparency, where there is little gyroresonance absorption, the radiation can freely leave the source.

4. CONCLUSION

Let us formulate the main conclusions of our analysis concerning the escape of electron-cyclotron maser radiation from hot stellar coronas. As examples, we have considered the coronas of the red dwarf AD Leo, where the expected plasma temperature could reach 10^7 K, and of the Sun, where the plasma temperature is 10^6 K.

If the magnetic field in the source is sufficiently strong ($\omega_{Pe}/\omega_{Be} < 0.25-0.4$), the ECM generates extraordinary waves near the electron gyrofrequency $\omega \simeq \omega_{Be}$ at an angle $\theta' \simeq 70°$ to the magnetic field. In this case, the excited radiation is scattered predominantly into extraordinary waves at a smaller angle θ. If the growth in the intensity of the scattered wave is exponential and the optical depth to induced scattering is fairly high (this will be the case when $N_h/N_0 \gg 6 \times 10^{-7}$ for the corona of AD Leo and $N_h/N_0 \gg 10^{-5}$ for the solar corona), this leads to the formation of a condensate near $\theta \simeq 0°$ with an angular width of $\Delta\theta \simeq 3.8°$ for AD Leo and $\Delta\theta \simeq 15°$ for the Sun. The width of the window of transparency near $\theta \simeq 0°$ is appreciably smaller, being 0.2° for AD Leo and 0.5° for the Sun. This means that only a small fraction of the radiation can escape from the source: 3×10^{-3} for the corona of AD Leo and 10^{-3} for the solar corona. The remaining radiation is absorbed as it propagates through the gyroresonance level $s = 2$.

When $0.25-0.4 \lesssim \omega_{Pe}/\omega_{Be} \lesssim 1$, the ECM mechanism excites ordinary waves at an angle of $\theta' \simeq 70°$ to the magnetic field. These waves are scattered predominantly into ordinary waves, with the probability of scattering growing as the angle between the magnetic field and the direction of propagation decreases, reaching its maximum at $\theta_m \simeq 15°$, which is within the window of transparency for ordinary waves (Fig. 2). The optical depth to scattering is high when $N_h/N_0 \gg 10^{-6}$ for the corona of AD Leo and $N_h/N_0 \gg 1.4 \times 10^{-5}$ for the solar corona. The angular width of the condensate of ordinary waves is $\Delta\theta \simeq 6°$, i.e., smaller than the window of transparency. This means that, when $\tau_{oo} \gg 1$, the bulk of the generated ECM radiation can leave the source as a result of induced scattering from the region of instability into a window of transparency for cyclotron absorption. Our analysis and comparisons indicate that, if sources of powerful ECM radiation are realized in the coronas of the Sun and dMe stars, they should generate primarily ordinary waves.

ACKNOWLEDGMENTS

This work was supported by the Russian Foundation for Basic Research (project nos. 05-02-162252 and 03-02-20009-BNTSa), the Program of Support for Leading Scientific Schools of Russia, the Basic Research Program of the Presidium of the Russian Academy of Sciences *Non-stationary Phenomena in Astronomy,* the program of the Physical Sciences Division of the Russian Academy of Sciences *Solar Wind: Generation and Interaction with the Earth and Other Planets,* and the Commission on International Collaboration of the Austrian Academy of Sciences.

REFERENCES

1. G. A. Dulk, Annu. Rev. Astron. Astrophys. **23**, 169 (1985).
2. D. B. Melrose, in *Cool Stars, Stellar Systems, and the Sun*, Ed. by T. Linsky and R. E. Stencel (Springer, Berlin, 1987), p. 83.
3. R. M. Hjellming, in *Galactic and Extragalactic Radio Astronomy*, Ed. by G. L. Verschuur and K. I. Kellerman (Springer, Berlin and New York, 1988), p. 381.
4. J. Kuijpers, Solar Phys. **121**, 163 (1989).
5. J. A. Bookbinder, in *Activity in Cool Star Envelopes*, Ed. by O. Havnes, B. R. Pettersen, and J. H. M. M. Schmitt (Kluwer, Dordrecht, 1988).
6. T. S. Bastian, Solar Phys. **130**, 265 (1990).
7. R. E. Gershberg, *Solar-type Activity of Main Sequence Stars* (Astroprint, Odessa, 2002), p. 688 [in Russian].
8. A. V. Stepanov, E. Furst, A. Kruger, *et al.*, Astron. Astrophys. **299**, 739 (1995).
9. A. V. Stepanov, B. Kliem, V. V. Zaitsev, *et al.*, Astron. Astrophys. **374**, 1072 (2001).
10. V. V. Zheleznyakov, *Radio Emission of the Sun and Planets* (Nauka, Moscow, 1964), p. 560 [in Russian].
11. V. V. Zheleznyakov and V. V. Zaitsev, Astron. Zh. **47**, 60 (1970) [Sov. Astron. **14**, 47 (1970)].
12. V. V. Zheleznyakov and V. V. Zaĭtsev, Astron. Zh. **47**, 308 (1970) [Sov. Astron. **14**, 250 (1970)].
13. A. V. Stepanov, Astron. Zh. **50**, 1243 (1973) [Sov. Astron. **17**, 781 (1973)].
14. J. Kuijpers, Solar Phys. **36**, 157 (1974).
15. V. V. Zaitsev and A. V. Stepanov, Astron. Astrophys. **45**, 135 (1975).
16. V. V. Zaitsev and A. V. Stepanov, Solar Phys. **88**, 297 (1983).
17. R. G. Hewitt and D. B. Melrose, Solar Phys. **96**, 157 (1985).
18. R. M. Winglee and G. A. Dulk, Astrophys. J. **307**, 808 (1986).
19. A. V. Stepanov, B. Kliem, A. Kruger, *et al.*, Astrophys. J. **524**, 961 (1999).
20. A. F. Kukes and R. N. Sudan, Solar Phys. **17**, 194 (1971).

21. A. V. Stepanov, Pis'ma Astron. Zh. **4**, 193 (1978) [Sov. Astron. Lett. **4**, 103 (1978)].
22. G. D. Holman, D. Eichler, and M. R. Kundu, *Radiophysics of the Sun*, Ed. by M. R. Kundu and T. Gergely (Reidel, Dordrecht, 1980), p. 457.
23. D. B. Melrose and G. A. Dulk, Astrophys. J. **259**, 844 (1982).
24. P. Louran, D. Le Queau, and A. Roux, Astron. Astrophys. **165**, 211 (1986).
25. P. Louran, D. Le Queau, and A. Roux, Solar Phys. **111**, 201 (1987).
26. M. E. McKean, R. M. Winglee, and G. A. Dulk, Solar Phys. **122**, 53 (1989).
27. M. J. Aschwanden, Astron. Astrophys. **237**, 512 (1990).
28. R. R. Sharma and L. Vlahos, Astrophys. J. **280**, 405 (1984).
29. D. B. Melrose, G. A. Dulk, and R. G. Hewitt, J. Geophys. Res. **89**, 897 (1984).
30. A. G. Litvak and V. Yu. Trakhtengerts, Zh. Éksp. Teor. Fiz. **60**, 1702 (1971) [Sov. Phys. JETP **33**, 921 (1971)].
31. A. G. Litvak and V. Yu. Trakhtengerts, Zh. Éksp. Teor. Fiz. **62**, 228 (1972) [Sov. Phys. JETP **62**, 228 (1972)].
32. D. B. Melrose and W. Sy, Astrophys. Space Sci. **17**, 345 (1972).
33. V. V. Zheleznyakov, *Electromagnetic Waves in Astrophysical Plasma* (Nauka, Moscow, 1977), p. 432 [in Russian].
34. S. H. Saar and J. L. Linsky, Astrophys. J. **299**, L47 (1985).

Translated by D. Gabuzda

Astronomy Reports, Vol. 49, No. 4, 2005, pp. 337–342. Translated from Astronomicheskiĭ Zhurnal, Vol. 82, No. 4, 2005, pp. 378–384.

A Dynamo Wave near the Solar Equator

V. M. Galitski[1], D. D. Sokoloff[2], and K. M. Kuzanyan[3]

[1]*Kavli Institute for Theoretical Physics, University of California, Santa Barbara, CA 93106-4030, USA*

[2]*Department of Physics, Moscow State University, Moscow, 119992 Russia*

[3]*Institute of Terrestrial Magnetism, Ionosphere, and Radiowave Propagation, Russian Academy of Sciences, Troitsk, Moscow oblast, 142190 Russia*

Received April 25, 2004; in final form, September 20, 2004

Abstract—The structure of a dynamo wave near the solar equator is considered in the Parker approximation. The results show that the principal dynamo wave, which travels in the northern hemisphere from middle latitudes toward the equator, penetrates slightly into the southern hemisphere. The wave that propagates in the southern hemisphere exhibits similar behavior. The angular distance the wave is able to penetrate into the neighboring hemisphere can reach about ten degrees of latitude. Possible observational manifestations of this effect are discussed. The growth rate of the dipolar magnetic-field configuration exceeds that of the quadrupolar configuration, and the difference between these growth rates is computed. A possible relation of this quantity to the time characteristics of the Maunder minimum is discussed.

1. INTRODUCTION

The magnetic-activity cycle involves two waves of activity, which propagate in opposite directions in the northern and southern hemispheres. Naturally, these waves are not strictly symmetrical. It has become clear relatively recently that the asymmetry between the hemispheres was especially pronounced at the end of the Maunder minimum, when the activity wave propagated over only one hemisphere [1, 2].

Solar activity is usually associated with the action of the solar dynamo and the propagation of dynamo waves, which are manifest as activity waves. To some extent, the asymmetry of solar activity can be reproduced in numerical simulations based on the dynamo equations (see, e.g., [3]). However, the origin of the asymmetry remains incompletely understood. To clarify this point, we analyze here symmetry properties about the solar equator for a simple Parker model [4] for the solar dynamo in a linear (kinematic) approximation. We use analytical (asymptotic), rather than numerical, techniques to relate the symmetry properties and the model parameters. It is obvious that Parker's kinematic dynamo is only a crude approximation to reality that will enable us to find only the configuration of the dipole and quadrupole magnetic fields and a relationship between the conditions for their generation. We will then use this information to give some indication of the possible asymmetries of more complex models for the solar dynamo. Deeper conclusions will require studies with more realistic models. Nevertheless, we believe that this investigation need not start from a complex realistic model, and instead the physical processes should first be explained in terms of a simple Parker model.

2. GOVERNING EQUATIONS

We consider the mean-field equations in the $\alpha\Omega$ approximation and assume that the generation of the magnetic field is localized in a thin spherical layer, with the rotation curve dominated by the radial gradient $G = \partial\Omega/r\partial r$, which varies slowly with the latitude θ (measured from the equator). We consider an axisymmetric magnetic field, which can be represented in terms of a toroidal component B and a poloidal component that is specified by a variable A that is proportional to the azimuthal component of the vector potential. We are interested in eigenmodes whose time dependence has the form $\exp(\gamma t)$. Averaging the mean-field equations over the cross section of the layer leads to the equations

$$\gamma A = \alpha(\theta)B + \frac{d}{d\theta}\left[\frac{1}{\cos\theta}\frac{d}{d\theta}(A\cos\theta)\right], \quad (1)$$

$$\gamma B = -DG(\theta)\frac{d}{d\theta}(A\cos\theta) + \frac{d}{d\theta}\left[\frac{1}{\cos\theta}\frac{d}{d\theta}(B\cos\theta)\right]. \quad (2)$$

Here, D is the dimensionless dynamo number, which we assume to be negative and large in absolute magnitude. The functions $\alpha(\theta)$ and $G(\theta)$ are measured in

1063-7729/05/4904-0337$26.00

units of their maximum values and have the following symmetry properties: $\alpha(\theta) = -\alpha(-\theta)$, $G(\theta) = G(-\theta)$. The exact form of these functions is not very important for our purposes, and we assume for our estimates that $\alpha(\theta) = \sin\theta$ and $G = 1$; however, if necessary, we can use more realistic approximations (see, e.g., [5]) for the rotation curve, which is known from helioseismological data [6].

It is useful to rewrite (1) and (2) in the symbolic form $\hat{\mathcal{H}}\mathbf{h} = \gamma\mathbf{h}$, where we have introduced the two-component complex function $\mathbf{h}(\theta) = \begin{pmatrix} A(\theta) \\ B(\theta) \end{pmatrix}$ and the matrix differential operator

$$\hat{\mathcal{H}} = \begin{pmatrix} \Delta & \alpha(\theta) \\ -DG(\theta)\dfrac{d}{d\theta}\cos\theta & \Delta \end{pmatrix}, \qquad (3)$$

where $\Delta = \dfrac{d}{d\theta}\dfrac{1}{\cos\theta}\dfrac{d}{d\theta}\cos\theta$ is the azimuthal part of the Laplacian. The operator (3) is not Hermitian and, therefore, can, in general, have complex eigenvalues. The corresponding adjoint operator has the form $\hat{\mathcal{H}}^{\dagger} = \begin{pmatrix} \Delta & DG(\theta)\dfrac{d}{d\theta}\cos\theta \\ \alpha(\theta) & \Delta \end{pmatrix}$. These operators are defined for $-\pi/2 \le \theta \le \pi/2$.

The structure of the eigenfunctions $\mathbf{n}$ of the operator $\hat{\mathcal{H}}$ far from the poles and equator can be found using a WKB technique, which also provides an estimate for γ [7, 8]. To this end, the solution for, e.g., the northern hemisphere should be sought in the form of the product of a rapidly oscillating exponential function and a slowly varying amplitude $\mathbf{n}_0$:

$$\mathbf{n}(\theta) = \mathbf{n}_0(\theta)\exp\left[\frac{iS(\theta)}{\varepsilon}\right], \qquad (4)$$

where $\varepsilon = |D|^{-1/3}$. The eigenvalues should be sought in the form $\gamma = \varepsilon^{-2}\Gamma_0 + \varepsilon^{-1}\Gamma_{1,n} + \ldots$, where the index n counts the eigenvalues (complex growth rates).

The application of the WKB technique yields

$$\mathbf{n}_0(\theta) = \frac{1}{\cos\theta}\begin{pmatrix} \Gamma_0 + k(\theta)^2 \\ i\varepsilon^{-2}k(\theta)\cos\theta \end{pmatrix}\sigma(\theta), \qquad (5)$$

where $k(\theta) = dS(\theta)/d\theta$ can be found from the Hamilton–Jacobi equation:

$$\left[\Gamma_0 + k^2(\theta)\right]^2 - i\tilde{\alpha}(\theta)k(\theta) = 0, \qquad (6)$$

and $\tilde{\alpha} = \alpha(\theta)G(\theta)\cos\theta$. This algebraic equation has four branches, and a smooth solution cannot be constructed based on one branch. Two of the four branches are present in the solution [7]. The condition of smooth matching can be used to obtain γ:

$$\Gamma_0 = \frac{3}{2^{8/3}}\tilde{\alpha}_{max}^{2/3}e^{i\frac{\pi}{3}}, \qquad (7)$$

$$\Gamma_{1,n} = 3ik'(\theta')\left[n + 1/2\right], \quad n = 0, 1, 2, ...,$$

where the matching point θ' is the point of the maximum of the function $\tilde{\alpha}(\theta)$. The leading mode corresponds to $n = 0$. The function $\sigma(\theta)$ in (5) has the form

$$\sigma_n(\theta) = \exp\left\{\int \frac{\Gamma_{1,n} - ik'\left(1 + \dfrac{2k^2}{\Gamma_0 + k^2}\right)}{2ik + \dfrac{\hat{\alpha}}{2(\Gamma_0 + k^2)}}d\theta\right\}. \qquad (8)$$

3. EQUATORIAL REGION

The WKB approximation fails near the equator, where $\theta < \varepsilon$, since $d\mathbf{n}_0/d\theta \sim \theta^{-1}\mathbf{n}_0$, and the amplitude $\mathbf{n}_0$ is no longer a slowly varying function, for which $d\mathbf{n}_0/d\theta \ll \varepsilon^{-1}\mathbf{n}_0$. It can readily be shown using (4)–(8) that, near the equator, $\sigma(\theta) \approx \theta^{-1/4}$ and $k'(\theta) \sim \theta^{-1/2}$. Therefore, the asymptotic structure of the eigenmodes in the equatorial region must be additionally analyzed.

Near the point $\theta = 0$, (1) and (2) have the form

$$\gamma A(\theta) = \alpha'(0)\theta B(\theta) + A''(\theta), \qquad (9)$$

$$\gamma B(\theta) = -DA'(\theta) + B''(\theta). \qquad (10)$$

Here, γ plays the role of an independent external parameter. In the region $\theta < \varepsilon$, in view of the perturbing corrections δ, the solution can be represented as a superposition of two waves:

$$\begin{pmatrix} A(\theta) \\ B(\theta) \end{pmatrix} = \begin{pmatrix} A_1 + \delta A_1(\theta) \\ B_1 + \delta B_1(\theta) \end{pmatrix} e^{-\sqrt{\gamma}\theta} + \begin{pmatrix} A_2 + \delta A_2(\theta) \\ B_2 + \delta B_2(\theta) \end{pmatrix} e^{\sqrt{\gamma}\theta}, \qquad (11)$$

where the constants $A_{1,2}$ and $B_{1,2}$ can be determined from the condition for matching the solution (11) to the solution for the middle latitudes. In contrast to the WKB solution, (11) is regular at the equator.

Let $\mathbf{n}(\theta)$ be the solution obtained for the northern hemisphere and $\mathbf{s}(\theta)$ is the corresponding solution for the southern hemisphere. Note that the first term in (11) describes a wave propagating toward the equator, and the second term an exponentially damped wave propagating toward the pole. The first term must be matched to the WKB solution

for the northern hemisphere. To this end, we must assume that the wave in the solution $\mathbf{s}(\theta)$ originating in the southern hemisphere penetrates into the northern hemisphere. The exponential factors in (11) and in the WKB decomposition should coincide near the equator. By equating these terms, we express the coefficients $A_{1,2}$ and $B_{1,2}$ in terms of the coefficients of the WKB expansion.

Note that one of the four branches of $k(\theta)$ obtained from (6)—the third—remains unused in this procedure. This third branch enables us to construct a solution near the pole, where the WKB approximation is likewise not applicable [8]. It turns out that the third branch describes a wave reflected from the pole, since it is monotonically damped as θ decreases to $-\pi/2$. Note also that the fourth branch describes a wave that penetrates from the other hemisphere through the equator, which is damped as θ increases to $\pi/2$.

Using the WKB expansion in the limiting case $\theta \ll 1$, we obtain

$$\mathbf{n} = \begin{pmatrix} ae^{(i\pi/12)}(\theta_1)^{1/4} \\ \varepsilon^{-2}be^{(i\pi/6)}(\theta_1)^{-1/4} \end{pmatrix} \exp\left(-\sqrt{\gamma}\theta\right), \quad (12)$$

and the adjoint solution for the southern hemisphere is

$$\mathbf{s}^a(\theta) = \begin{pmatrix} \varepsilon^{-2}be^{(i\pi/12)}(\theta_1)^{-1/4} \\ ae^{(-i\pi/3)}(\theta_1)^{1/4} \end{pmatrix} \exp\left(-\sqrt{\gamma^*}\theta\right). \quad (13)$$

The condition of matching the two solutions at $\theta_1 \sim \varepsilon$ yields $a = 2^{4/3}3^{1/4}\sqrt{\tilde{\alpha}'(0)}\tilde{\alpha}_{max}^{2/3}$, $b = 3^{1/2}2^{(-4/3)}\tilde{\alpha}_{max}^{1/3}$.

We now estimate the rate of spatial damping of the wave originating in one hemisphere and penetrating into the neighboring one. The characteristic damping distance in latitude Θ^* is determined by the quantity $(\mathrm{Re}\gamma)^{-1/2}$. For $D = -10^3$ ($\varepsilon = 0.1$), we obtain $\Theta^* = 0.28$ (or 16°). For $D = -10^4$, we find $\Theta^* = 7°$. These estimates are consistent with data for active regions [1] whose polarities do not obey the Hale law. Such regions emerge at the end of the solar cycle, mainly at low latitudes, near the solar equator. In our view, they correspond to dynamo waves that penetrate into the neighboring hemispheres.

4. SYMMETRY PROPERTIES

Below, we will need the spatial-reflection operator $\hat{P}$, defined by the relationship $\hat{P}f(\theta) = f(-\theta)$. It is obvious that its eigenvalues (the parity) are $p = \pm 1$. By applying this operator to the most general equations of mean-field electrodynamics, it can easily be verified that the operator $\hat{P}$ commutes with the operator appearing in this equation. In doing this, we must use the symmetry properties of the helicity $\hat{P}\alpha(\mathbf{r}) = -\alpha(\mathbf{r})$ and velocity $\hat{P}\mathbf{v}(\mathbf{r}) = \mathbf{v}(\mathbf{r})$. Therefore, the modes of the magnetic field as eigenvectors of the operator $\hat{P}$ can be classified by their parity p. The value $p = +1$ corresponds to quadrupolar and $p = -1$ to dipolar solutions. In general, the eigenvalues of γ corresponding to different parities do not coincide.

Naturally, Eqs. (1) and (2) inherit these symmetry properties of the mean-field equations. Their characteristic feature is that they are written in terms of the toroidal components of the magnetic field and the vector potential, which have opposite parities. To express this, we introduce the unitary matrix $\hat{U} = \hat{U}^\dagger = \mathrm{diag}(1, -1)$. The dipolar solutions satisfy the condition $\hat{P}\hat{U}\mathbf{d} = \mathbf{d}$, and the quadrupolar solutions the condition $\hat{P}\hat{U}\mathbf{q} = -\mathbf{q}$. The corresponding spectral problems have the form $\hat{\mathcal{H}}\mathbf{d} = \gamma_d\mathbf{d}$ and $\hat{H}\mathbf{q} = \gamma_q\mathbf{q}$. We have for the eigenvectors of the adjoint operator $\hat{\mathcal{H}}^\dagger\mathbf{d}^a = \gamma_d^*\mathbf{d}^a$ and $\hat{\mathcal{H}}^\dagger\mathbf{q}^a = \gamma_q^*\mathbf{q}^a$. Since we are dealing with non-Hermitian operators, the eigenvectors for mutually adjoint operators do not coincide; however, since the magnetic field is real, the eigenvalues form complex conjugate pairs. Below, we will primarily be interested in the structure of the eigenfunctions, but will also determine the splitting between the dipolar and quadrupolar eigenvalues.

Note that our spectral problem is similar to the well-known quantum-mechanical problem of level splitting in a potential consisting of two symmetrical wells. To solve this problem, we will use the well-known technique (which traces back to E.M. Lifshitz) [9] of modifying it in view of the non-Hermitian properties of our operator. We recall that the Lifshitz treatment refers to a one-dimensional potential consisting of two symmetrical wells separated by a high barrier. If we neglect the tunneling of a particle through the barrier, the energy levels are degenerate and can be calculated for either well (e.g., the right-hand well) using the WKB technique. Away from the well, the corresponding eigenfunctions decay exponentially. Allowance for the finite probability of tunneling removes the degeneracy, and the energy levels split into pairs whose components correspond to the symmetric and antisymmetric solutions. Of primary interest is the difference of the relevant energies, which corresponds to the rate of tunneling through the barrier. This rate is normally small and very difficult to evaluate, especially for high barriers. However, it can be determined using the WKB technique.

In our case, we are dealing with regions of generation in the northern and southern hemispheres separated by the equatorial region, in which there is

no generation. This region is similar to a barrier. If we neglect the penetration of dynamo waves from one hemisphere to the other, we can obtain the classical solutions (4)–(8). Using the solutions $\mathbf{n}(\theta)$ for the northern and $\mathbf{s}(\theta)$ for the southern hemisphere and applying the method of Lifshitz, we can construct the dipolar and quadrupolar modes according to the rule

$$\mathbf{d}(\theta) = \frac{1}{\sqrt{2}}\left[\mathbf{n}(\theta) + \mathbf{s}(\theta)\right], \qquad (14)$$
$$\mathbf{q}(\theta) = \frac{1}{\sqrt{2}}\left[\mathbf{n}(\theta) - \mathbf{s}(\theta)\right],$$

where the factor $1/\sqrt{2}$ is introduced for normalization purposes. We note that the solution for the southern hemisphere can be written $\mathbf{s}(\theta) = \hat{P}\hat{U}\mathbf{n}(\theta)$.

We will need the dot product of the vector functions $\mathbf{f}$ and $\mathbf{g}$, which we define as

$$(\mathbf{f},\mathbf{g}) = \int_0^{\pi/2} [f_1(\theta)g_1^*(\theta) + f_2(\theta)g_2^*(\theta)]\cos\theta d\theta, \quad (15)$$

where $\mathbf{f} = \begin{pmatrix} f_1 \\ f_2 \end{pmatrix}$ and $\mathbf{g} = \begin{pmatrix} g_1 \\ g_2 \end{pmatrix}$. The scalar multiplication of our equations by $\mathbf{d}^a$ and $\mathbf{n}$ followed by the combination of the results yields

$$\gamma_d^* - \gamma_0 = \frac{\left(\left(\hat{\mathcal{H}}^\dagger \mathbf{d}^a\right)^*, \mathbf{n}\right) - \left(\mathbf{d}^{a*}, \hat{\mathcal{H}}\mathbf{n}\right)}{(\mathbf{d}^{a*}, \mathbf{n})}, \qquad (16)$$
$$\gamma_q^* - \gamma_0 = \frac{\left(\left(\hat{\mathcal{H}}^\dagger \mathbf{q}^a\right)^*, \mathbf{n}\right) - \left(\mathbf{q}^{a*}, \hat{\mathcal{H}}\mathbf{n}\right)}{(\mathbf{q}^{a*}, \mathbf{n})}.$$

We now take into account the fact that the dynamo wave penetrating from one hemisphere to the other is exponentially weak. This implies that $|(\mathbf{s}^{a*}, \mathbf{n})| \ll |(\mathbf{n}^{a*}, \mathbf{n})|$. Therefore, $(\mathbf{d}^{a*}, \mathbf{n}) \sim (\mathbf{q}^{a*}, \mathbf{n}) \sim (\mathbf{n}^{a*}, \mathbf{n})$.

Neglecting the small difference between the denominators, we obtain

$$\gamma_d^* - \gamma_q^* = 2\frac{\left(\left(\hat{\mathcal{H}}^\dagger \mathbf{s}^a\right)^*, \mathbf{n}\right) - \left(\mathbf{s}^a, \hat{\mathcal{H}}\mathbf{n}\right)}{(\mathbf{n}^{a*}, \mathbf{n})}. \qquad (17)$$

The explicit form of the operators $\hat{\mathcal{H}}$ and $\hat{\mathcal{H}}^\dagger$ gives

$$\frac{1}{2}(\mathbf{n}^{a*}, \mathbf{n})\Delta\gamma^* = \int_0^{\pi/2} d\theta \cos\theta \Big[\Delta s_1^a n_1 + D\frac{d}{d\theta} \qquad (18)$$
$$\times (\cos\theta s_2^a)\, n_1 + \Delta s_2^a n_2$$
$$- s_1^a(\Delta n_1) + D s_2^a \frac{d}{d\theta}(\cos\theta n_1) - s_1^a(\Delta n_2)\Big],$$

where the subscripts 1 and 2 correspond to the upper and lower components of the two-dimensional vectors and s^a is the solution to the adjoint equation for the southern hemisphere. Integration by parts yields

$$\frac{1}{2}(\mathbf{n}^{a*}, \mathbf{n})\Delta\gamma^* = n_1\frac{ds_1^a}{d\theta} + n_2\frac{ds_2^a}{d\theta} \qquad (19)$$
$$- s_1^a\frac{dn_1}{d\theta} - s_2^a\frac{dn_2}{d\theta} + Dn_1 s_2^a\Big|_{\theta=0}.$$

5. LEVEL SPLITTING

To make further estimates, we will need to know the structure of an eigenmode for all latitudes (not only in one hemisphere). This can be expressed in terms of the eigenfunction $\mathbf{n}(\theta)$ by making the substitution $n_{1,2} \to n_{2,1}$, $\Gamma_0 \to \Gamma_0^*$, $\Gamma_1 \to \Gamma_1^*$, where n_1 and n_2 are the upper and lower components of the eigenvector, respectively. The solution to the Hamilton–Jacobi equation (6) then transforms according to the rule $k(\theta) \to -k^*(\theta)$. Finally, we obtain

$$\mathbf{n}^a(\theta) = \begin{pmatrix} -i\varepsilon^{-2}k^*(\theta)\cos\theta \\ \Gamma_0^* + k^*(\theta)^2 \end{pmatrix} \frac{\sigma^*(\theta)}{\cos\theta}\exp\left[-\frac{iS^*(\theta)}{\varepsilon}\right]. \qquad (20)$$

We then use (5) and (20) to obtain

$$(\mathbf{n}^a, \mathbf{n}) = i\varepsilon^{-2}\int_0^{\pi/2} d\theta[-(\Gamma_0 + k^2(\theta))k^*(\theta) \qquad (21)$$
$$+ k(\theta)(\Gamma_0 + k^2(\theta))^*]|\sigma(\theta)|^2 e^{-\frac{2}{\varepsilon}\int_0^\theta \mathrm{Im}\, k(\theta')d\theta'}.$$

Calculation of the outer integral using the Laplace method yields

$$(\mathbf{n}^{a*}, \mathbf{n}) = \frac{4\mathrm{Im}\,\Gamma_0}{\varepsilon^2}\sqrt{\frac{\pi\varepsilon}{\mathrm{Im}\, k'(\theta_*)}}\,|\sigma(\theta_*)|^2 \qquad (22)$$
$$\times k(\theta_*)\exp\left\{-\frac{2}{\varepsilon}\int_0^{\theta_*}\mathrm{Im}\, k(\theta)d\theta\right\},$$

where θ_* is the point at which the effect of $S(\theta)$ is maximum, i.e., $\mathrm{Im}\, k(\theta_*) = 0$. This point is specified by the relationship [7] $\tilde{\alpha}(\theta_*)/\tilde{\alpha}_{max} = 9\sqrt{3} \times (16\sqrt{2}\sqrt{\sqrt{3}-1})^{-1} \approx 0.8052$. Note that the quantity (22) is real, positive, and exponentially large, so that the level splitting is exponentially small. Similar estimates for the terms appearing in (19) yield

$$\left[n_1\frac{ds_1^a}{d\theta} - s_2^a\frac{dn_2}{d\theta}\right]\Big|_{\theta=0} = \frac{2ab}{\varepsilon^3}\mathrm{Re}\,\left[e^{(-i\pi/6)}\sqrt{\Gamma_0}\right], \qquad (23)$$

$$\left[n_2\frac{ds_2^a}{d\theta}-s_1^a\frac{dn_1}{d\theta}\right]\Bigg|_{\theta=0}=\frac{2ab}{\varepsilon^3}\mathrm{Re}\,\left[e^{(-i\pi/6)}\sqrt{\Gamma_0}\right], \tag{24}$$

$$Dn_1s_2^a\Big|_{\theta=0}=-\frac{a^2\sqrt{\theta_1}}{\varepsilon^3}e^{(-i\pi/3)}.$$

Note that the first two terms, which preserve the Hermitian properties of the operator, contribute to the real part of the splitting (i.e., to the difference in the growth rates) and do not depend on the position of the matching point θ_1. The third, non-Hermitian, term contributes to the difference in the frequencies and depends on the position of the matching point. Since $\theta_1\sim\varepsilon$, this contribution is much smaller than the former one. We obtain from (23) and (24)

$$(\mathbf{n}^a,\mathbf{n})\,\Delta\gamma=\frac{1}{\varepsilon^3}\frac{3^{9/4}}{2^{1/3}}\tilde\alpha_{max}^{4/3}\sqrt{\tilde\alpha'(0)} \tag{25}$$

$$-i\frac{\sqrt{\varepsilon}}{\varepsilon^3}2^{19/6}3^{1/2}\sqrt{\frac{\theta_1}{\varepsilon}}\tilde\alpha_{max}^{4/3}\tilde\alpha'(0).$$

The matching point θ_1 is determined as the point at which the phase shifts of both asymptotic expansions coincide [8].

We emphasize that we were not able to use the WKB asymptotics alone to obtain the above estimates, since this fails near the point $\theta=0$, which is a turning point in our problem. Note that this difficulty is not typical of quantum mechanics. The technique we have used is aimed at correctly evaluating the exponents that are involved in the splitting, and does not claim to be able to reproduce the coefficients of the exponential functions. Various approaches can be used to calculate these coefficients, which give slightly different results [10]. In view of this fact, we can rewrite our result in the form

$$\frac{\mathrm{Re}\,\Delta\gamma}{|\gamma_0|}\approx\sqrt{\varepsilon}\exp\left\{-\frac{2}{\varepsilon}\int\limits_0^{\theta_*}|\mathrm{Im}\,k(\theta)|\,d\theta\right\}, \tag{26}$$

$$\frac{\mathrm{Im}\,\Delta\gamma}{|\gamma_0|}\approx-\varepsilon\exp\left\{-\frac{2}{\varepsilon}\int\limits_0^{\theta_*}|\mathrm{Im}\,k(\theta)|\,d\theta\right\}.$$

6. DISCUSSION

Our analysis of the asymptotic behavior of dynamo waves in the equatorial region has enabled us to identify two phenomena.

First, as the dynamo wave that originates in the middle latitudes of the northern hemisphere reaches the equator, it does not disappear, but instead penetrates into the southern hemisphere, where it travels toward the pole and is then rapidly damped. Similar behavior is exhibited by the dynamo wave in the southern hemisphere. The angular distance these waves penetrate into the opposite hemisphere can attain roughly ten degrees. Evidence for effects of this sort seem be present in existing observations of solar activity. Of particular interest in this context are observations of solar activity conducted at the Paris Observatory during the final stage of the Maunder minimum [2, 13]. The solar-activity cycle was then manifest via a single dynamo wave propagating over the southern hemisphere, while the dynamo wave in the northern hemisphere was suppressed for some reason. The butterfly diagrams that can be constructed from archival data show that the activity wave slightly advances into the northern from the southern hemisphere. If this phenomenon is related to the effect considered above, the polarity of the spots in the northern hemisphere should be the same as in the southern hemisphere. In other words, the spots in the northern hemisphere should violate the Hale polarity law. Unfortunately, observations of the spot polarities were not possible in the 18th century, so that we must postpone observational confirmation of this conclusion to the next Maunder-like solar-activity minimum.

In modern observations, the weak wave penetrating from the southern hemisphere is masked by the principal wave in the northern hemisphere. However, activity tracers that propagate from the equator to a pole are known even from these observations; one example is far-UV lines (see, e.g. [12]). Some active regions violate the Hale polarity law [1]. It cannot be ruled out that these phenomena are associated with the penetration of dynamo waves from one hemisphere into the other. Directed observations of disruptions in the symmetry of the magnetic activity of the Sun about the equator, especially observations taking into account spot polarities, should help clarify this issue.

Another of our results is the comparison between the growth rates of the dipolar and quadrupolar magnetic configurations. We confirm that the dipolar magnetic configuration grows more rapidly and is excited more easily than the dipolar configuration. These facts are consistent with the assertion that the solar magnetic field is dipolar to the first approximation.

At the same time, the complex growth rates of the dipolar and quadrupolar configurations are similar. This suggests that, once it has arisen in some way, a nondipolar configuration can exist for a long time. It is such a situation that occurred at the end of the Maunder minimum. Our results furnish insights into the reasons for the long existence of mixed-parity configurations, although they do not disclose their origins.

At the same time, we cannot directly associate the difference between the growth rates of the dipolar and quadrupolar configurations with the time taken by the solar dynamo to leave the Maunder minimum. Indeed, for $\alpha(\theta) = \sin\theta$ and $D = -10^3$, we obtain $\mathrm{Re}\,\Delta\gamma/|\gamma_0| \sim 0.03$. In accordance with the actual duration of the solar cycle, we assume $(2\pi/\mathrm{Im}\,\gamma_0) \approx$ 22 yr, in which case $\mathrm{Im}\,\gamma_0 = |\gamma_0|\sqrt{3}/2$. Therefore, the regeneration time for the dipolar field can be estimated to be $\tau = 1/\mathrm{Re}\,\Delta\gamma \sim 100$ yr. This is appreciably longer than the duration of the phase of asymmetric solar activity at the end of the Maunder minimum, which lasted about ten years [2].

It is tempting to relate the difference between the imaginary parts of the dipolar and quadrupolar modes $\tau^* = 2\pi/\mathrm{Im}\,\Delta\gamma \sim 2 \times 10^3$ yr to the time separating great minima. The resulting value again turns out to be somewhat overestimated. We are inclined to attribute this quantitative disagreement between our asymptotic results and the observations to the fact that the Parker dynamo mechanism underestimates the link between the magnetic fields of the northern and southern hemispheres of the Sun. In this model, the magnetic field can find its way from one hemisphere to the other only by being transported across the equator in the convection zone. The nature of this transport is ultimately related to turbulent diffusion, so that the penetration weakens dramatically as the eddy diffusivity decreases, other parameters of the problem being fixed. In the real Sun, another penetration mechanism is possible. A poloidal magnetic-field line issues from the convection zone in the northern hemisphere, goes to the southern hemisphere through the weakly conducting circumsolar plasma, and again enters the convection zone. This link cannot be described in the Parker approximation, and it could be more efficient than the effects taken into account in this approximation.

A comparison of our results with the fact that quadrupolar dynamo modes are excited in thin galactic disks leads to the conclusion that, at least in a one-dimensional approximation, the preferred excitation of the mode of one or the other configuration depends on the direction of the angular-velocity gradient. If the angular velocity varies mainly across the layer in which the generation occurs (as in the Parker dynamo), the excitation of the dipolar mode is preferred. If the angular velocity varies along the layer (as is usually the case in galactic disks), the quadrupolar mode is excited. In some galaxies (NGC 5775), the angular velocity seems to vary not only along but also across the disk, and a dipolar dynamo wave is observed (see [13] for details).

ACKNOWLEDGMENTS

This work was supported by the Russian Foundation for Basic Research [project nos. 04-02-16068 (DDS) and 03-02-16384 and 02-02-39027 (KMK)].

REFERENCES

1. K. L. Harvey, *The Cyclic Behavior of Solar Activity*, Ed. by K. L. Harvey; ASP Conf. Ser. **27**, 335 (1992).
2. J. C. Ribes and E. Nesme-Ribes, Astron. Astrophys. **276**, 549 (1993).
3. A. Brandenburg, F. Krause, R. Meinel, *et al.*, Astron. Astrophys. **213**, 411 (1989).
4. E. N. Parker, Astrophys. J. **122**, 293 (1955).
5. G. M. Belvedere, K. M. Kuzanyan, and D. D. Sokoloff, Mon. Not. R. Astron. Soc. **315**, 778 (2000).
6. J. Schou, H. M. Antia, S. Basu, *et al.*, Astrophys. J. **505**, 390 (1998).
7. K. M. Kuzanyan and D. D. Sokoloff, Geophys. Astrophys. Fluid Dyn. **81**, 113 (1995).
8. V. M. Galitski and D. D. Sokoloff, Geophys. Astrophys. Fluid Dyn. **91**, 147 (1999).
9. L. D. Landau and E. M. Lifshits, *Quantum Mechanics* (Nauka, Moscow, 1974) [in Russian].
10. F. Cooper, A. Khare, and U. Sukhatme, Phys. Rep. **251**, 267 (1995).
11. D. D. Sokoloff and E. Nesme-Ribes, Astron. Astrophys. **288**, 293 (1994).
12. E. E. Benevolenskaya, A. A. Kosovichev, and P. H. Schereer, Astrophys. J. **554**, L107 (2001).
13. D. D. Sokoloff, Astron. Zh. **79**, 968 (2002) [Astron. Rep. **46**, 871 (2002)].

Translated by A. Getling